Università degli Studi Roma Tre

Dipartimento di Fisica "E. Amaldi"

Dottorato in Fisica XVII ciclo

MEASUREMENT OF THE BRANCHING RATIO OF THE DECAY $\eta \to \pi^0\gamma\gamma$ AND UPPER LIMIT ON THE DECAY $\eta \to 3\gamma$ WITH THE KLOE EXPERIMENT.

Biagio Di Micco

Supervisor
prof. Filippo Ceradini

Coordinator
prof. Orlando Ragnisco

Rome, December 2004

Introduction

This work has been done in the framework of the KLOE experiment at Frascati. KLOE is a general purpose detector that works on one of the two interaction points of the DAΦNE collider running at the "Laboratorio nazionale di Frascati". DAΦNE is an electron-positron collider that works at energy $\sqrt{s} = 1019MeV$, corresponding to the ϕ resonance mass. The ϕ is a spin 1 meson, odd under parity and C conjugation. Its main decay modes are K^+K^- (49%), $K^0_LK^0_S$ (34%), $\rho\pi$, (16%), $\eta\gamma$ (1.3 %). In 2001 and 2002 data taking, DAΦNE has produced about 1.5×10^9 ϕ mesons, and 18×10^6 η mesons. Such a large sample of η mesons is useful to understand the η decay physics, both in rare branching ratio measurement and upper limit determination on C and CP violating decays. From the historical point of view η physics has been studied mainly at hadron machines where, through nuclear reaction, a large amount of η mesons can be produced in short time. Nowadays KLOE, with its 18 million of η mesons, has the same order of magnitude of hadron machine data sample of η mesons in a more clear environment, guaranteed by a lepton machine.

In this work I have studied the η decay $\eta \to \pi^0\gamma\gamma$ and the forbidden decays $\eta \to \gamma\gamma\gamma$. The study of $\eta \to \pi^0\gamma\gamma$ decay is the main goal, it has a long experimental and theoretical history. The branching ratio of this decay has been computed in many models and QCD approximation starting from VMD (Vector Meson Dominance), and ending to ChPT (Chiral Perturbation Theory) with several low energy approximation schemes (ENJL, large N_c, unitary approach). The main part of these models predicts values far below the today measured value, and this has been a trouble for low energy effective theory for long time.

The PDG quoted value for the branching ratio is $Br(\eta \to \pi^0\gamma\gamma) = (7.2 \pm 1.4) \times 10^{-4}$, while the models give values about 1/2 lower. Recently a new result has come up from the Crystal Ball collaboration: $Br(\eta \to \pi^0\gamma\gamma) = (2.5 \pm 1.2) \times 10^{-4}$. This measurement is in better agreement with the theory, although it is affected by a large experimental systematic uncertainty due to the analysis procedure adopted. KLOE, with its high pure η sample, is able to give a more precise measurement of this branching ratio.

With the high η statistic collected we have also performed an upper limit evaluation on the $\eta \to \gamma\gamma\gamma$. It tests C violation in electromagnetic and strong interactions. The decay is possible in the Standard Model through weak interaction, but the predicted rate are far below today experimental sensitivity. So any measurement of a larger rate would be a clear signal of new physics. The limits on this branching ratio evaluated in this work is the world strongest limit nowadays available.

Contents

List of Figures

List of Tables

Chapter 1

Theoretical models for the $\eta \longrightarrow \pi^0\gamma\gamma$ decay.

In this chapter several theoretical model that have been used to predict the $\eta \to \pi^0\gamma\gamma$ branching ratio will be described. Special attention is given to ChPT prediction, whose calculation is described with some details. An introduction to ChPT is also given.

1.1 The QCD theory

In the framework of the Standard Model the strong interaction is described by the QCD (Quantum Chromo Dynamics). The QCD is a gauge theory whose gauge group is the color SU(3) group of the set of 3×3 complex matrices whose determinant is 1. The group operation is the usual raw by column multiplication between complex matrices. The dimension of the parameters space is 8, so the group has 8 generators. This means that the most general group element can be written as:

$$U = exp\left(-i\sum_{i=1}^{8}\alpha_i t^i\right)$$

where t^i are 3×3 Hermitean complex matrices, with trace equal to 0 and such that:

$$[t^i, t^j] = iC_{ijk}t^k$$

The C_{ijk} constants are not fully fixed by the group structure. Multiplying both the operators t^i as the structure constants C_{ijk} by a constant a one obtains the same group structure. To fix the a value one imposes the condition:

$$Tr(t^i t^j) = \frac{\delta^{ij}}{2}$$

The QCD Lagrangian for a 1/2 spin field ψ is:

$$\mathscr{L} = \bar{\psi}(i\not{D} - m)\psi - \frac{1}{4}\sum_{i=1}^{8} F^{i\mu\nu}F^{i}\mu\nu \tag{1.1}$$

where we have used the notation $\not{D} = D_\mu\gamma^\mu$ and

$$D_\mu = \partial_\mu - ig_s\sum_{i=1}^{8} t^i A^i_\mu.$$

$F_{\mu\nu}$ gives the propagation of the eight gluon fields A^i_μ, and is written as:

$$F^i_{\mu\nu} = \partial_\mu A^i_\nu - \partial_\nu A^i_\mu - g_s C_{ijk} A^j_\mu A^k_\nu$$

while g_s is the coupling constant of the gluons with the spinorial field ψ.
The spinorial field ψ can be seen as a set of three spinorial fields, one for each color (eigenstate of $SU(3)_C$). In the Lagrangian, the matrices t^i act on the color degrees of freedom while the matrix γ^μ are the 4 by 4 Dirac matrices acting on the spinorial degree of freedom. Here m is the mass of the field ψ that in the Standard Model is given by the spontaneous symmetry breaking mechanism through the introduction of the boson Higgs field H.

The Lagrangian (1.1) describes the QCD interaction for a single spinorial field. In the standard model the elementary fields that interact via strong interaction are 6, corresponding to the quark flavors u, d, c, s, t, b. So that the real QCD Lagrangian is the sum of (1.1) for each quark flavor.

1.2 The running of α_s and Λ_{QCD}

The problem of any Quantum Field Theory is to find the transition probability from a state $|\phi_I\rangle$ to a state $|\phi_F\rangle$, from which one can compute as many physical quantities as one wants. This can be computed starting from the total Lagrangian $\mathscr{L}$ of the theory using different approaches. Usually one proceeds to do a perturbative expansion of the transition amplitude respect to a parameter of the Lagrangian, for example the coupling constant ($\alpha_s = \frac{g_s^2}{4\pi}$ for the QCD). This means that for a given power of α_s one computes all possible Feynman diagrams that contribute to that power. Computing these diagrams one often finds divergences that compel to use particular technique to make them calculable. Usually the so called renormalization procedure is used.
The idea is to isolate the divergent terms from the not divergent terms (finite

terms). The divergent terms are written in such a way that the divergence is embedded in one or more parameters.
These parameters have different meaning, for different renormalization schemes. For example in the case of dimensional regularization one choses to perform integrals in a dimension in which the divergences disappear. Let's call this dimension $4-\epsilon$. When $\epsilon \to 0$ the integration dimension goes to 4 as the case of the physical space time, but the integral result diverges. One can often write the integral result as a sum of two pieces. A finite term and a one that is multiplied by a divergent factor $1/\epsilon$. In this way one has embedded the divergence of the integral in the parameter $1/\epsilon$.
The idea of regularization is to rewrite a parameter of the Lagrangian, for example α_s as a function of $1/\epsilon$ and the old parameter α_s^0, known as "bare" parameter. The value of α_s is obtained by measuring a physical observable depending from α_s. In this way the Feynman diagram, for any other process, can be computed because there isn't anymore a term in $1/\epsilon$ but simply the finite coupling constant α_s. In doing this job, the absorption of the divergence in the parameter, one often puts in the coupling constant not only the $1/\epsilon$ and α_s^0 terms but also finite term that are function, for example, of the energy s at which the process happens.
Due to these terms the coupling constant α_s is not a constant parameter anymore, but it is a function of the process energy s. This means that the "bare" coupling constant, that was used in the Lagrangian, has been replaced with a "running" coupling constant that is a function of s. The theory is able to predict the functional dependence of the running coupling constant by s. The functional dependence of α is still evaluated in perturbation theory, at 1-loop level one can show that in the limit of massless quarks:

$$\alpha(s) = \frac{\alpha}{1 - b\alpha ln\left(\frac{s}{\mu^2}\right)} \tag{1.2}$$

where:

$$b = \begin{cases} \sum_i \frac{N_C(Q_i^2)}{3\pi} & for\ QED \\ -\frac{11N_C - 2n_f}{12\pi} & for\ QCD \end{cases}$$

In these equations N_f is the number of coupled quarks. In QED i runs over all fermions, N_C is 3 for quarks and is 1 for leptons, while in QCD it runs only over the quarks. This is because both leptons and quarks interact via QED but only quarks interact via strong interaction.
Equation (1.2) must be used in the following way. If one knows the value of α at a given energy value s_0 (for example $s_0 = M_z$), one can set $\mu = s_0 = M_z$,

and the value of α at a different scale s is given by:

$$\alpha(s) = \frac{\alpha_{M_z}}{1 - b\alpha_{M_z} ln\left(\frac{s}{M_z^2}\right)}$$

In these equations only the coupled fermions must be included, that is only fermions with mass $m^2 \ll s$ must be taken into account in the sum. For example for $s \to +\infty$ all quarks and leptons must be included so:

$$\begin{aligned} b_{QED} &= \frac{\left(3\times\left(3\cdot\frac{4}{9}+3\cdot\frac{1}{9}\right)+1\times3\right)}{3\pi} = \frac{8}{3\pi} \\ b_{QCD} &= -\frac{(3\times11-2\times6)}{12\pi} = -\frac{7}{4\pi} \end{aligned}$$

The different sign between b_{QCD} and b_{QED} is responsible for the different asymptotic behavior. α_{QED} increases at high energy, reaching a pole at $b_{QED}\alpha_{M_z} ln\left(\frac{s_{pole}}{M_z^2}\right) = 1$.
Taking $b_{QED} = \frac{8}{3\pi}$, $M_z \sim 90GeV$ and $\alpha(M_z) \sim 1/127$ one finds $s_{pole}^{1/2} = 3 \times 10^{34} GeV$. For this reason we are allowed not to care about this problem. The situation is different for QCD, in fact α_{QCD} decreases with the energy, and the coupling constant goes to zero at high energy.
Nevertheless the pole is still present but at low energy. Using $b_{QCD} = -\frac{7}{4\pi}$ and $\alpha_s(M_z) \sim 0.12$ one finds $s_{pole}^{1/2} = 51MeV$. This value of the pole is wrong, because it has been evaluated using $n_f = 6$ but at energy around $\sim 1GeV$ the t, b, c quarks are decoupled, so the number of fermions to use is 3.
If we evaluate the equation 1.2 at an energy around 1 GeV and count $n_f = 3$ we set: $\alpha(m_\tau = 1.777\text{GeV}) = 0.35 \pm 0.03$ [1], $b_{QCD} = -\frac{9}{4\pi}$ and the pole is: $s_{pole}^{1/2} \sim 200 - 300MeV$. This means a big difference between QCD and QED. Perturbation theory can be used in QED to describe electromagnetic phenomena in all the physical range reachable at accelerators and the known universe, while perturbative QCD cannot be used for scale of $O(300MeV)$. This scale is known as Λ_{QCD}, it plays a fundamental role in the physics around and below 1 GeV. For this reason all $\sim 1GeV$ physics cannot be computed simply by perturbative QCD. Other approaches must be tried.

One possible approach is to use the symmetry properties of QCD to understand the low energy behavior. In the following we describe the *Chiral Perturbation Theory* that uses the Chiral symmetry of QCD to evaluate scattering amplitudes and decay rates of light particles.

1.3 Chiral symmetry in QCD

Given a spinor ψ we set the following definitions:

$$\psi_L = \frac{1}{2}(1-\gamma^5)\psi, \quad \psi_R = \frac{1}{2}(1+\gamma^5)\psi$$

from which:

$$\psi = \psi_L + \psi_R$$

Replacing this in equation (1.1) we obtain:

$$\mathscr{L} = (\bar{\psi}_L + \bar{\psi}_R)(iD_\mu\gamma^\mu - m)(\psi_L + \psi_R) + \ldots =$$

$$= i\bar{\psi}_L D_\mu\gamma^\mu\psi_L + i\bar{\psi}_R D_\mu\gamma^\mu\psi_R + i\bar{\psi}_R D_\mu\gamma^\mu\psi_L + i\bar{\psi}_L D_\mu\gamma^\mu\psi_R -$$
$$-m\bar{\psi}_L\psi_R - m\bar{\psi}_R\psi_L - m\bar{\psi}_L\psi_L - m\bar{\psi}_R\psi_R + \ldots$$

The terms $\bar{\psi}_R D_\mu\gamma^\mu\psi_L$, $\bar{\psi}_L D_\mu\gamma^\mu\psi_R$, $\bar{\psi}_L\psi_L$ and $\bar{\psi}_R\psi_R$ are null. In fact:

$$\bar{\psi}_R D_\mu\gamma^\mu\bar{\psi}_L = \overline{\left(\frac{1}{2}(1-\gamma^5)\psi\right)} D_\mu\gamma^\mu \left(\frac{1}{2}(1+\gamma^5)\psi\right) =$$

$$= \psi^\dagger\frac{1}{2}(1-\gamma^{5\dagger})\gamma^0 D_\mu\gamma^\mu\frac{1}{2}(1+\gamma^5)\psi$$

being $\gamma^{5\dagger} = \gamma^5$, $\gamma^5\gamma^\mu = -\gamma^\mu\gamma^5$ with $\mu = 0,1,2,3$ and ${\gamma^5}^2 = 1$ we have:

$$\psi^\dagger\gamma^0\frac{1}{2}(1+\gamma^5)D_\mu\gamma^\mu\frac{1}{2}(1+\gamma^5)\psi = \bar{\psi}D_\mu\gamma^\mu\frac{1}{2}(1-\gamma^5)\frac{1}{2}(1+\gamma^5)\psi =$$

$$= \bar{\psi}D_\mu\gamma^\mu\frac{1}{4}(1+\gamma^5-\gamma^5-\gamma^5\gamma^5)\psi = 0$$

Furthermore:

$$\bar{\psi}_L\psi_L = \overline{\left(\frac{1}{2}(1-\gamma^5)\psi\right)}\left(\frac{1}{2}(1-\gamma^5)\psi\right) = \frac{1}{2}\psi^\dagger(1-\gamma^5)\gamma^0\frac{1}{2}(1-\gamma^5)\psi =$$

$$= \bar{\psi}\frac{1}{2}(1+\gamma^5)(1-\gamma^5)\psi = 0$$

A similar demonstration can be done for the terms $\bar{\psi}_L D_\mu\gamma^\mu\psi_R$ and $\bar{\psi}_R\psi_R$. At the end the Lagrangian (1.1) can be written:

$$\mathscr{L} = i\bar{\psi}_L D_\mu\gamma^\mu\psi_L + i\bar{\psi}_R D_\mu\gamma^\mu\psi_R - m\bar{\psi}_L\psi_R - m\bar{\psi}_R\psi_L + \ldots$$

The field ψ is a spinorial field representing a point-like particle of mass m, in QCD we have 6 of such fields, representing the quarks: u, d, s, c, t, b. In

the low energy region, we are interested at, the quarks c, t, b decouple and don't give contributions to the interaction. For this reason we can limit our attention to light quarks u, d, s. The Lagrangian $\mathscr{L}$ is written in the form:

$$\mathscr{L} = \sum_{q=u,d,s} i\bar{\psi}_{qL} D_\mu \gamma^\mu \psi_{qL} + i\bar{\psi}_{qR} D_\mu \gamma^\mu \psi_{qR} - m_q \bar{\psi}_{qL} \psi_{qR} - m_q \bar{\psi}_{qR} \psi_{qL} + \dots \quad (1.3)$$

Now we define the following quantities:

$$\Psi_{L,R} = \begin{pmatrix} \psi_{uL,R} \\ \psi_{dL,R} \\ \psi_{sL,R} \end{pmatrix}; \quad \bar{\Psi}_{L,R} = \begin{pmatrix} \bar{\psi}_{uL,R} & \bar{\psi}_{dL,R} & \bar{\psi}_{sL,R} \end{pmatrix}$$

$$D_\mu \Psi_{L,R} = \begin{pmatrix} D_\mu \psi_{uL,R} \\ D_\mu \psi_{dL,R} \\ D_\mu \psi_{sL,R} \end{pmatrix}; \quad \bar{\Psi}\Psi = \sum_{i=u,d,s} \bar{\psi}_i \psi_i$$

where the spinor ψ_i can be the full spinor ψ or its projections ψ_L,ψ_R. Defining the quark mass matrix in this way:

$$M = \begin{pmatrix} m_u & 0 & 0 \\ 0 & m_d & 0 \\ 0 & 0 & m_s \end{pmatrix}$$

the Lagrangian 1.3 can be written in the compact form:

$$\mathscr{L} = i\bar{\Psi}_L D_\mu \gamma^\mu \Psi_L + i\bar{\Psi}_R D_\mu \gamma^\mu \Psi_R - \bar{\Psi}_L M \Psi_R - \bar{\Psi}_R M \Psi_L + \dots \quad (1.4)$$

This Lagrangian shows interesting symmetry properties under the following unitary transformations:

$$\Psi'_L = U_L \Psi_L \quad \Psi'_R = U_R \Psi_R \quad (1.5)$$

where U_L and U_R are independent 3×3 unitary matrices. The Lagrangian $\mathscr{L}'$ after this transformation is:

$$\mathscr{L}' = i\bar{\Psi}'_L D_\mu \gamma^\mu \Psi'_L + i\bar{\Psi}'_R D_\mu \gamma^\mu \Psi'_R - \bar{\Psi}'_L M \Psi'_R - \bar{\Psi}'_R M \Psi'_L + \dots =$$

$$= i\overline{(U_L\Psi_L)} D_\mu \gamma^\mu U_L \Psi_L + i\overline{(U_R\Psi_R)} D_\mu \gamma^\mu U_R \Psi_R - \overline{(U_L\Psi_L)} M U_R \Psi_R - \overline{(U_R\Psi_R)} M U_L \Psi_L + \dots$$

If we indicate with a subscript k the k^{th} component of the array Ψ we can write:

$$\bar{\Psi}'_k = \overline{\left(\sum_{j=1}^{3} U_{kj} \psi_j \right)} = \left(\sum_{j=1}^{3} U_{kj} \psi_j \right)^\dagger \gamma^0 = \sum_{j=1}^{3} \psi_j^\dagger \gamma^0 U_{kj}^* = \sum_{j=1}^{3} \psi_j^\dagger \gamma^0 U_{jk}^\dagger = (\bar{\Psi} U^\dagger)_k$$

and

$$\mathscr{L}' = i\bar{\Psi}_L U_L^\dagger D_\mu \gamma^\mu U_L \Psi_L + i\bar{\Psi}_R U_R^\dagger D_\mu \gamma^\mu U_R \Psi_R - \bar{\Psi}_L U_L^\dagger M U_R \Psi_R - \bar{\Psi}_R U_R^\dagger M U_L \Psi_L + \dots$$

and using the property: $U^\dagger U = 1$, one finds:

$$\mathscr{L}' = i\bar{\Psi}_L D_\mu \gamma^\mu \Psi_L + i\bar{\Psi}_R D_\mu \gamma^\mu \Psi_R - \bar{\Psi}_L U_L^\dagger M U_R \Psi_R - \bar{\Psi}_R U_R^\dagger M U_L \Psi_L + \dots$$

If M was 0 (that is the quark masses was null) the QCD Lagrangian would be invariant under the two transformations (1.5), these transformations are called *Chiral transformations* and the Lagrangian symmetry *Chiral symmetry.*

If the mass of the quark are small respect to the energy scale at which we compute physical quantities the Chiral symmetry is partially broken. Anyway it can be used to do prediction about the phenomenology of the quark interaction and the bound state spectroscopy.

Let's define the Weyl representation of the spinor Ψ:

$$\Psi = \begin{pmatrix} \Psi_L \\ \Psi_R \end{pmatrix}$$

and, given a chiral transformation (U_L, U_R) we define the following auxiliary matrix:

$$U_V = \frac{1}{2}(U_R + U_L) \quad U_A = \frac{1}{2}(U_R - U_L)$$

A Chiral transformation such that $U_A = 0$ is called a vectorial transformation while a Chiral transformation in which $U_V = 0$ is called an axial transformation, the reason for that will be explained in the following. The QCD Lagrangian with $M = 0$ is of course invariant under both transformations. The QCD vacuum, instead, shows different behavior for vectorial and axial transformations. Both the unitary matrix U_V and U_A can be written as:

$$U_V = e^{i\alpha_V} S_V \quad U_A = e^{i\alpha_A} S_A$$

where S_V and S_A are unitary matrix such that: $detS_{V,A} = 1$. The matrix group S_V and S_A belong to $SU(3)$. It has eight generators Λ^a, the generator of the group that gives the phase transformation is the identity matrix 1. A chiral transformation on Ψ can be written as:

$$\begin{pmatrix} \Psi'_L \\ \Psi'_R \end{pmatrix} = \begin{pmatrix} U_L & 0 \\ 0 & U_R \end{pmatrix} \begin{pmatrix} \Psi_L \\ \Psi_R \end{pmatrix}$$

In the vectorial case, being $U_A = 0$ one has $U_L = U_R = U_V$, while in the axial case, being $U_V = 0$ one has $U_L = -U_R = U_A$. So that one has:

$$\begin{pmatrix} \Psi'_L \\ \Psi'_R \end{pmatrix} = \underbrace{\begin{pmatrix} U_V & 0 \\ 0 & U_V \end{pmatrix}}_{Vector} \begin{pmatrix} \Psi_L \\ \Psi_R \end{pmatrix} \quad \begin{pmatrix} \Psi'_L \\ \Psi'_R \end{pmatrix} = \underbrace{\begin{pmatrix} -U_A & 0 \\ 0 & +U_A \end{pmatrix}}_{Axial} \begin{pmatrix} \Psi_L \\ \Psi_R \end{pmatrix}$$

or again:

$$\begin{pmatrix} \Psi'_L \\ \Psi'_R \end{pmatrix} = U_V \begin{pmatrix} 1 & 0 \\ 0 & 1 \end{pmatrix} \begin{pmatrix} \Psi_L \\ \Psi_R \end{pmatrix} \quad \begin{pmatrix} \Psi'_L \\ \Psi'_R \end{pmatrix} = U_A \begin{pmatrix} -1 & 0 \\ 0 & 1 \end{pmatrix} \begin{pmatrix} \Psi_L \\ \Psi_R \end{pmatrix}$$

The matrix $\begin{pmatrix} -1 & 0 \\ 0 & 1 \end{pmatrix}$ is γ^5 in the Weyl representation, in fact:

$$\gamma^5\Psi_L = \gamma^5\frac{1}{2}(1-\gamma^5)\Psi = \frac{1}{2}(\gamma^5-1)\Psi = -\frac{1}{2}(1-\gamma^5)\Psi = -1\Psi_L$$

$$\gamma^5\Psi_R = \gamma^5\frac{1}{2}(1+\gamma^5)\Psi = \frac{1}{2}(\gamma^5+1)\Psi = -\frac{1}{2}(1+\gamma^5)\Psi = +1\Psi_R$$

so that we can write:

$$\Psi' = U_V\Psi \quad \textit{Vector} \qquad \Psi' = U_A\gamma^5\Psi \quad \textit{Axial}$$

Now we indicate with Λ^0 the generator of $U(1)$ Group and Λ^i $(i = 1, \ldots, 8)$ the generators of $SU(3)$ group. Under an infinitesimal transformation $\theta^a_{V,A}$ around the direction a of these groups we have:

$$\Psi' = (1 + i\Lambda^a\delta\theta^a_V)\Psi \quad \Psi' = (1 + i\Lambda^a\delta\theta^a_A)\gamma^5\Psi$$

The currents associated to these transformations are:

$$J^{\mu,a}_V = \bar{\Psi}\gamma^\mu\Lambda^a\Psi \quad J^{\mu,a}_A = \bar{\Psi}\gamma^\mu\gamma^5\Lambda^a\Psi$$

These two currents are both classical conserved in the limit in which $M = 0$ for the Noether's theorem. Anyway it can be demonstrated [2] that quantum correction due to the gluon anomaly make the quantity $\partial_\mu J^{\mu,0} \neq 0$. This problem is known as $U(1)_A$ anomaly and is responsible for the breaking of $U(1)_A$ symmetry at quantum level.
Now we find the transformation properties of the currents $J^{\mu,a}_V$ and $J^{\mu,a}_A$ under parity. A spinor transforms under parity according:

$$\Psi_P = \gamma^0\Psi$$

so:

$${J^{\mu,a}_V}_P = \bar{\Psi}_P\gamma^\mu\Lambda^a\Psi_P = \bar{\Psi}\gamma^0\gamma^\mu\Lambda^a\gamma^0\Psi = \begin{cases} \bar{\Psi}\gamma^0\Lambda^a\Psi = & J^{0,a}_V & \mu = 0 \\ -\bar{\Psi}\gamma^\mu\Lambda^a\Psi = & -J^{\mu,a}_V & \mu = 1,2,3 \end{cases}$$

$${J^{\mu,a}_A}_P = \bar{\Psi}_P\gamma^\mu\gamma^5\Lambda^a\Psi_P = \bar{\Psi}\gamma^0\gamma^\mu\gamma^5\Lambda^a\gamma^0\Psi =$$

$$= -\bar{\Psi}\gamma^0\gamma^\mu\gamma^0\gamma^5\Lambda^a\Psi = \begin{cases} -\bar{\Psi}\gamma^0\gamma^5\Lambda^a\Psi = & -J^{0,a}_A & \mu = 0 \\ +\bar{\Psi}\gamma^\mu\gamma^5\Lambda^a\Psi = & +J^{\mu,a}_A & \mu = 1,2,3 \end{cases}$$

In other words the time component of $J_V^{\mu,a}$ ($J_A^{\mu,a}$) transforms as a scalar (pseudo-scalar) while the spatial components transform as a vector (pseudo-vector). This is the reason why $J_V^{\mu,a}$ is called vector and $J_A^{\mu,a}$ axial. One can demonstrate that the charge associated to the current $J_V^{\mu,a}$ $\left(Q_V^a = \int J_V^{0,a} d^3x\right)$ annihilate the vacuum, that is $Q_V^a |0\rangle = 0$ [3]. A symmetry that has this property is called exact. The symmetry is reproduced in the spectrum of the theory in the sense that particles belonging to the same representation of the symmetry group have equal masses.
For the axial current $Q_A^a |0\rangle \neq 0$. The derivation of this property from the QCD Lagrangian is still missing. The property can be deduced from the particles spectrum. In fact if $Q_A^a |0\rangle$ was equal to 0 we should see for each particle with given parity a particle with opposite parity and same mass, but it is not observed.
A symmetry such that $\partial_\mu J^\mu = 0$ and $Q |0\rangle \neq 0$ is called *spontaneously broken*. In this case the Goldstone theorem [4] asserts that as many null mass boson particles must be in the theory spectrum, as the charges, which don't annihilate the vacuum.
These particles are called *Goldstone bosons*. The Goldstone bosons have the same transformation properties and the same quantum numbers of the charge which they are associated to. In the case of the axial symmetry they are pseudo-scalars, as the Q_A^a charges. The Q_A^a charges are eight, where a runs from 1 to 8 (the current $J_A^{\mu,0}$ is not conserved due to $U(1)_A$ anomaly) and so we must have eight null mass pseudo-scalar particles. We know that in the hadron spectrum there aren't eight null mass particles, the reason for this is that the axial symmetry is only an approximation of a spontaneous broken symmetry. In fact, it would be if the quark mass matrix was the null matrix, but it isn't. For this reason the eight Goldstone bosons acquire a mass proportional to the breaking of the symmetry, that is the quark masses.
The quark mass matrix for u, d, s is the following[1]:

$$M = \begin{pmatrix} 1.4 - 4 & 0 & 0 \\ 0 & 4 - 8 & 0 \\ 0 & 0 & 80 - 130 \end{pmatrix} \quad \mathrm{MeV/c^2}$$

As we can see the u and d quarks are much lighter than the s quark, therefore one would expect that the $SU(2)_A$ subgroup of the $SU(3)_A$ is a better approximation of a spontaneous broken symmetry than the $SU(3)_A$ itself. So the Goldstone boson associated to the $SU(2)_A$ subgroup must be lighter than the other one.
This is exactly what happens in the light meson spectrum (see fig. 1.1). There are three mesons, the pions, π^+, π^-, π^0 that are a representation of the $SU(2)$ subgroup that are very light, they are the lightest hadrons with

mass around $130MeV$, then we have the remaining pseudo-scalar mesons with mass around $550MeV$ that complete, together with the pions, an $SU(3)$ representation.

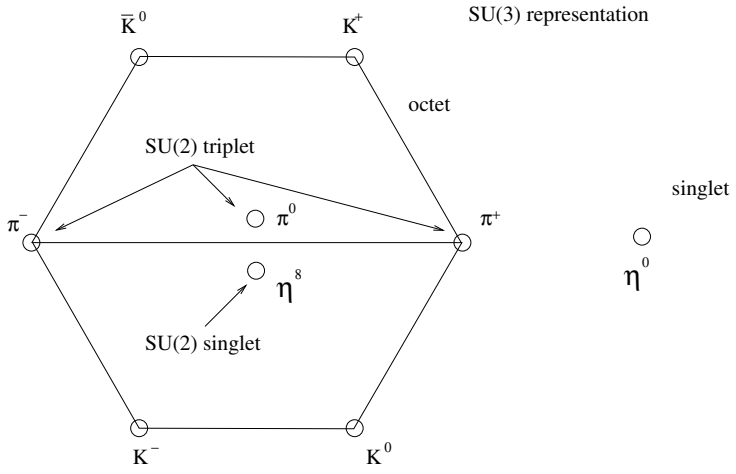

Figure 1.1: Light mesons spectrum, the $SU(2)$ subgroup is shown.

1.4 The low energy theorem and the Chiral expansion

As we have shown before the interaction among quarks diverges at energy scale of $O(\Lambda_{QCD})$, making the perturbation expansion de facto impossible. On the contrary it can be demonstrated that the interaction among the Goldstone bosons goes to zero when the interacting particles energy goes to zero. Usually the interaction between pions in $\pi\pi \to \pi\pi$ process is expressed in terms of scattering length. In other terms the scattering length should go to zero as the pion kinetic energy goes to 0. In reality this doesn't happen exactly, because the Chiral symmetry is explicitly broken by the mass terms in the Lagrangian, so the scattering length in the limit $E \to 0$ is [5]:

$$a_0^0 = \frac{7m_\pi^2}{32\pi F_\pi^2} = 0.159$$

Where F_π is the π decay constant.
Anyway the fact that the coupling among bosons vanishes when the energy goes to zero, is the main ingredient for ChPT. The idea is to do a power

expansion in terms of momenta and quark masses. So we build a Lagrangian in which the interacting fields are not the quark fields but the Goldstone boson fields. The Lagrangian is built in such a way to preserve chiral and Lorentz invariance.
For technical reasons the Goldstone bosons fields are usually collected in a matrix. This matrix is called P_8 and has the following form:

$$P_8 = \begin{pmatrix} \frac{\pi^0}{\sqrt{2}} + \frac{\eta_8}{\sqrt{6}} & \pi^+ & K^+ \\ \pi^- & -\frac{\pi^0}{\sqrt{2}} + \frac{\eta_8}{\sqrt{6}} & K^0 \\ K^- & \bar{K}^0 & -\frac{2}{\sqrt{6}}\eta_8 \end{pmatrix}$$

The matrix used in the Lagrangian is $\Sigma = exp\left(\frac{\sqrt{2}i}{F_\pi}P_8\right)$. This matrix has very nice transformation properties under Chiral transformation $SU(3)_L \times SU(3)_R$, that is $\Sigma \to S_L \Sigma S_R^\dagger$; where S_L, S_R are unitary matrices with determinant equal to 1. With this definition is very simple to build Chiral invariant terms. In fact any term of the type:

$$Tr(L\Sigma M\Sigma^\dagger)$$

where L and M are linear operators commuting with S_L, S_R is invariant under chiral transformation. In fact:

$$Tr[L\Sigma' M\Sigma'^\dagger] = Tr[LS_L\Sigma S_R^\dagger M(S_L\Sigma S_R^\dagger)^\dagger] =$$

$$= Tr[S_L L\Sigma S_R^\dagger M S_R \Sigma^\dagger S_L^\dagger] = Tr[L\Sigma S_R^\dagger S_R M\Sigma^\dagger S_L^\dagger S_L] = Tr(L\Sigma M\Sigma^\dagger)$$

Lorentz invariance also restricts the type of terms that one can have in the Lagrangian. Being Σ a scalar field, the only kinetic Lorentz and Chiral invariant term is:

$$Tr(\partial_\mu \Sigma \partial^\mu \Sigma^\dagger)$$

The electromagnetic interaction is introduced in the Lagrangian through the covariant derivative definition:

$$D_\mu = \partial_\mu + ieA_\mu[Q, \Sigma]$$

where Q is the quark charge matrix:

$$Q = \begin{pmatrix} \frac{2}{3} & 0 & 0 \\ 0 & -\frac{1}{3} & 0 \\ 0 & 0 & -\frac{1}{3} \end{pmatrix}$$

To introduce the Chiral symmetry breaking terms one proceeds in this way. First we observe that the Lagrangian (1.4) is still invariant under U_R,U_L

transformations if at the same time the mass matrix M transforms in this way:

$$M' = U_R M U_L^\dagger$$

So we must add the mass term to the Chiral Lagrangian in such way to preserve this invariance. If we think to expand the Lagrangian respect to quark masses the first symmetry breaking term in this expansion would be:

$$\mathscr{L}_{sb} = f(\Sigma, \partial\Sigma, ...) \times M$$

At leading order in an expansion of both, powers of M and powers of momenta (derivatives), the symmetry breaking term reduces to $f(\Sigma)\times M$. Moreover, this expression must be invariant under simultaneous transformations of Σ and M. The only invariant of this type is $tr(M\Sigma^\dagger)$ and its complex conjugate. Hence the leading symmetry breaking term is of the form:

$$\mathscr{L}_{sb} = \frac{F_\pi^2}{2} B tr M(\Sigma^\dagger + \Sigma)$$

Adding this term to the Chiral Lagrangian and expanding the Σ matrix as a power of the pion field, one can show that the pion mass is given by:

$$m_\pi^2 = (m_u + m_d)B(1 + O(M))$$

So the pion mass is linear in the quark masses. If we indicate with p_π the pion momentum one can write $p_\pi^2 = m_\pi^2$, this means that $(m_u + m_d) \sim p_\pi^2$. For this reason the mass matrix counts as two power of momenta in the Chiral Lagrangian expansion.
In the same way one can extract the following relations for the Goldstone bosons masses:

$$\begin{array}{ll} m_\pi^2 = B(m_u + m_d) & m_{K^\pm}^2 = B(m_s + m_u) \\ m_{K^0}^2 = B(m_s + m_d) & m_{\eta_8}^2 = \frac{1}{3}B(4m_s + m_u + m_d) \end{array}$$

From which one find:

$$\frac{1}{2}\frac{m_u + m_d}{2m_K^2 - m_\pi^2} \sim \frac{1}{26}$$

There are some estimates for the m_s mass that should lie in the range 150 - 300 MeV/c^2. From which one can extract the value of $m_u + m_d$ quantity and from the m_π^2 the B value.

Introducing the notation $\chi = 2BM$, the lowest order ChPT Lagrangian can be written in the form:

$$\mathscr{L}_2 = \frac{F_\pi^2}{4} tr(D_\mu \Sigma D^\mu \Sigma^\dagger + \chi\Sigma^\dagger + \chi^\dagger \Sigma)$$

The tree diagram are obtained simply by the terms in $\mathscr{L}_2$. This is done by expanding Σ as a function of P_8:

$$\Sigma = exp(\frac{\sqrt{2}i}{F_\pi} P_8) = 1 + \frac{2i}{F_\pi} P_8 + \frac{1}{2}\left(\frac{2i}{F_\pi}\right)^2 P_8^2 + \dots$$

In this way the terms with two powers of P_8 give vertices with two Goldstone bosons, those with four power 4 Goldstone bosons etc. The photon coupling is given by the terms with A_μ coming from the covariant derivative.
Of course these are all tree level diagrams, starting from two vertices of $\mathscr{L}_2$ one can build also loop terms. Each term having a derivative gives a p^μ contribution to the vertex in momenta representation, so the tree level vertex are $O(p^2)$. Diagrams with two $\mathscr{L}_2$ vertices are $O(p^4)$. Often these terms are divergent and must be regularized.
Unfortunately the Chiral Lagrangian is not renormalizable. Hence differently from the QCD, we cannot absorb divergences in a finite number of Lagrangian parameters. To restore renormalizability we must add, order by order, new terms to the Lagrangian, known as counterterms. So that new tree level vertices of $O(p^4)$ must be added to the $\mathscr{L}_2$ that are needed to absorb divergent terms from $\mathscr{L}_2$ loops. And so on.
At the end the Chiral Lagrangian is a sum of $\mathscr{L}_2$ and all its possible counterterms:

$$\mathscr{L}_{ChPT} = \mathscr{L}_2 + \mathscr{L}_4 + \mathscr{L}_6 + \dots$$

Note that the term of the Chiral expansion are even in p. This comes from Lorentz invariance that compels to build terms with an even number of derivatives to saturate Lorentz indices. These derivatives give rise to the p^μ term in momentum space when Feynman diagrams are built. To calculate an amplitude at a given order in p one must take all terms of that order, including loop corrections, taking into account the counterterms and counting the mass term as two powers of momenta.

1.5 $\eta \to \pi^0\gamma\gamma$ amplitude in ChPT.

Now we evaluate the $\eta \to \pi^0\gamma\gamma$ amplitude in ChPT framework. $O(p^2)$ contributions can come only from tree level diagrams in $\mathscr{L}_2$, in particular diagrams

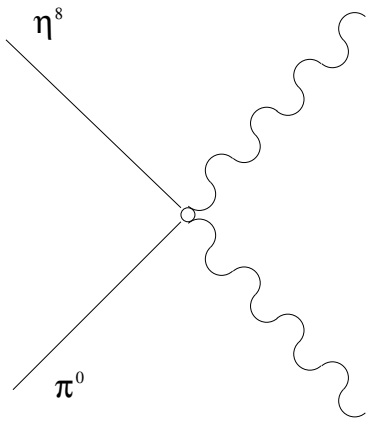

Figure 1.2: p^2 Feynman diagram from $\mathscr{L}_2$.

with only one vertex. Two photons and two Goldstone bosons (the π^0 and the η) must be linked to this vertex (see fig. 1.2). The only terms with two photons, come from the covariant derivative D_μ. Hence we focus our attention on the term $tr(D_\mu \Sigma D^\mu \Sigma^\dagger)$ and we extract: $tr\left(ieA_\mu[Q,\Sigma]\Sigma\right)\left(ieA^\mu[Q,\Sigma]\Sigma^\dagger\right)$. In expanding Σ to have the right linked legs, we observe that the Σ in the commutator must be expanded at least at the term in P_8 otherwise the commutator, therefore the term, vanishes.
So we must write: $-e^2 A^\mu A_\mu tr\left[Q, \frac{\sqrt{2}i}{F_\pi}P_8\right]\Sigma\left[Q, \frac{\sqrt{2}i}{F_\pi}P_8\right]\Sigma^\dagger$. Due to the two P_8 terms we have yet a coupling to two mesons, so the remaining two Σ terms can be expanded only to the first term (the identity 1).
Hence we have:

$$+e^2\frac{2}{F_\pi^2}A^\mu A_\mu tr\left[Q,P_8\right]^2 \tag{1.6}$$

being

$$[Q,P_8] = \begin{pmatrix} 0 & \pi^+ & K^+ \\ -\pi^- & 0 & 0 \\ -K^- & 0 & 0 \end{pmatrix}$$

there cannot be a vertex of the type given in fig.(1.2), It is because no π^0 and η field appear in the matrix. This is a general property: only the charged meson couples directly to a photon in a vertex. It depends on the structure of Q and P_8 matrices. For this reason the $\eta \to \pi^0\gamma\gamma$ amplitude vanishes at $O(p^2)$. Higher p orders must be evaluated.
Let's evaluate the amplitude at p^4 order. The contribution to this order comes from tree diagrams from vertices in $\mathscr{L}_4$, or from two $\mathscr{L}_2$ vertices. We begin to search for contributions from 2 $\mathscr{L}_2$ vertices.

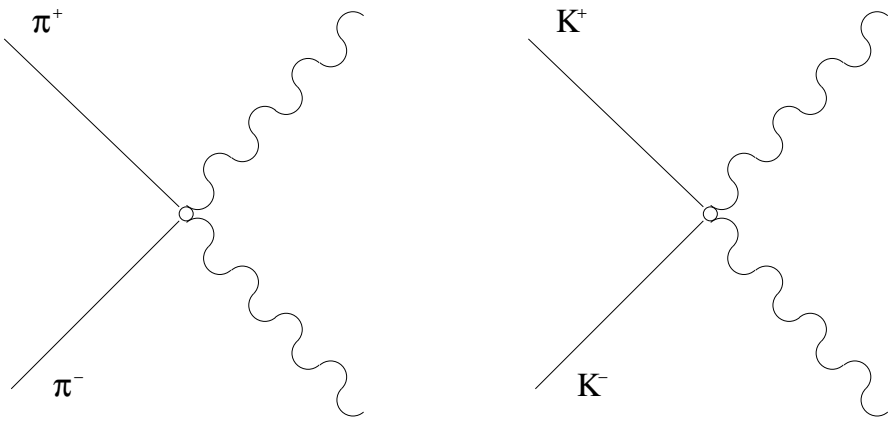

Figure 1.3: Feynman diagrams of the vertices from $\mathscr{L}_2$ with a coupling to two photons.

Let's compute the trace in the expression (1.6), we have:

$$+e^2\frac{2}{F_\pi^2}A^\mu A_\mu tr\left[Q,P_8\right]^2 = +e^2\frac{2}{F_\pi^2}A^\mu A_\mu tr\begin{pmatrix} 0 & \pi^+ & K^+ \\ -\pi^- & 0 & 0 \\ -K^- & 0 & 0 \end{pmatrix}^2 =$$

$$+e^2\frac{2}{F_\pi^2}A^\mu A_\mu tr\begin{pmatrix} -\pi^+\pi^- - K^+K^- & 0 & 0 \\ 0 & -\pi^+\pi^- & -\pi^-K^+ \\ 0 & -K^-\pi^+ & -K^-K^+ \end{pmatrix} =$$

$$= -2e^2\frac{2}{F_\pi^2}\left(A^\mu A_\mu \pi^+\pi^- + A^\mu A_\mu K^+K^-\right)$$

These two terms are the only ones coupled to two photons in $\mathscr{L}_2$. They correspond to the Feynman diagrams shown in fig. (1.3).

Now we search for any 4 mesons vertices with at least η and π^0 legs. These vertices can come only from the term $tr\left(\partial_\mu\Sigma\partial^\mu\Sigma^\dagger\right)$ because we don't want a photon attached to the vertex. So we must take all terms with four power of P_8 from Σ expansion. These are terms of the form:

$$\partial_\mu P_8\partial^\mu P_8^{3\dagger};\quad \partial_\mu P_8^2\partial^\mu P_8^{2\dagger};\quad \partial_\mu P_8^3\partial^\mu P_8^{\dagger}.$$

We must compute the quantities P_8^2 and P_8^3.

$$P_8^2 = \begin{pmatrix} \left(\frac{\pi^0}{\sqrt{2}}+\frac{\eta_8}{\sqrt{6}}\right)^2+\pi^+\pi^-+K^+K^- & \frac{2}{\sqrt{6}}\eta_8\pi^+ + K^+\bar{K}^0 & \frac{\pi^0K^+}{\sqrt{2}}+\pi^+K^0-\frac{\eta_8K^+}{\sqrt{6}} \\ \frac{2}{\sqrt{6}}\eta_8\pi^- + K^0K^- & \pi^-\pi^+ + \left(-\frac{\pi^0}{\sqrt{2}}+\frac{\eta_8}{\sqrt{6}}\right)^2 + K^0\bar{K}^0 & \pi^-K^+ - \frac{\pi^0}{\sqrt{2}}K^0 - \frac{\eta_8}{\sqrt{6}}K^0 \\ \frac{\pi^0K^-}{\sqrt{2}} - \frac{\eta_8K^-}{\sqrt{6}} + \pi^-\bar{K}^0 & K^-\pi^+ - \frac{\pi^0\bar{K}^0}{\sqrt{2}} - \frac{\eta_8\bar{K}^0}{\sqrt{6}} & K^-K^+ + K^0\bar{K}^0 + \frac{2}{3}\eta_8^2 \end{pmatrix}$$

In evaluating P_8^3, to simplify calculation, we take in account only terms that can contribute to a vertex with one π^0 leg and/or one η_8 leg. So each term with two or more π^0 or η_8 or with none of the two is discarded. With this simplification P_8^3 is:

$$P_8^3 = \begin{pmatrix} \frac{\pi^+\pi^-\pi^0}{\sqrt{2}} + \sqrt{\frac{3}{2}}\pi^+\pi^-\eta_8 + & 0 & 0 \\ +\sqrt{2}\pi^0 K^+ K^- & & \\ 0 & \sqrt{\frac{3}{2}}\eta_8\pi^+\pi^- - \frac{\pi^0\pi^+\pi^-}{\sqrt{2}} - & 0 \\ & -\sqrt{2}\pi^0 K^0 \bar{K}^0 & \\ 0 & 0 & \left(\frac{\pi^0}{\sqrt{2}} - \sqrt{\frac{3}{2}}\eta_8\right) K^- K^+ - \\ & & -\left(\sqrt{\frac{3}{2}}\eta_8 + \frac{\pi^0}{\sqrt{2}}\right) K^0 \bar{K}^0 \end{pmatrix}$$

Let's start to evaluate the quantity $\partial_\mu P_8^2 \partial^\mu P_8^{2\dagger}$ using the same prescription used to evaluate P_8^3. But now we want one π^0 and one η_8 in the product of the fields. In adjoint we are interested only to diagonal terms because at the end we must compute a trace, so:

$$\begin{aligned}
\left(\partial_\mu P_8^2 \partial^\mu P_8^{2\dagger}\right)_{11} &= \frac{\partial_\mu(\pi^0\eta_8)\partial^\mu(\pi^{+*}\pi^{-*})}{\sqrt{3}} + \frac{\partial_\mu(\pi^0\eta_8)\partial^\mu(K^{+*}K^{-*})}{\sqrt{3}} + \\
&+ \frac{\partial_\mu(\pi^+\pi^-)\partial^\mu(\pi^{0*}\eta_8{}^*)}{\sqrt{3}} + \frac{\partial_\mu(K^+K^-)\partial^\mu(\pi^{0*}\eta_8{}^*)}{\sqrt{3}} + \\
&- \frac{\partial_\mu(\pi^0 K^+)\partial^\mu(\eta_8{}^* K^{+*})}{\sqrt{12}} - \frac{\partial_\mu(\eta_8 K^+)\partial^\mu(\pi^{0*} K^{+*})}{\sqrt{12}} \\
\left(\partial_\mu P_8^2 \partial^\mu P_8^{2\dagger}\right)_{22} &= - \frac{\partial_\mu(\pi^-\pi^+)\partial^\mu(\pi^{0*}\eta_8{}^*)}{\sqrt{3}} - \frac{\partial_\mu(\pi^0\eta_8)\partial^\mu(\pi^{+*}\pi^{-*})}{\sqrt{3}} + \\
&- \frac{\partial_\mu(\pi^0\eta_8)\partial^\mu(K^{0*}\bar{K}^{0*})}{\sqrt{3}} - \frac{\partial_\mu(K^0\bar{K}^0)\partial^\mu(\pi^{0*}\eta_8{}^*)}{\sqrt{3}} + \\
&+ \frac{\partial_\mu(\pi^0 K^0)\partial^\mu(\eta_8{}^* K^{0*})}{\sqrt{12}} + \frac{\partial_\mu(\eta_8 K^0)\partial^\mu(\pi^{0*} K^{0*})}{\sqrt{12}} \\
\left(\partial_\mu P_8^2 \partial^\mu P_8^{2\dagger}\right)_{33} &= - \frac{\partial_\mu(\pi^0 K^-)\partial^\mu(\eta_8{}^* K^{-*})}{\sqrt{12}} - \frac{\partial_\mu(\eta_8 K^-)\partial^\mu(\pi^{0*} K^{-*})}{\sqrt{12}} + \\
&+ \frac{\partial_\mu(\pi^0\bar{K}^0)\partial^\mu(\eta_8{}^*\bar{K}^{0*})}{\sqrt{12}} + \frac{\partial_\mu(\eta_8\bar{K}^0)\partial^\mu(\pi^{0*}\bar{K}^{0*})}{\sqrt{12}}
\end{aligned}$$

Summing all these terms one obtains:

$$\begin{aligned}
Tr\left(\partial_\mu P_8^2 \partial^\mu P_8^{2\dagger}\right) &= \frac{\partial_\mu(\pi^0\eta_8)\partial^\mu(K^{+*}K^{-*})}{\sqrt{3}} + \frac{\partial_\mu(K^+K^-)\partial^\mu(\pi^{0*}\eta_8{}^*)}{\sqrt{3}} + \\
&- \frac{\partial_\mu(\pi^0 K^+)\partial^\mu(\eta_8{}^* K^{+*})}{\sqrt{12}} - \frac{\partial_\mu(\eta_8 K^+)\partial^\mu(\pi^{0*} K^{+*})}{\sqrt{12}} + \\
&- \frac{\partial_\mu(\pi^0\eta_8)\partial^\mu(K^{0*}\bar{K}^{0*})}{\sqrt{3}} - \frac{\partial_\mu(K^0\bar{K}^0)\partial^\mu(\pi^{0*}\eta_8{}^*)}{\sqrt{3}} +
\end{aligned}$$

$$+\frac{\partial_\mu(\pi^0 K^0)\partial^\mu({\eta_8}^* K^{0*})}{\sqrt{12}}+\frac{\partial_\mu(\eta_8 K^0)\partial^\mu(\pi^{0*} K^{0*})}{\sqrt{12}}+$$
$$-\frac{\partial_\mu(\pi^0 K^-)\partial^\mu({\eta_8}^* K^{-*})}{\sqrt{12}}-\frac{\partial_\mu(\eta_8 K^-)\partial^\mu(\pi^{0*} K^{-*})}{\sqrt{12}}+$$
$$+\frac{\partial_\mu(\pi^0 \bar{K}^0)\partial^\mu({\eta_8}^* \bar{K}^{0*})}{\sqrt{12}}+\frac{\partial_\mu(\eta_8 \bar{K}^0)\partial^\mu(\pi^{0*} \bar{K}^{0*})}{\sqrt{12}}$$

Can be easily demonstrated that $Tr\left(\partial_\mu P_8 \partial^\mu P_8^{3\dagger}\right) = 0$ while:

$$Tr\left(\partial_\mu P_8^3 \partial^\mu P_8^\dagger\right) = Tr\left(\partial_\mu P_8 \partial^\mu P_8^{3\dagger}\right)^\dagger = Tr^*\left(\partial_\mu P_8 \partial^\mu P_8^{3\dagger}\right) = 0$$

So vertices with four mesons and one π^0 and one η_8 come from $Tr\left(\partial_\mu P_8^2 \partial^\mu P_8^{2\dagger}\right)$. They correspond to the Feynman diagrams shown in fig. (1.4).

As one can see in our calculation a vertex of the type $\pi^+\pi^-\pi^0\eta_8$ is present

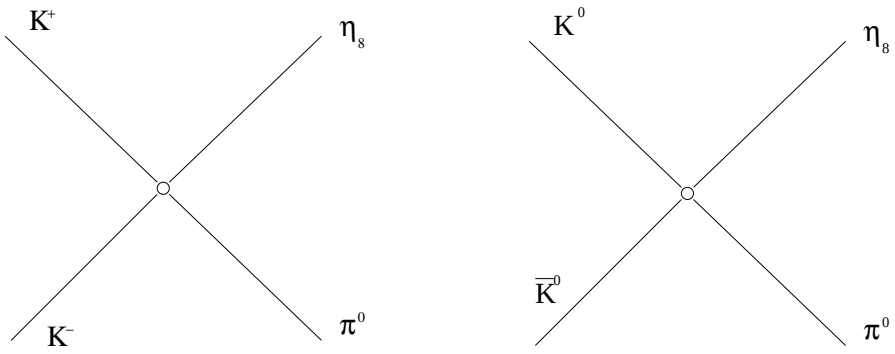

Figure 1.4: Feynman diagrams corresponding to vertices with four legs with one π^0 and one η^8 leg.

in the diagonal term of the matrix $\partial_\mu P_8^2 \partial^\mu P_8^{2\dagger}$ but it disappears in the trace due to a cancellation between the elements. This is not accidental. In fact the term $\partial_\mu \Sigma \partial^\mu \Sigma^\dagger$ is invariant under $SU(3)$. It is also invariant under the subgroup $SU(2)$ of the isospin I. And a vertex of this type violates isospin having π^+, π^- and π^0 odd G-Parity and η_8 even G-Parity. A vertex of this type appears instead in the mass term $Tr(\chi\Sigma^\dagger + \chi^\dagger\Sigma)$ where $\chi = 2BM$:

$$M = \begin{pmatrix} m_u & 0 & 0 \\ 0 & m_d & 0 \\ 0 & 0 & m_s \end{pmatrix}.$$

Here we look for a 4 legs vertex so we must expand Σ at the term P_8^4. Now we compute this quantity taking into account that at the end we must compute

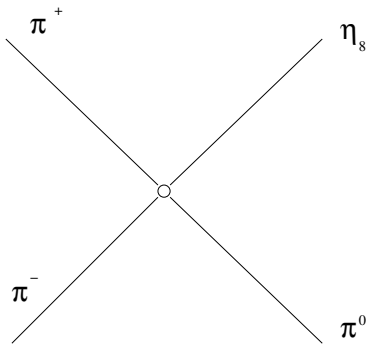

Figure 1.5: G-parity violating vertex for $\eta \to \pi^0\gamma\gamma$ amplitude.

a trace and we are interested only to $\pi^0\eta_8$ vertices. So we have:

$$\begin{aligned}
(P_8^4)_{11} &= \frac{2\sqrt{3}}{3}\pi^+\pi^-\eta_8\pi^0 + \frac{\sqrt{3}}{3}\eta_8\pi^0K^+K^- \\
(P_8^4)_{22} &= -\frac{2\sqrt{3}}{3}\pi^+\pi^-\eta_8\pi^0 + \frac{\sqrt{3}}{3}\eta_8\pi^0K^0\bar{K}^0 \\
(P_8^4)_{33} &= -\frac{\sqrt{3}}{3}\eta_8\pi^0K^+K^+ + \frac{\sqrt{3}}{3}\eta_8\pi^0K^0\bar{K}^0
\end{aligned}$$

Multiplying this matrix for the diagonal matrix M and computing the trace we obtain:

$$\begin{aligned}
Tr(\chi^\dagger\Sigma) &= \frac{2\sqrt{3}}{3}(m_u - m_d)\eta_8\pi^+\pi^-\pi^0 - (m_s - m_u)\frac{\eta_8\pi^0K^+K^-}{\sqrt{3}} + \\
&\quad + \frac{\sqrt{3}}{3}(m_s - m_d)\pi^0\eta_8K^0\bar{K}^0
\end{aligned}$$

The term $\eta_8\pi^+\pi^-\pi^0$ gives rise to the diagram shown in fig. (1.5) while the other two terms simply add a contribution to the vertex factor of diagrams shown in fig.1.4. To build the $\eta \to \pi^0\gamma\gamma$ diagram we must use the diagrams shown in fig. (1.3), fig. (1.4) and fig. (1.5). The only way is to contract the π^+,π^- and K^+,K^- legs to have the diagrams shown in fig. (1.6). These can be evaluated using the usual Feynman rules for boson propagator and boson legs. They are finite. This happens because also in $\mathscr{L}_4$ Lagrangian cannot be a direct 2-photon coupling of the type of fig. (1.2) for the same reason illustrated before for $\mathscr{L}_2$: the photons couple only to charged mesons. So there aren't counterterms that could absorb divergences coming from the loop integral.

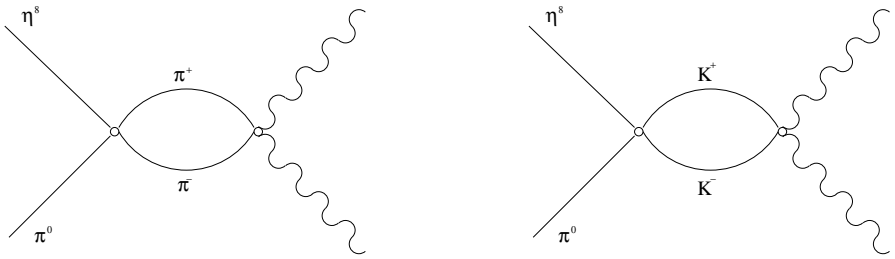

Figure 1.6: Feynman diagrams for $\eta \to \pi^0\gamma\gamma$ amplitude at $O(p^4)$.

Indicating with P, p, q_1, q_2 the η, π^0, and the two photons quadrimomenta respectively, the amplitude for the decay $\eta(P)\pi^0(p)\gamma(q_1)\gamma(q_2)$ is usually written in the form:

$$M = \sum_i (a_i^t + a_i^P)A + \sum_i (b_i^t + b_i^P)B$$

where A and B are the two kinematic allowed amplitudes:

$$\begin{aligned} A &= (\epsilon_1 \cdot \epsilon_2)(q_1 \cdot q_2) - (\epsilon_1 \cdot q_2)(\epsilon_2 \cdot q_1) \\ B &= -(\epsilon_1 \cdot \epsilon_2)(P \cdot q_1)(P \cdot q_2) - (\epsilon_1 \cdot P)(\epsilon_2 \cdot P)(q_1 \cdot q_2) + \\ &\quad +(\epsilon_1 \cdot q_2)(\epsilon_2 \cdot P)(P \cdot q_1) + (\epsilon_1 \cdot P)(\epsilon_2 \cdot q_1)(P \cdot q_2) \end{aligned}$$

where with ϵ_i we indicate the photon elicity.
The coefficient a_i^t and b_i^t refer to the tree-level and counter-term contribution, while a_i^P and b_i^P to the loop contributions. i refers to the order $O(p^i)$. So in our case we have $a_2^t = b_2^t = a_2^P = a_2^P = a_4^t = b_4^t = 0$. The pion and kaon loop diagrams give contribution only to a_4^P. So we have $b_4^{\pi,K} = 0$ [6] and defining $s = (q_1 + q_2)^2 = 2q_1 \cdot q_2$:

$$\begin{aligned} a_4^\pi &= -\frac{2\sqrt{2\alpha}}{3\sqrt{3}\pi F_\pi^2}\Delta m_K^2 \left(1 + \frac{3s - m_\eta^2 - 3m_\pi^2}{m_\eta^2 - m_\pi^2}\right) H(s, m_\pi^2) \\ a_4^K &= -\frac{\sqrt{2\alpha}}{3\sqrt{3}\pi F_\pi^2}\left(3s - m_\eta^2 - \frac{1}{3}m_\pi^2 - \frac{8}{3}m_K^2\right) H(s, m_K^2) \end{aligned}$$

and

$$sH(s, m^2) = s\int_0^1 dz \int_0^{1-z} dy \frac{zy}{m^2 - szy} = -\frac{1}{2} - \frac{1}{2x} ln^2 \frac{\sqrt{x} + \sqrt{x-4}}{-\sqrt{x} + \sqrt{x-4}}$$

with $(x = s/m^2)$.
In these formulas $\Delta m_K^2 = \left(m_{K^0}^2 - m_{K^+}^2\right)_{QCD} = 6.0 \times 10^{-3}$ GeV^2 is the kaon

mass difference after that the electromagnetic self energy has been removed. Evaluating these quantities and integrating over the phase space one finds the contribution to the η width coming from $\eta \to \pi^0\gamma\gamma$ process at $O(p^4)$ in ChPT:

$$\Gamma^{(4)}(\eta \to \pi^0\gamma\gamma) = 7.18 \times 10^{-3} eV$$

As we have seen before the pion loop contribution is suppressed by the G-parity violation in the vertex $\eta\pi^+\pi^-\pi^0$, which makes the amplitude proportional to $m_d - m_u$ or Δm_K^2 while the kaon loop is suppressed by the factor m_K^2 appearing in the kaon propagator.
Also $O(p^6)$ calculation has been performed. At this level the calculation becomes less precise. In fact the $\mathscr{L}_6$ Lagrangian has many terms ~ 100 and it is impossible to evaluate the coefficients from experimental measurements of other branching ratios or physical quantities. To give the ChPT prediction several techniques have been adopted to evaluate the $O(p^6)$ Lagrangian terms. These run from resonance saturation assumption to large N_c limit calculation. In the next section we'll give an overview of the techniques.

1.6 $\eta \to \pi^0\gamma\gamma$ at $O(p^6)$ and beyond.

The first technique used to estimate the $\mathscr{L}_6$ coefficients was based on *the resonance saturation* assumption. It consists to assume that $\mathscr{L}_6$ Lagrangian coefficients are mainly determined by the Vector Meson Dominance (VMD) diagram shown in fig. (1.7). The basic idea of the VMD model is that the coupling of light mesons to photons proceeds via the Vector Mesons, which have the right spin and parity to couple to real photons.

VMD can be used to estimate the $\mathscr{L}_6$ coefficient by taking only the $O(p^6)$ contribution from the Vector Mesons propagators [6]. This assumption is known as "Resonance Saturation" and it works for $\mathscr{L}_4$ Lagrangian. Doing this one obtains the value:

$$\Gamma^{(6)}_{vec.res.} = 0.18 \text{ eV}.$$

If one takes the full VMD propagator one has an all order estimate (at $O(p^6)$ and beyond), giving the result $\Gamma_{VMD} = 0.31$ eV.
Other contributions from $O(p^8)$ have been taken into account, coming from diagrams shown in fig. (1.8) that have the same strength of pion and kaon loops. It happens because in this case there isn't a G-parity violating vertex in the diagram. Due to strong interference among loop diagrams and VMD diagrams, the loop contribution is much higher when considered together with the VMD estimate. This gives a value of $\Gamma \sim 0.42$ eV.

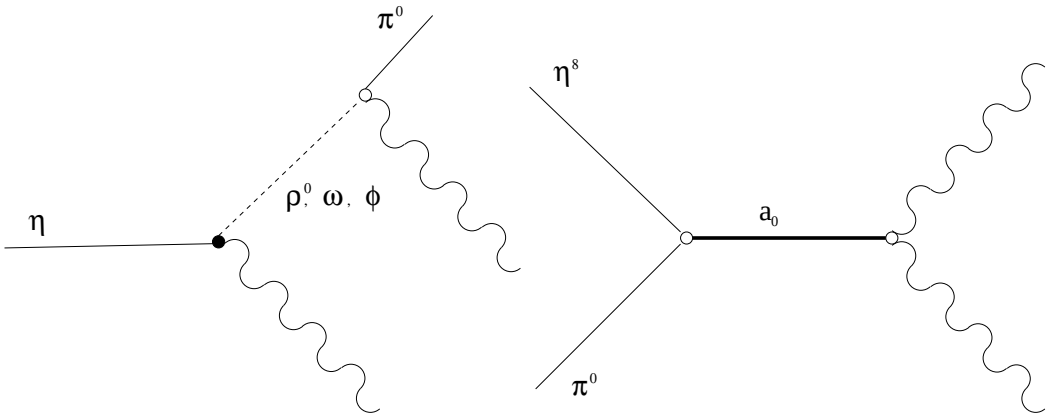

Figure 1.7: VMD and a_0 diagrams for the $\eta \to \pi^0\gamma\gamma$ amplitude.

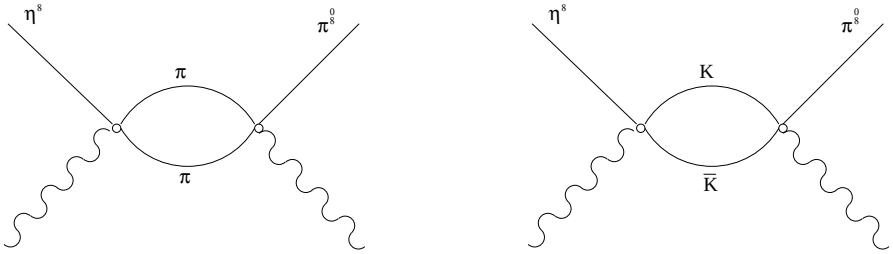

Figure 1.8: Loops at $O(p^8)$ [7].

In ref. [6] also the contribution coming from the scalar meson a_0 and a_2 is taken into account. The a_0 scalar meson decays both in the $\gamma\gamma$ final state and in the $\eta\pi^0$ final state, crossing the $a_0 \to \gamma\gamma$ decay and building a scalar propagator one can construct the diagram shown in fig. (1.7 right) obtaining a $\eta\pi^0\gamma\gamma$ coupling.
The sign of this contribution was unknown and it produces a large error on the decay width:

$$\Gamma \sim 0.42 \pm 0.20 \text{ eV}.$$

Recently a new work has been published that re-evaluates all contributions to the amplitude in Chiral Perturbation Theory using a Chiral Unitary approach [7]. Here we will not describe the Chiral Unitary approach, the interested reader can refer to [7] and reference therein. We underline the main results of this work.
The tree level VMD amplitude has been reevaluated using more recent data in [8] and renormalizing the VMD couplings to the measured branching ratios of vector meson decays. In [6] only $\omega \to \pi^0\gamma$ was adjusted because it was the only available at that time, while SU(3) considerations were done on the other couplings. The estimated VMD tree-level amplitude is:

$$\Gamma_{VMD-tree} = 0.30 \pm 0.06 \text{ eV}$$

The uncertainty linked to the sign of the a_0 resonance is eliminated. The a_0 is generated directly in the $KK \to \pi^0\eta$ amplitude through non perturbative techniques that are able to reproduce the a_0 resonance peak. In this way the size and sign of a_0 resonance is unambiguously determined. At the end its contribution is small (0.01 eV). The strong constructive interference between tree-level VMD and 1-loop diagram is confirmed, rising about of 30% the VMD estimate. Also the $O(p^8)$ term is added and VMD loops are considered. In this way the main systematic uncertainty of [6] is reduced. At the end one obtains the value:

$$\Gamma = 0.47 \pm 0.10 \text{ eV}$$

Here the main systematic error comes from the error on the measurements of vector mesons branching ratios. To illustrate the importance of the several contributions, the $m_{\gamma\gamma}$ spectrum obtained adding each amplitude component is shown in fig. (1.9).

This is what concern the more recent theoretical study on the $\eta \to \pi^0\gamma\gamma$ decay width.
In the literature we find many theoretical calculations. In the framework of ChPT other calculations were done to estimate the $\mathscr{L}_6$ operators coefficients.

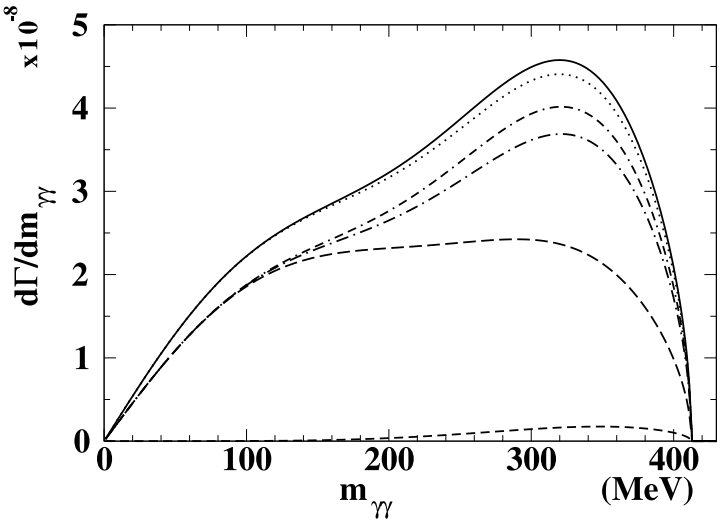

Figure 1.9: From bottom to top, short dashed lines: chiral loops $O(p^4)$; long dashed line: tree level VMD; dashed-dotted line: coherent sum of the previous mechanisms; double dashed-dotted line: VMD loops added; continuous line: $O(p^8)$ loop term added; the dotted line below the continuous one indicates the full calculation without a_0 contribution. [7]

In [9] the $\mathscr{L}_6$ Lagrangian was studied taking into account only terms leading in the large N_C limit. The large N_C limit is an approximation in which the QCD contributions are expanded as a power series of $1/N_C$, where $N_C = 3$ is the number of colors. The leading term in this expansion consists to take $N_C \to +\infty$. This approximation has produced many successful results [10]. Only three operators contributing to the $\eta \to \pi^0\gamma\gamma$ amplitude are leading in the large N_C expansion. The coefficients of these operators are called d_1, d_2, d_3.
The coefficients d_1 and d_2 where estimated in [6] by the resonance saturation assumption. All contributions were estimated in [9] using the so-called Extended Nambu Jona-Lasinio Model. The ENJL model consists in approximating the large-N_C QCD at the chiral symmetry breaking scale Λ_χ (a model parameter) by an effective four-fermion theory. The main assumption is that higher dimension fermion operators are irrelevant for long distance interactions. The decay width prediction of this model is:

$$\Gamma_{ENJL}(\eta \to \pi^0\gamma\gamma) = 0.58 \pm 0.3 \text{ eV}$$

This value is obtained with a prediction for the d_3 coefficient $d_3 = 1.5 \times 10^{-5}$. The d_3 constant has been evaluated in the scalar resonance saturation as-

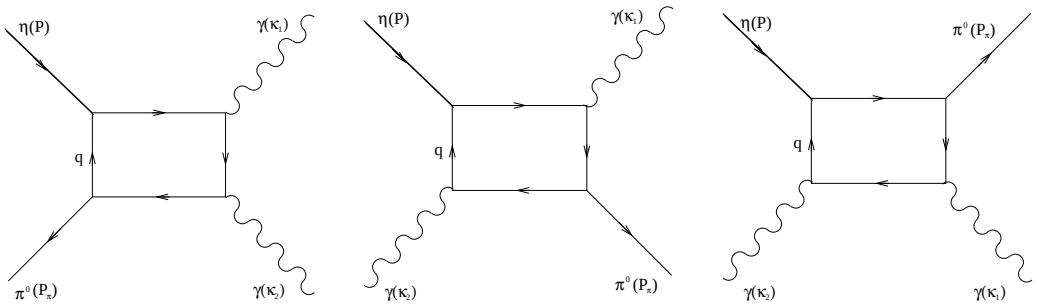

Figure 1.10: The quark-box diagram for the $\eta \to \pi^0\gamma\gamma$ decay.

.

sumption (a_0) by [11] giving the value $d_3 \simeq 0.38 \times 10^{-5}$. In that case the resonance saturation would not be valid for $\mathscr{L}_6$ Lagrangian. This is quite surprising because it does work well in the $O(p^4)$ case [12]. Only the measurement of the decay width with good accuracy could clarify the problem. Another NJL calculation made by reference [17] gives the following result:

$$\Gamma(\eta \to \pi^0\gamma\gamma) = 0.11 \text{ eV}$$

1.7 $\eta \to \pi^0\gamma\gamma$ in the full VMD and in the quark loop model context.

Out of ChPT description of the $\eta \to \pi^0\gamma\gamma$ there were other theoretical estimates of the decay rate. In [13] the tree level VMD calculation was performed according the diagrams shown in fig.(1.7).
The value obtained is:

$$\Gamma_{VMD} = 0.30^{+0.16}_{-0.13} \text{ eV}$$

In [14] a quark-box model is used to evaluate the decay width.
The quark box diagrams are shown in fig. (1.10). The model parameters are the pseudo-scalar meson-quark-quark couplings (ηqq and $\pi^0 qq$) and the constituent quark masses. The quark masses are not the real quark masses, but they are effective quark masses. Reasonable ranges of this masses can be deduced in the study of the decay $P(pseudoscalar) \to \gamma\gamma$, $P \to l\bar{l}$ and $P \to \gamma l\bar{l}$. The assumption $m_u = m_d = m$ is done with $280 < m < 330$ MeV/c^2 and $m_s = 500$ MeV/c^2. The m_s value is roughly fixed being the calculation almost insensitive to this parameter. The $\pi^0 qq$ and ηqq coupling are determined by the decay $\eta \to \gamma\gamma$ and $\pi^0 \to \gamma\gamma$ that proceed through the triangle diagrams shown in fig. (1.11).
From the $P \to \gamma\gamma$ decay width one finds the following couplings of the π^0 and

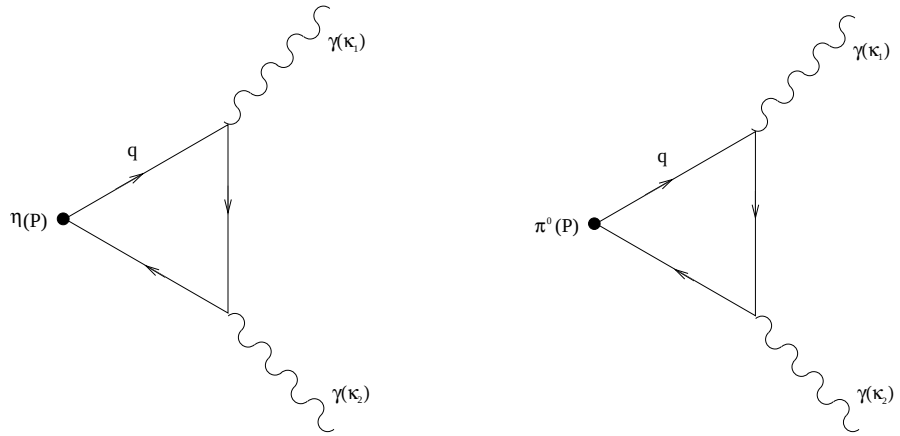

Figure 1.11: Triangle diagrams used to evaluate the ηqq and πqq couplings.

η to quarks: $g_{\pi^0 uu} = g_{\pi^0 dd} = 3.19 \pm 0.11$ and $g_{\eta uu} = g_{\eta dd} = g_{\eta ss} = 1.26 \pm 0.06$. The resulting $\eta \to \pi^0\gamma\gamma$ width is:

$$\Gamma_{Quark-Box} = 0.70 \pm 0.12 \text{ eV}$$

Varying m in the [280,330] MeV interval the width spreads in the range:

$$\Gamma_{Quark-box} = 0.60 - 0.97 \text{ eV}.$$

1.8 Theoretical model predictions summary.

Theoretical estimates of $\eta \to \pi^0\gamma\gamma$ decay width are summarized in table (1.1) where the references are reported.

As we have shown there are many models and frameworks in which the $\eta \to \pi^0\gamma\gamma$ has been computed. This demonstrates the theoretical interest for this decay. The experimental history is very rich too. Many experiments have tried to measure this decay width leaving, still today, large uncertainities in the measurement. For this reason it is impossible to estabilish definitively the physical process that is able to describe the decay.
A summary of the experimental measurements will be given in the next section with a sketch of the experimental history.

1.9 $\eta \to \pi^0\gamma\gamma$ phenomenology.

In fig. (1.1) we show 2 η states. Both of them are not strange and are SU(2) singlet, for this reason they are called with the same name. The only

Model	$\Gamma(\eta \to \pi^0\gamma\gamma)$ (eV)	error range (eV)	reference
VMD	0.30	+0.16, -0.13	[13]
Quark Box	0.70	0.60 - 0.97	[14]
CHPT (res. sat.) p^6	0.18	...	[6]
ChPT (res. sat.)	0.42	$\pm$0.20	[6]
ChPT (ENJL p^6)	0.58	$\pm$0.3	[9]
Unitary ChPT	0.47	$\pm$0.10	[7]
ENJL	0.27	+0.18, -0.07	[15]
NJL	0.92, 0.58	...	[16]
NJL (Belkov) $O(p^6)$	0.11	...	[17]

Table 1.1: Theoretical predictions for $\Gamma(\eta \to \pi^0\gamma\gamma)$.

difference is that one belong to the $SU(3)$ octet (η_8) and the other one is the $SU(3)$ singlet (η_0). If $SU(3)$ were an exact simmetry the η_8 and η_0 state would be two different particles in the physical spectrum.
This doesn't happen because the quark masses are different, $SU(3)$ is broken, and the physical η states are a mixing between η_8 and η_0. So the physical states, η and η' can be written in the form:

$$\begin{pmatrix} \eta \\ \eta' \end{pmatrix} = \begin{pmatrix} cos\theta & -sin\theta \\ sin\theta & cos\theta \end{pmatrix} \cdot \begin{pmatrix} \eta_8 \\ \eta_0 \end{pmatrix}$$

As we have seen before the $U(1)_A$ axial simmetry is broken by the Chyral anomaly, so the η_0, that is associated to the $U(1)_A$, is not a Goldstone boson. For this reason it is not compelled to have a zero mass in the Chyral limit. In fact the two physical η states have a mass of 547.30 MeV (η) and 957.78 MeV (η'). While the η has a mass comparable with the kaon masses, ~ 500 MeV, the η' mass is much higher. This indicates that η is almost η_8 and η' is almost η_0, that is the θ angle is small.
The θ mixing angle has been measured also by the KLOE experiment studying the ratio of branching fractions:

$$\frac{Br(\phi \to \eta'\gamma)}{Br(\phi \to \eta\gamma)}$$

and a value of $\theta = -12.9^{+1.9^\circ}_{-1.6}$ [18] has been extracted.
The η is a pseudoscalar particle symmetric under C conjugation, its main decay modes are reported in tab. (1.2) together with their branching ratio.
To measure rare η decays one must produce a large quantity of η mesons,

Decay channel	Br
$2\ \gamma$	$(39.43 \pm 0.26)\%$
$3\pi^0$	$(32.51 \pm 0.29)\ \%$
$\pi^+\pi^-\pi^0$	$(22.6 \pm 0.5)\ \%$

Table 1.2: Main η decay modes [1].

this has been done in hadron machine through the following reactions:

$$\begin{array}{ll} \pi^- + p \to \eta + n & K^- + p \to \Lambda + \eta \\ \pi^+ + d \to p + p + \eta & \pi^+ + n \to \eta + p \\ \pi^+ + p \to \pi^+ + p + \eta & \pi^- + n \to \pi^- + n + \eta \end{array}$$

The first $\eta \to \pi^0\gamma\gamma$ observation was claimed at CERN in 1966 [19]. In that experiment a fraction of $\eta \to \pi^0\gamma\gamma$ decays of the same order of $\eta \to \gamma\gamma$ and $\eta \to 3\pi^0$ contributions was guessed. Theoretical predictions were much lower so since that time a lot of measurements were performed. Some experiments measured a value, some others gave an upper limit.
In fig. (1.12) the branching ratios measured and the upper limit determined are shown, all the references can be found in ref. [20].

The two last measurements are those of GAMS-2000 experiment [33] and Crystall Ball experiment [34]. The PDG quotes the GAMS-2000 value:

$$Br(\eta \to \pi^0\gamma\gamma) = (7.2 \pm 1.4) \times 10^{-4} \quad \text{GAMS}$$

while the Crystall Ball measurement is:

$$Br(\eta \to \pi^0\gamma\gamma) = (2.7 \pm 0.9_{stat.} \pm 0.5_{syst.}) \times 10^{-4}$$

This means that the first CERN observation and many others were wrong. The GAMS result itself is in doubt now due to the CB new measurement. The GAMS mesurement has triggered many of the theoretical works discussed in this chapter, because ChPT prediction was unable to reproduce that result.
GAMS searched for $\eta \to \pi^0\gamma\gamma$ in an η sample produced through the reaction $\pi^- p \to \eta n$. The produced number of η's was 6×10^5 and ~ 35 $\eta \to \pi^0\gamma\gamma$ events were identified. Despite the small value of collected events, the signal signature is very clear (see fig. 1.13).

The Crystall Ball η sample is produced in the same way, the number of produced η's is much higher 3×10^7, and the number of detected events is 120 ± 40. Despite this, the method used to extract the signal is based on

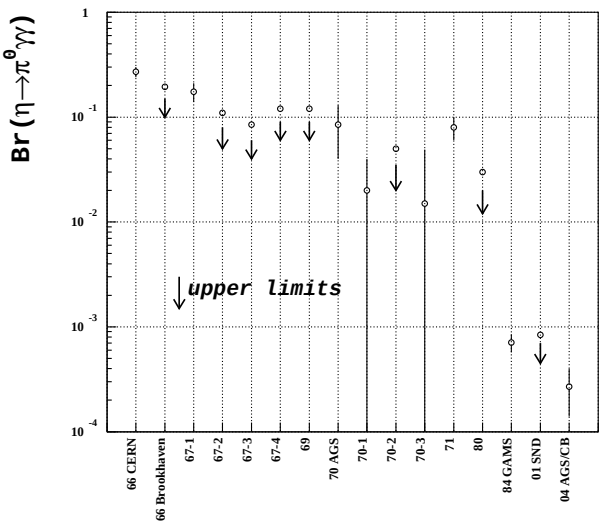

Figure 1.12: Branching ratio measurement in the history. The arrows indicate the upper limits. References:
66 CERN [19], 66 Brookgaven [21], 67-1 [22],67-2 [23], 67-3 [24], 67-4 [25], 69 [26], 70 AGS [27], 70-1 [28], 70-2 [29], 70-3 [30], 71 [31], 80 [32], 84 GAMS [33], 01 SND [20], 04 AGS/CB [34]

an absolute background subtraction based on MC simulation. No particular signal topology is observed.

The very different values measured by GAMS and Crystall Ball give different theoretical indication.
In the GAMS case all ChPT based models give value too small, and only the Quark Box model gives a value in good agreement. The Crystall Ball result lies in a lower range, being consistent with almost all ChPT predictions. For this reason the $\eta \to \pi^0\gamma\gamma$ has been studied at KLOE in this work. In our case the η is produced through the $\phi \to \eta\gamma$ decay, the backgrounds and the systematic are completely different respect to hadron machines.
The SND collaboration [20], that works at a ϕ-factory too, has performed this measurement and given an upper limit: $Br(\eta \to \pi^0\gamma\gamma) < 8.4 \times 10^{-4}$ not reaching the GAMS sensitivity due to low number of η mesons produced.

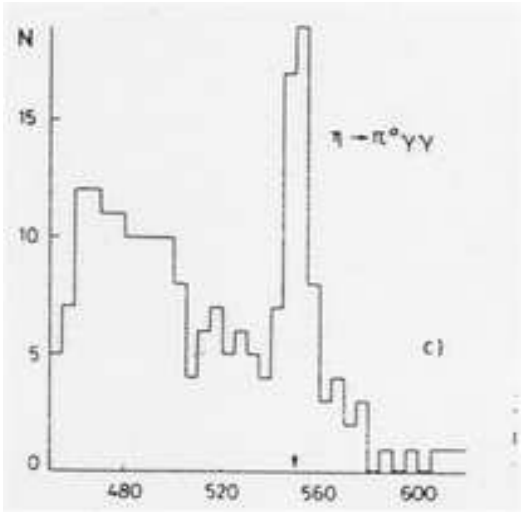

Figure 1.13: $\eta \to \pi^0\gamma\gamma$ signature of the GAMS experiment.

Chapter 2

The KLOE experiment.

In this chapter we describe the KLOE experiment. The KLOE detector, together with the algorithms used to select and analyze the DATA, is shown. Also an overview of the Monte Carlo simulation of the experiment is given. The DAΦNE collider on which KLOE works is also presented.

2.1 The DAΦNE collider.

The KLOE experiment works on the collider DAΦNE at Frascati. DAΦNE (**D**ouble **A**nnular Φ-factory for **N**ice **E**xperiments) is able to produce large quantity of ϕ mesons. This type of machines are commonly known as ϕ factory. The ϕ is generated in e^+e^- collisions and the ϕ decay products are then analyzed by the KLOE detector. A lot of low energy measurements can be performed, in particular ϕ, η and kaons decays can be studied. DAΦNE works at the energy corresponding to the ϕ resonance peak ($M_\phi = 1019.456 \pm$ 0.020 MeV) [1]. The ϕ production cross section at DAΦNE has a peak value of $\sigma_{e^+e^-\to\phi} \sim 3.1\ \mu b$.

The first stage of the DAΦNE collider consists of a LINAC used to accelerate electron and positron up to 510 MeV. They are accelerated at different times and temporary collected in a small accumulator ring (see fig. 2.1).

The injection chain (LINAC plus accumulator) flips from an e^+ condition to an e^- condition. The e^+ and e^- beams are made of bunches, they are injected into two different rings, shifted in the horizontal plane. The double ring configuration is necessary to reduce inter-beam interaction, an effect that limits the luminosity. The two rings intersect in two collision points. At one the KLOE detector is located, while the other is alternatively occupied by two other experiments: DEAR and FINUDA (see fig. 2.2).

The maximum number of bunches that can circulate is 120, correspond-

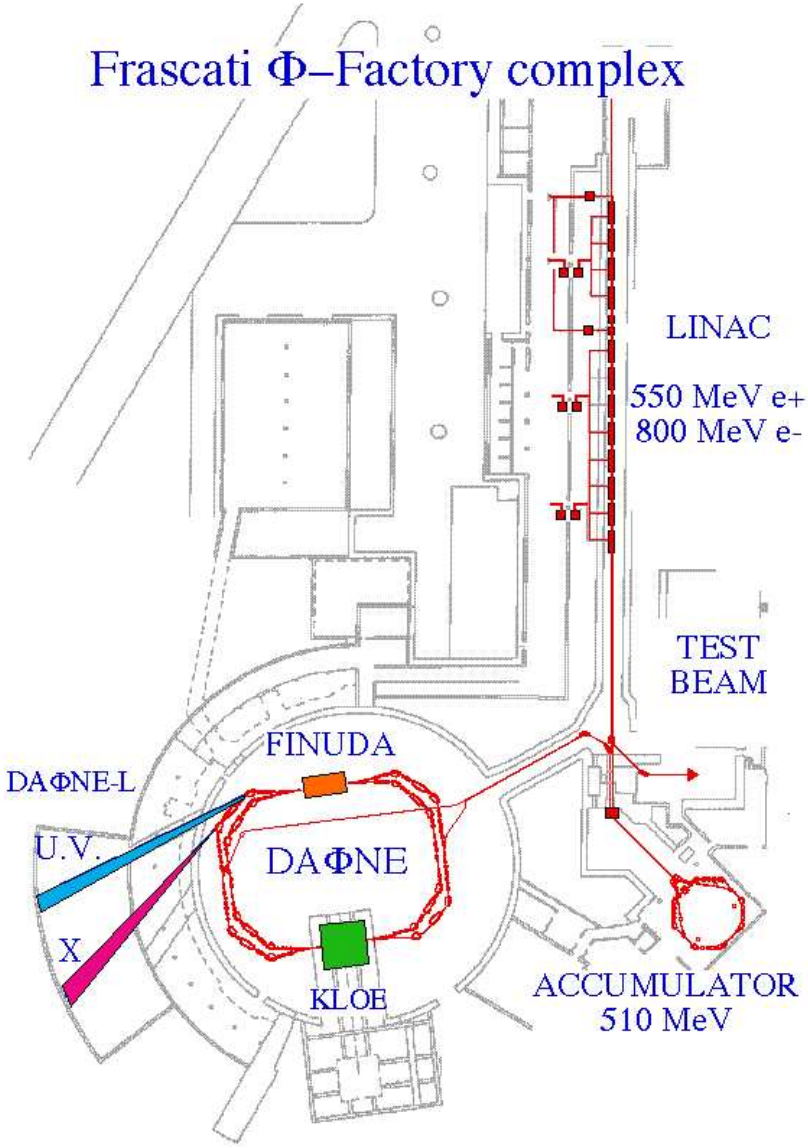

Figure 2.1: Scheme of the DAΦNE collider apparatus.

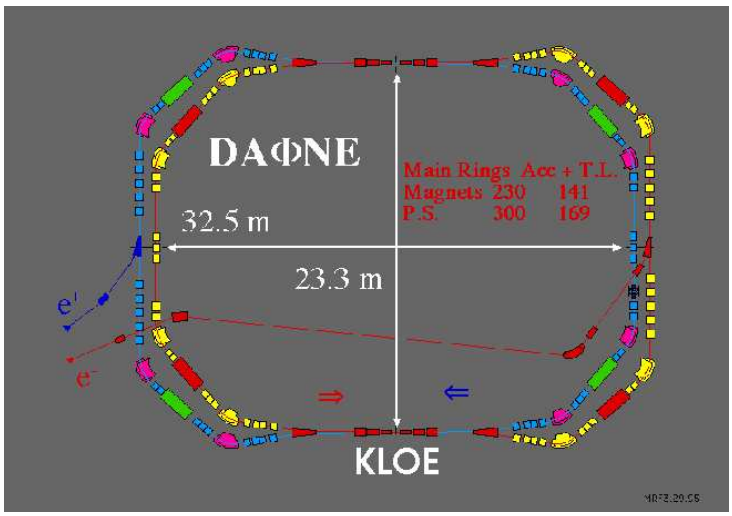

Figure 2.2: Double ring collider scheme. The two interaction regions are shown.

ing to a bunch crossing period of 2.7 ns. During 2001-2002 data taking the average bunch number was ~ 60. The beams collides at the KLOE interaction point (IP in the following) with a crossing angle $\theta_x \simeq 25\ mrad$, then the ϕ is produced with a momentum of about 13 MeV in the horizontal plane.

In order to have high circulating currents the injection is very frequent as can be seen in fig. (2.3), where the beam currents together with the luminosity as a function of time are reported. High currents are needed to reach high luminosity that is the characteristic feature of DAΦNE.
The design peak luminosity is 5×10^{32} cm^{-2}s^{-1} while the peak luminosity reached in 2001-2002 data taking was $\sim 8 \times 10^{31} cm^{-2} s^{-1}$. At the moment DAΦNE is still running and in 2004 data taking has reached $\sim 1.1 \times 10^{32}$ cm^{2}s^{-1}. The total integrated luminosity is ~ 450 pb^{-1} in 2001-2002 data taking, while in 2004 KLOE has collected ~ 750 pb^{-1}.

2.2 The KLOE detector.

The KLOE detector consists of three main elements: an electromagnetic calorimeter, a drift chamber and a superconducting solenoid, a schematic transverse section of the detector is shown in fig. (2.4). In the following we will use the following coordinate system: the horizontal direction along the beam pipe is z, the vertical coordinate is y and the horizontal direction

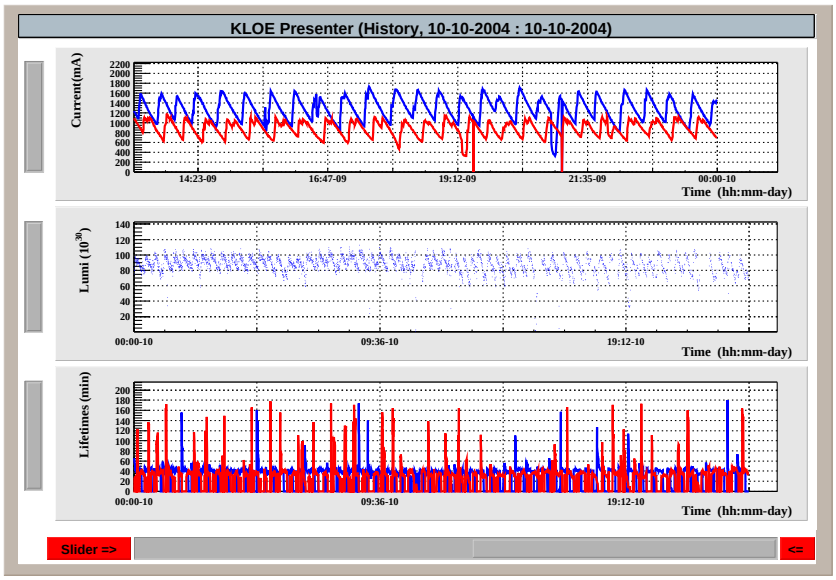

Figure 2.3: Electron (blue) and positron (red) currents in the DAΦNE machine, luminosity and beam life time (2004 data taking).

orthogonal to the beam pipe is x.

2.2.1 The drift chamber

The Drift Chamber (DC) (see fig. 2.5) surrounds the beam pipe which is a sphere made of a beryllium-aluminum alloy with 10 cm diameter and 50 μm thickness.
The beryllium, having a low atomic number, has been used to minimize the interaction of particles produced at the IP with the material.
These elements are inserted inside a superconducting coil which produces a solenoids magnetic field parallel to the beam axis. The field intensity is 0.52 T.
The drift chamber has the following properties:

- high and uniform reconstruction efficiency over a large volume, in order to reconstruct correctly particles that decay inside its sensitive volume (such as K_L);

- track resolution in the transverse plane $\sigma_{R\phi} \simeq 200\ \mu m$ and vertex resolution $\sigma_{vtx} \simeq 1\ mm$;

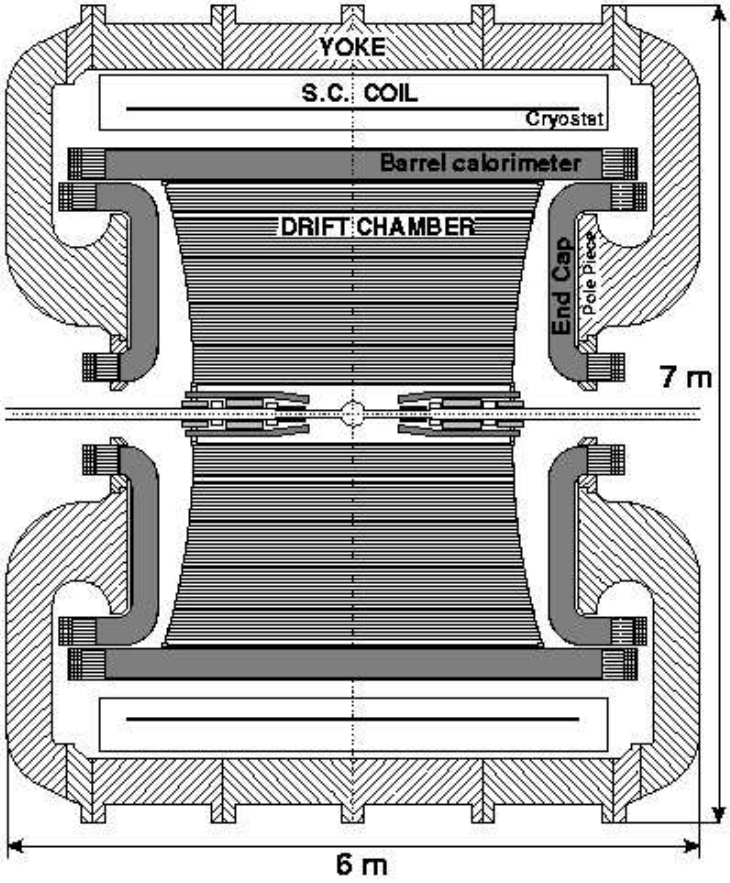

Figure 2.4: Vertical transverse section of the KLOE detector.

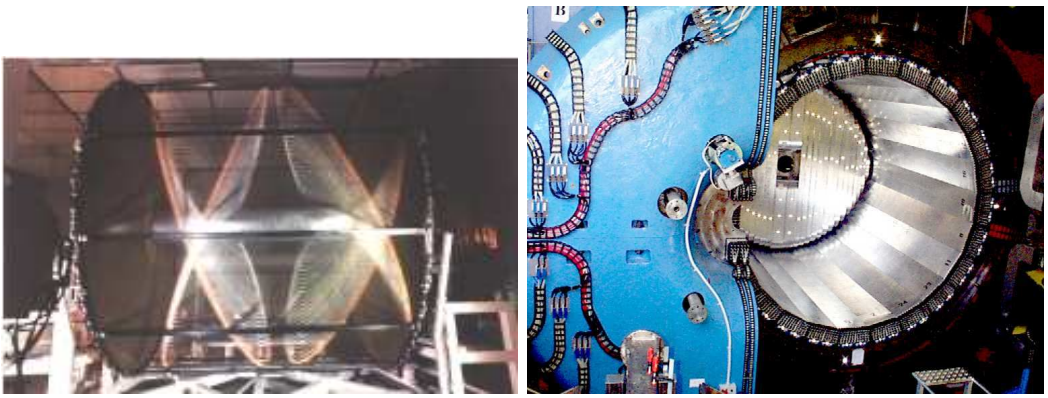

Figure 2.5: Photos of the drift chamber (left) and of the calorimeter (right).

- very good momentum resolution ($\Delta p_\perp / p_\perp$) for low momentum tracks ($50 < p < 300\ MeV$). In this energy range the dominant contribution to the momentum resolution is the multiple scattering:

$$\frac{\Delta p_\perp}{p_\perp} = \frac{0.053}{L|B|\beta}\sqrt{\frac{L}{X_0}}$$

  where $p_\perp$ is the transverse momentum in GeV, β is the velocity of the particle, L is the track length in m, B is the magnetic field in T and X_0 is the radiation length;

- it is transparent to low energy photons (down to 20 MeV).

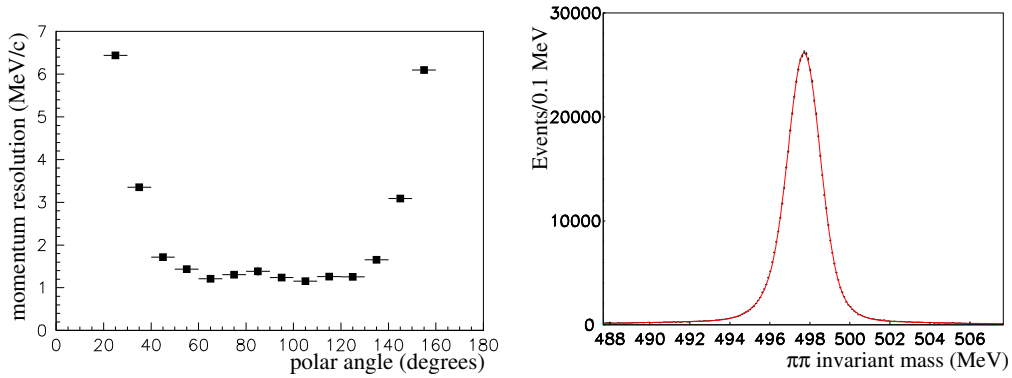

Figure 2.6: (left) Momentum resolution for 510 MeV $e^\pm$ from Bhabha scattering events as function of the polar angle; (right) K_S invariant mass distribution as calculated from oppositely charged tracks from the interaction point.

The chamber has a uniform cell structure on a large cylindrical volume, whose length is variable from 2.8 m near the beam-pipe to 3.3 m near the calorimeter walls; the outer radius is 2 m, the inner radius is 25 cm.

The uniform filling of the chamber has been achieved through a structure of drift cells "almost" square shaped, arranged in coaxial layers with alternating stereo angles which increase with the radius from $\pm$ 60 to $\pm$ 150 $mrad$. The stereo angle is defined as the angle between the wire and a line parallel to the z-axis.
The ratio of field to sense wires is 3:1. The sense wires are made of gold-plated tungsten and their diameter is 25 μm. The field wires are made of silver-plated aluminum and their diameter is 80 μm. There are 12 inner and

46 outer layers, the corresponding cell areas are 2×2 and 3×3 cm^2, respectively, for a total of 12582 drift cells.
The voltage difference is 1750 V and 1900 V for the small and large drift cells respectively.

Materials are chosen in order to minimize the density along the path of particles. A carbon fiber composite ($\leq 0.1X_0$) is used for the chamber walls. The gas used is a 90% helium, 10% isobutane mixture. To reduce multiple scattering and photon conversion the gas mixture has a radiation length $X_0 \simeq 1300$ m. Taking into account also the wires, the average radiation length in the chamber volume is about $X_0 \sim 900$ m.

The momentum resolution for 510 MeV $e^{\pm}$ Bhabha-scattering events is shown in fig. (2.6) for $50° < \theta < 130°$. It is $\sigma_p \simeq 1.3\ MeV$, $\sigma_p/p = 2.5 \times 10^{-3}$. The $\pi^+\pi^-$ invariant mass distribution of $K_S \rightarrow \pi^+\pi^-$ is also shown in the figure. The resolution is $\delta m/m = 1.8 \times 10^{-3}$.

2.2.2 The calorimeter.

The calorimeter has a cylindrical structure surrounding the DC. The cylinder axis is on the horizontal plane parallel to the beam direction.
The calorimeter has the following properties:

- a very good time resolution ($\simeq 100\ ps$) and a good determination ($\simeq 1.4\ cm$) of the photon conversion point, this task is very important to select events that are produced at the IP from the kaons decays that happen in the DC volume. The good position resolution together with the large radius ($\sim$ 2m) consent to have a very good resolution on the angle of the photon conversion point . This is a very important property that is used through kinematic fit techniques (see chapter 3) to reject missing momentum events;

- an high hermeticity (98% of the solid angle), thanks to which multiphoton process has an acceptable geometrical efficiency and events with different number of photons can be separated correctly. The energy resolution is good ($5.7\%/\sqrt{E[GeV]}$) and the calorimeter is fully efficient over the range $20 \div 500\ MeV$;

- it has also a very fast time response, that is used to trigger events at the first stage.

The calorimeter has a led-scintillating fiber sampling structure. Scintillating fibers provide good light transmission over the required distances, up to $\sim 4.3\ m$.

It is made of three main elements: a cylindrical barrel and two end-caps. The barrel consists of 24 modules 4.3 m long $\times$ 23 cm thick with trapezoidal transverse section, with bases of 52 and 59 cm. Each end-cap consists of 32 vertical modules $0.7 \div 3.9$ m long and 23 cm thick. The barrel covers a region between 45° and 135°, the end-caps cover the angles included between 10° and 45° and between 135° and 170° respectively. The transverse section of the modules is rectangular, of variable width. Modules are bent at the upper and lower ends to allow insertion into the barrel calorimeter and also to maintain the photo-tube axes parallel to the magnetic field. Due to the large overlap of barrel and end-caps (see fig. 2.9), the calorimeter has no inactive gap at the interface between those components. The central end-cap modules are vertically divided into two halves.

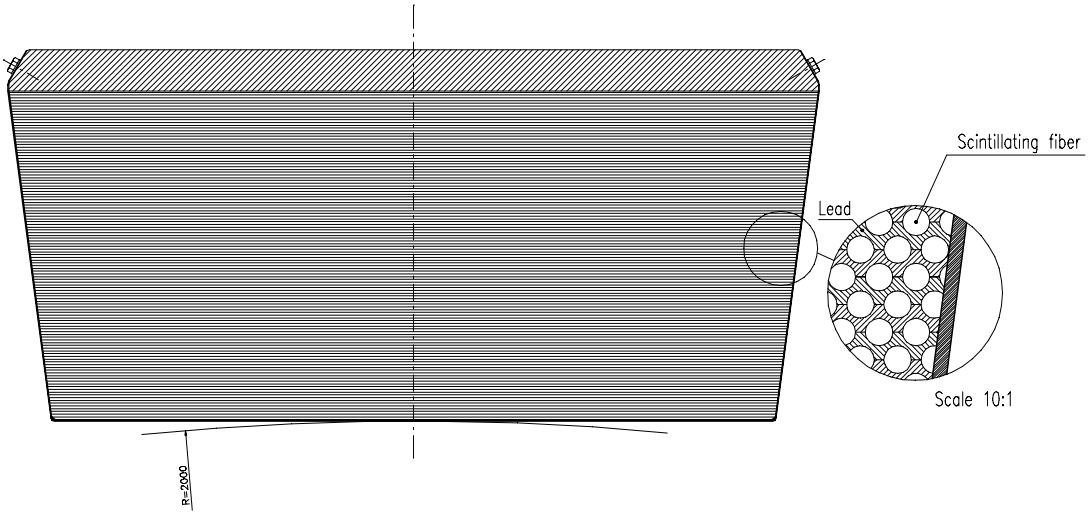

Figure 2.7: Schematic view of the fiber-lead composite of each module of the electromagnetic calorimeter.

All modules are made of 200 grooved, 0.55 mm thick lead foils alternating with 200 layers of scintillating fibers with diameter 1 mm, glued in the grooves with a special epoxy, which is not harmful to the fiber plastic (see fig. 2.7).
Fibers are mostly orthogonal to the entering particles in order to avoid channeling. The ratio by volume of the different component material is: lead:fiber:epoxy 42:48:10. This low value of the lead content consents to have an almost homogeneous calorimeter. In this way the energy loss in the

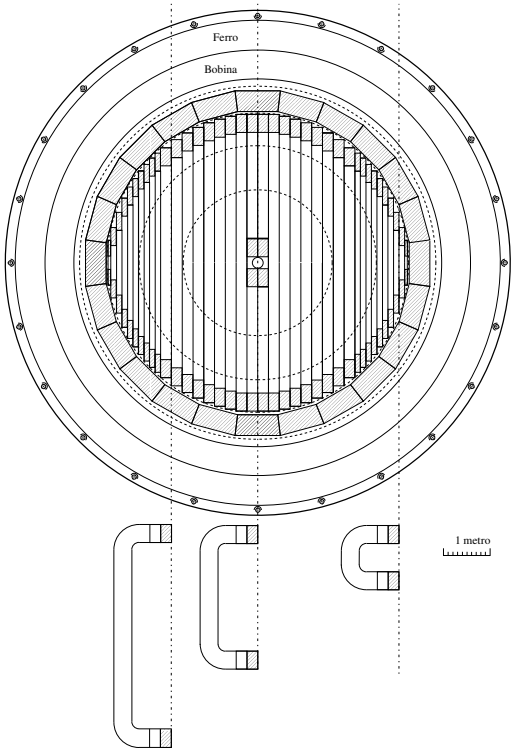

Figure 2.8: Transverse section of the KLOE detector, it is possible to see the shapes of the end-cap EMC modules.

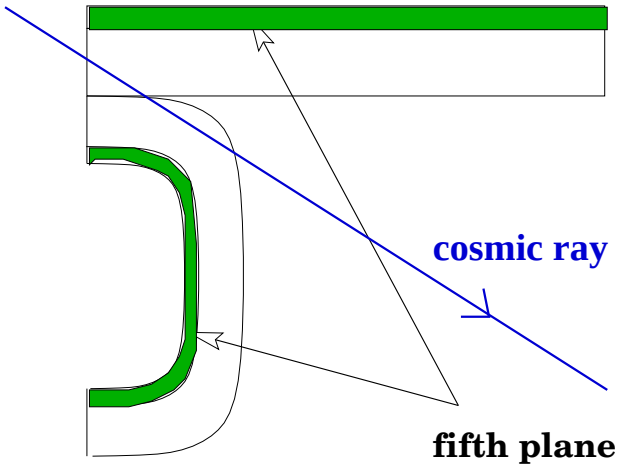

Figure 2.9: Schematic view of the overlap region between barrel and end-cap.

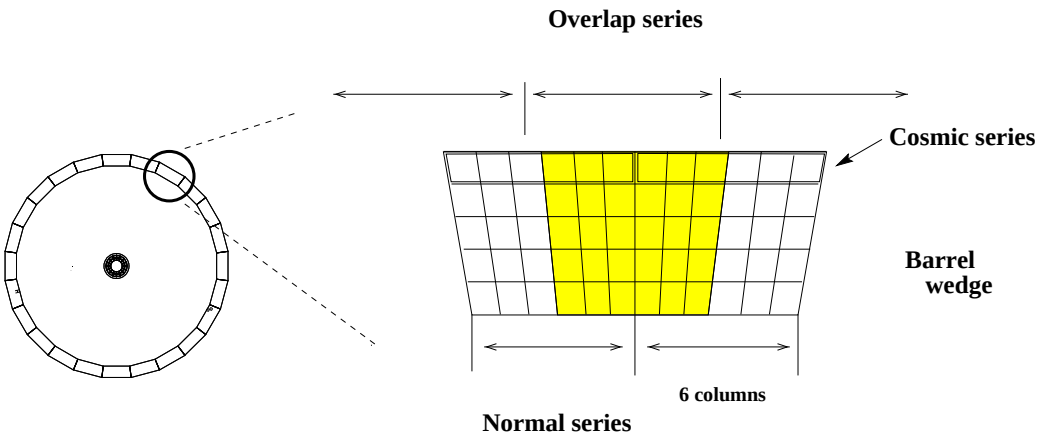

Figure 2.10: Schematic view of a module transverse section.

passive material is almost independent from the shower direction and the energy response is direction independent.
The attenuation length of the fibers is $\lambda \geq 3\ m$, while the average density is 5 g/cm^3, the radiation length is $\sim$ 1.5 cm and the overall thickness of the calorimeter is $\sim$ 15 radiation lengths.
Light is collected on both sides of each module. The longitudinal coordinates is measured by the time difference.
The calorimeter is divided into five planes in depth, four of 4.4 cm, the last is 5.2 cm deep (see fig. 2.10).
In the transverse direction each plane is subdivided into cells 4.4 cm wide. The set made of 5 cells lined up, one for each transverse plane is named "column".
The read-out $r-\phi$ for barrel ($x-z$ for end-cap) granularity for the EmC is finally $\sim 4.4 \times 4.4$ cm^2 slightly varying in size across the modules. This allow a good spatial resolution.

The energy deposit in each cell is obtained from the charge measured at each side of the modules by the ADC's. The cell time is derived by time intervals measured at each side of the modules by the TDC's.
The energy resolution and the linearity of the energy response have been measured using photons from radiative Bhabha events and from $\phi \to \pi^+\pi^-\pi^0$ events. In both cases the photon energy E_γ is estimated by tracks momenta reconstructed by the drift chamber and it is compared with the measured energy E_{CL}. The fractional resolution σ_E/E_γ and the relative deviation from linearity $(E_\gamma - E_{CL})/E_\gamma$, obtained from radiative Bhabha events are plotted in fig. (2.11) as function of the photon energy. Linearity is better than 1% for

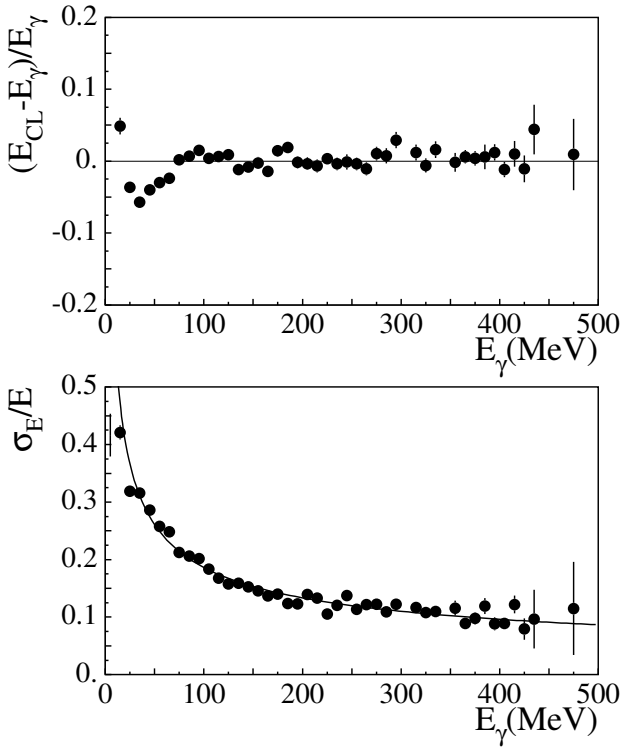

Figure 2.11: (top) Linearity of the calorimeter energy response as a function of the photon energy; (bottom) energy resolution of the calorimeter as a function of the photon energy. The two curves are evaluated with radiative Bhabha events.

$E_\gamma > 75\ MeV$, while deviations from linearity at the $4-5\%$ level are observed for low energies, probably due to the loss of shower fragments. The fit of the energy resolution to the function $a/\sqrt{E[GeV]} + b$ gives a negligible constant term, proving that the resolution is dominated by sampling fluctuations, and gives a stochastic term $a = 5.7\%$. Compatible results are obtained from $\phi \to \pi^+\pi^-\pi^0$.
The time resolution derived by the analysis of various radiative ϕ decays is shown in fig. (2.12). Good agreement between the measurements for different channels is observed down to 100 MeV. The curve in the plot is the result of a fit:

$$\sigma_t = \frac{54\ ps}{\sqrt{E[GeV]}} \oplus 140ps \tag{2.1}$$

the first term is due to the sampling fluctuation and the second term is a constant to be added in quadrature. The constant term is given by the

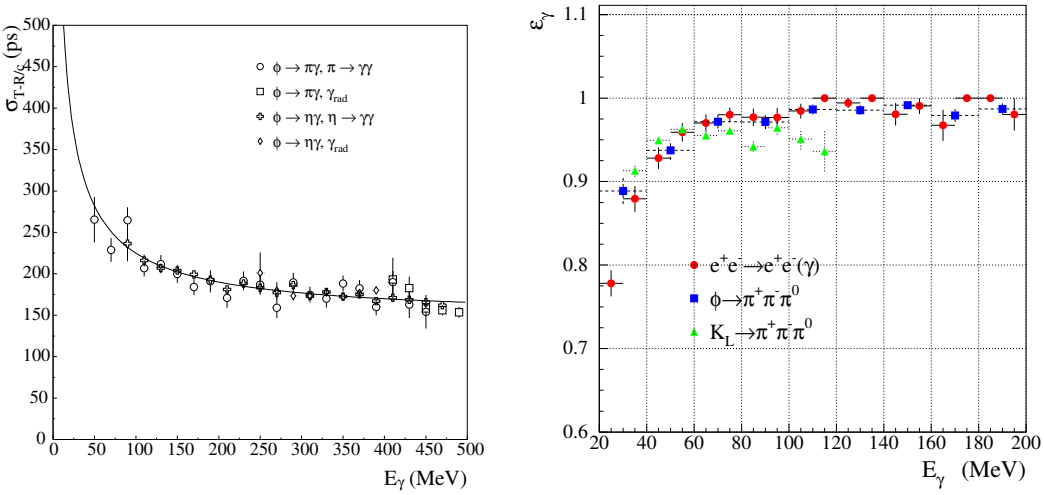

Figure 2.12: (left) Time resolution of the calorimeter as a function of the photon energy, for radiative ϕ decays; (right) Photon detection efficiency as a function of the photon energy, as measured from radiative Bhabha, $\phi \to \pi^+\pi^-\pi^0$ and $K_L \to \pi^+\pi^-\pi^0$ samples.

quadrature sum of two contributions: residual calorimeter miscalibrations, which contribute for $\sim 50\ ps$, and the intrinsic time spread due to the finite lenght of the luminous point in the beam direction, which contributes for $\sim 125\ ps$. Compatible results are obtained from $\phi \to \pi^+\pi^-\pi^0$ and from radiative Bhabha decays.
The position of a cluster centroid in the transverse plane (see fig. 2.10) is determined from the geometrical distribution of fired cells and is $\sigma_t \sim 1.4cm$ while the longitudinal coordinate is determined with the difference of the signal arrival times at both ends. It is:

$$\sigma_z \sim \frac{1.4\text{cm}}{\sqrt{E[GeV]}}$$

The photon detection efficiency is an important quantity for this work. It was estimated using three data samples: radiative Bhabha events and $\phi \to \pi^+\pi^-\pi^0$ decays, which provide photons originated in the interaction point, and $K_L \to \pi^+\pi^-\pi^0$ decays, in which the photons originate from a K_L decay vertex in the DC volume. The detection efficiency ϵ_γ, resulting from these three analyses, are shown as a function of the photon energy in fig. (2.12 right). A constant value of $\sim 99\%$ is observed above 100 MeV, while a loss in efficiency is evident below 100 MeV.

2.2.3 The trigger system

The main function of the trigger system is to:

- produce an unbiased trigger signal for all ϕ events;
- recognize cosmic-ray events and accept a downscaled sample for calibration purposes.

Cosmic rays are recognized by the coincidence of two outer calorimeter planes (cosmic trigger veto).
During years 2000-2001, with an average luminosity of $\sim 10^{31}\ cm^{-2}s^{-1}$, the average trigger rate was about 2.5 KHz. Of those only $\sim$ 250 Hz were due to ϕ events and Bhabha. About 400 Hz were due to downscaled cosmic rays, while an additional $\sim$ 650 Hz were due to cosmic rays escaping the trigger veto. The remaining $\sim 1.2\ KHz$ come from machine background.

There are two main sources of background. One is the Bhabha events at small angles, where electrons and positrons hit two focusing quadrupoles located very close to the IP and produce showers inside the detector. The other source is due to particle losses from the beams. These off-momentum particles are originated in beam-gas interactions or Touschek scattering.

The trigger is based on local energy deposit in calorimeter and multiplicity information from the drift chamber. It is composed by two levels (see fig. 2.13) in order to both produce an early trigger with good timing to start the Front End Electronic (FEE) and to use as much information as possible from the drift chamber. After the arrival of a first level trigger, additional information is collected from the drift chamber, which is used, together with the calorimetric information, to confirm the former and to start the DAQ system.

The "first level" trigger algorithm accepts events if one of these two conditions are found true (see figure 2.13):

- 2 calorimeter clusters with energy larger than a fixed threshold (Low Energy Threshold, LET) with Barrel-Barrel, Barrel-Endcap or Endcap-Endcap topology. The thresholds are: 50 MeV for barrel and variable from 90 - 140 MeV for end-caps. The values are higher for endcap elements closer to the beam pipe;
- 15 drift chamber hits within 250 ns.

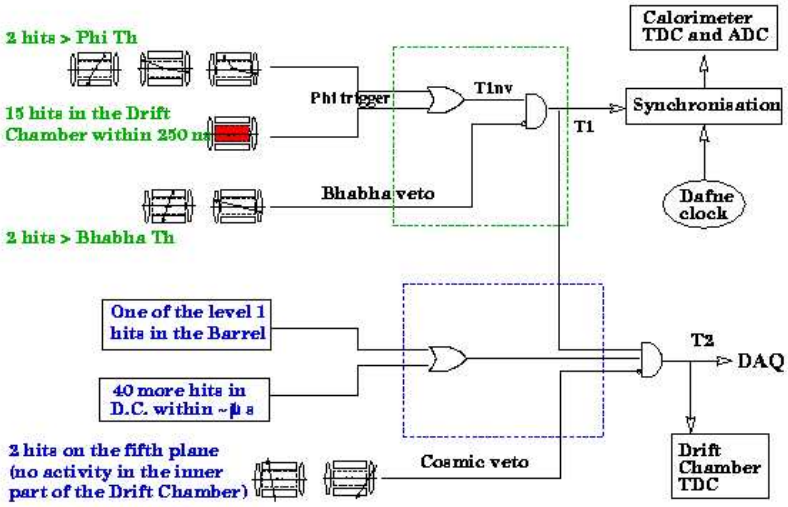

Figure 2.13: KLOE trigger logic, the Bhabha veto has been built but never used in 2001-2002 data taking. This because the luminosity was lower than the design luminosity and the DAQ system was able to acquire all the Bhabha events, the Bhabha are rejected at reconstruction level.

The trigger sets a 2 μs long acknowledge signal, which vetoes other first level triggers and allows signal formation from the drift chamber cells.
Before being distributed to the calorimeter FEE, it is synchronized with a resolution of 50 ps with the DAΦNE radiofrequency divided by 4 ($T = 10.8\ ns$) (see sec. 2.4). Therefore the calorimeter TDC's measure the time with respect to a bunch crossing coming n periods after the collision that originated the event, where n has to be determined by the offline reconstruction of the event. This tecnique allows us to preserve the resolution on time measurementat at the level of ps, which would be otherwise spoiled by the intrinsic jitter of the trigger signal formation.
After the first level decision, a second level trigger is requested to confirm level 1 decision according the following criteria:

- ϕ trigger one of the following criteria:
  - at least a calorimeter hit in the barrel or 3 hits in the same endcap;
  - 40 DC hits integrated during 850 ns after T1;

- Cosmic veto, the following condition is not fullfilled:
  - 2 hits on the external plane of the calorimeter with B-B, B-E topology, no activity in the central region of the DC (this to avoid that high energy particles from the IP could fire the external calorimeter plane and identified as cosmic rays).

At the end of the dead time the trigger system asks for a confirmation from the second level.

The level two trigger T2 gives the stop to chamber TDCs and starts the acquisition of the event.

2.3 Reconstruction algorithms for the calorimeter.

The calorimeter is segmented into 2440 cells, which are read out by Photomultipliers at either end (referred to as sides **A** and **B** in the following). Both charges $Q^{A,B}_{ADC}$ and times $t^{A,B}_{TDC}$ are recorded. For each cell, the particle arrival time t and the impact point along the fiber direction are reconstructed using the times at the two ends as

$$\begin{array}{rcl} t & = & \frac{1}{2}(t^A + t^B - t^A_0 - t^B_0) - \frac{L}{2v} \\ s & = & \frac{v}{2}(t^A - t^B - t^A_0 + t^B_0) \end{array} \tag{2.2}$$

with $t^{A,B} = c^{A,B} t^{A,B}_{TDC}$, where $c^{A,B}$ are the TDC calibration constants, $t^{A,B}_0$ are the overall time offsets, and L and v are the cell length and the light velocity in the fibers. The impact position in the transverse direction is provided by the location of the readout elements. The energy signal E_i on either side of cell i is determined as

$$E^{A,B}_i = k_E g^{A,B}_i(s) \frac{S^{A,B}_i}{S^{A,B}_{mip,i}}$$

where $S = Q_{ADC} - Q_{0,ADC}$ is the charge collected after subtraction of the zero-offsets, and S_{mip} is the response to a minimum-ionizing particle crossing the calorimeter center.The correction factor $g(s)$ accounts for light attenuation as a function of the impact position s along the fiber, while k_E is the overall energy scale factor. The final value of E_i for the cell is taken as the mean of the determinations at both end.

$$E_i(\mathrm{MeV}) = \frac{E^A_i + E^B_i}{2}$$

The calibration constants related to minimum-ionizing particles, S_{mip} and g, are acquired with a dedicated trigger before the start of each long data-taking period. The time offsets $t_0^{A,B}$ and the light velocity v in the fibers are evaluated every few days using high-momentum cosmic rays selected using drift-chamber information. In this iterative procedure, the tracks reconstructed in the drift chamber are extrapolated through the calorimeter, and the residuals between the expected and measured times for each cell are minimized. Finally, a procedure to determine the value of k_E and to refine the values of $t^0_{A,B}$ runs online [35]; it uses Bhabha and $e^+e^- \to \gamma\gamma$ events to establish a new set of constants every $\sim 100 - 200$ nb$^-$1 (approximately every hour during 2002 data taking).

Calorimeter reconstruction starts by applying the calibration constants to convert the measured quantities Q_{ADC} and Q_{TDC} to the physical quantities S and t. Position reconstruction and energy/time corrections vs. s are then performed for each fired cell. Next, a clustering algorithm searches for groups of cells.
In the first step, cells contiguous in $r\phi$ (on barrel) or xz (on the endcap) are grouped into pre-clusters. In the second step, the longitudinal coordinates and arrival times of the pre-clusters are used for further merging and/or splitting. The cluster energy, E_{cl}, is the sum of the energies for all cells assigned to a cluster. The cluster position, $(x, y, z)_{cl}$ and time, t_{cl}, are computed as energy-weighted averages over the contributing cells. Cells are included in the cluster search only if times and energy are available on both sides; otherwise, they are listed as "incomplete" cells. The available information from most of the incomplete cells is added to the existing clusters at a later stage by comparison of the (x, y) positions, (x,z) on the end-cap[1], of such cells with the cluster centroids.

The production of fragments from electromagnetic showers has been studied by comparing data and Monte Carlo samples of $e^+e^- \to \gamma\gamma$ events, with tight selection cuts applied to the two highest-energy clusters in the event (the "golden photons").
The distribution of the minimum distance between the centroids of a golden photon with any other cluster:

$$\Delta x = \sqrt{(x_{cl}^{glod} - x_{cl}^{i})^2 + (y_{cl}^{gold} - y_{cl}^{2})^2 + (z_{cl}^{gold} - z_{cl}^{i})^2}$$

is characterized by reasonable agreement between data and MC at large values of Δx; at low values an appreciable discrepancy is observed. In this latter

[1]It is because the coordinate along the fibers is z for the barrel and y for the end-caps.

case, a similar discrepancy is observed for the distribution of the difference in time, Δt, between the selected clusters.
This discrepancy is due to the bad simulation of fragments in the MC. The multiplicity of fragments in data exceeds that in MC events by about a factor of two and is dominated by clusters with energy below 50 MeV. We attribute these discrepancies to small inaccuracies in the descriptions of the shower development and time response in the Monte Carlo, so that the longitudinal cluster-breaking procedure performs differently for data and MC events. For this reason, depending upon the multiplicity of photons in the event, a split-cluster recovery procedure is applied at the analysis level to merge close clusters depending on their values of Δx , Δt , and energy.

2.4 Determination of the absolute time scale and event-start time

The bunch-crossing period is $T = 2.715$ ns. Due to the large spread of the particle arrival times, the trigger time does not identify the bunch crossing that produced an event; the time at which this bunch crossing occurred must therefore be determined offline. In order not to spoil the EmC time resolution, the start to the TDC system is obtained by synchronizing the level-1 trigger with a clock that is phase-locked to the DAΦNE radiofrequency signal. The clock period is 4 $T_{RF} = 10.85$ ns. The calorimeter times are measured in common-start mode and are given by the TDC stops from the discriminated PMT signals:

$$t_{cl} = t_{TOF} + \delta_c - N_{BC} t_{RF}$$

where t_{TOF} is the time of flight of the particle from the event origin to the calorimeter, δ_c is the sum of all offsets due to electronics and cable delays, and $N_{BC} t_{RF}$ is the time needed to generate the TDC start (see fig. 2.14). The quantities δ_c and t_{RF} are determined using $e^+e^- \to \gamma\gamma$ events. For such events, the distribution of $\Delta_{TOF} = t_{cl} - r_{cl}/c$ shows well-separated peaks corre- sponding to the different values of N_{BC} for events in the sample (see fig. 2.15). We define δ_c as the position of the largest peak in the distribution, and obtain t_{RF} from the distance between peaks. This is done by calculating the discrete Fourier transform of the Δ_{TOF} distribution and fitting the peak around $\nu = 1/t_{RF}$. The absolute TDC time scale is obtained by imposing $t_{RF}(\text{fit}) = t_{RF}$. Both δ_c and t_{RF} are determined with precision better than 4 ps for every 200 nb^{-1} accumulated.

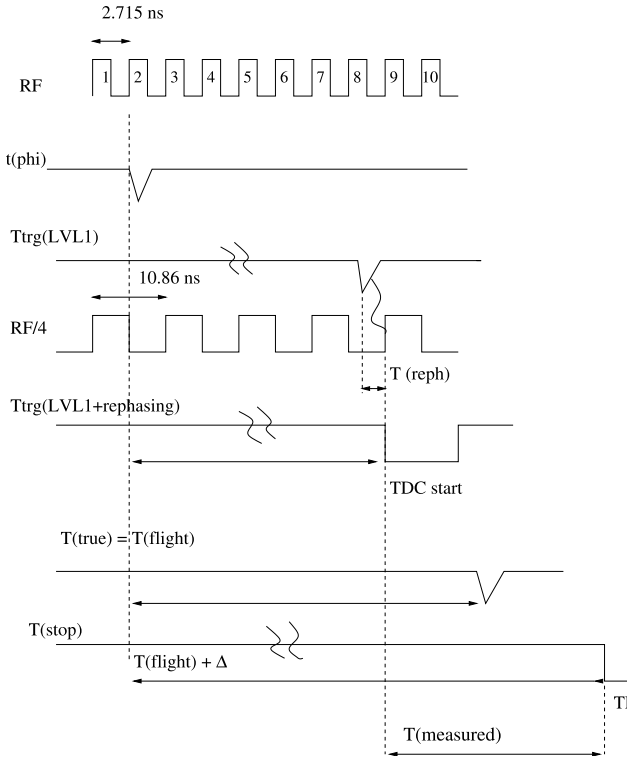

Figure 2.14: Timing scheme for bunch-crossing signal, calorimeter signals, and level-1 trigger formation.

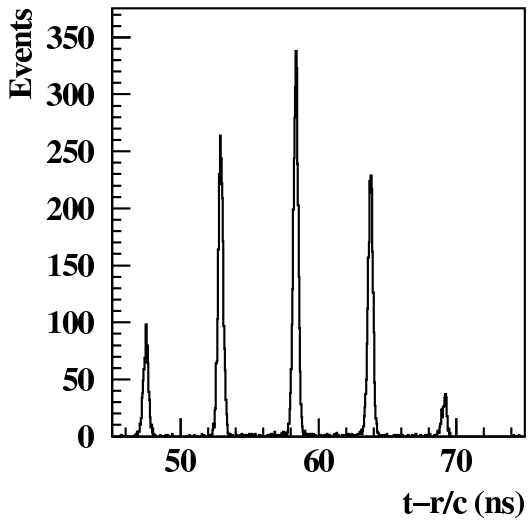

Figure 2.15: Calibration of EmC time scale using $e^+e^- \to \gamma\gamma$ events, Δ_{TOF} distribution.

Since we want the cluster times to correspond to particle times of flight, a time offset $t_{0,evt} \equiv \delta_c - N_{BC} t_{RF}$ must be subtracted from all cluster times (see eq. 2.3). The trigger-formation time $N_{BC} t_{RF}$ varies on an event-by-event basis; it is determined offline at different points of the reconstruction path. A zeroth-order value for N_{BC} (and hence $t_{0,evt}$) is obtained by assuming that the earliest cluster in the event is due to a prompt photon from the interaction point. By imposing $t_{TOF} = r_{cl}/c$ for this cluster, we obtain

$$t_{0,evt} = \delta_c - N_{int} \left[\frac{r_{cl}/c - t_{cl} + \delta_c}{t_{RF}} \right] t_{RF} \tag{2.3}$$

where N_{int} stands for the nearest integer to the quantity in brackets. We refer to $t_{0,evt}$ as the event-start time.

Soft clusters due to the accidental coincidence of machine-background events with the e^+e^- collisions can arrive earlier than the fastest cluster from the collision event itself. To increase the reliability of the estimate of $t_{0,evt}$, the cluster used for its evaluation must also satisfy the conditions $E_{cl} > 50$ MeV and $R_{xy} = (x_{cl}^2 + y_{cl}^2)^{1/2} > 60$ cm.

The $t_{0,evt}$ evaluated in this way is used only to reconstruct and classify the event by physics channel. However, many physics channels contain no prompt photons in the final state, so this determination of N_{BC}, therefore the corrected cluster times $t_{cl}^{(0)}$, may differ from the actual times of flight by an integer number of bunch crossings ΔN_{BC}. This quantity is evaluted in different ways for several channels. For the neutral radiative decays, that are interesting for this work, the goal in redetermining the event-start time is to correct situations in which N_{BC} is at first incorrectly determined because of the accidental coincidence of beam background clusters. For such events, if the second cluster with $E_{cl} > 50$ MeV and $R_{xy} > 60$ cm arrives more than 4 ns after the first, ΔN_{BC} is calculated using the second cluster.

2.5 Track-to-cluster association.

To identify photons one must reject cases in which a charged particle hits the calorimeter producing a cluster. This case is identified by the track-to-cluster algorithm.
The track-to-cluster association module establishes correspondences between tracks in the drift chamber and clusters in the calorimeter.
The procedure starts by assembling the reconstructed tracks and vertices into decay chains and isolating the tracks at the end of these chains. For

each of these tracks, the measured momentum and the position of the last hit in the drift chamber are used to extrapolate the track to the calorimeter. The extrapolation gives the track length L_{ex} from the last hit in the chamber to the calorimeter surface, and the momentum $\vec{p}_{ex}$ and position $\vec{x}_{ex}$ of the particle at the surface. The resulting impact point is then compared with the positions $\vec{x}_{cl}$ of the reconstructed cluster centroids. A track is associated to a cluster if the distance to the centroid in the plane orthogonal to the direction of incidence of the particle on the calorimeter, $D_{tcl} = |(\vec{x}_{cl} - \vec{x}_{ex}) \wedge \vec{p}_{ex}/|\vec{p}_{ex}|$, is less than 30 cm. For each track, the associated clusters are ordered by ascending D_{tcl} values.

2.6 The background rejection filter FILFO.

The background-rejection algorithm is based on calorimeter clustering and DC hit counting, so that background events can be eliminated before DC reconstruction, which is the most CPU-intensive section of our reconstruction program. The main FILFO features are the downscaling of Bhabha and cosmic events, and machine background rejection.
For the identification of background events, cuts are applied on the number of clusters; the number of DC hits; the total energy in the calorimeter; the average polar angle, position, and depth of the (two) most energetic cluster(s); and the ratio between the number of hits in the innermost DC layers and the total number of DC hits. These cuts have been studied to minimize losses for physics channels. Additionally, a simple cut on anomalously large energy deposits in any calorimeter region is included to reject rare machine background topologies due to sporadic beam-loss events.

2.7 Monte Carlo: physics generators and detector simulation.

The KLOE Monte Carlo program, GEANFI, is based on the GEANT 3.21 library [36, 37] widely used in current high-energy and astroparticle physics experiments. GEANFI incorporates a detailed description of the KLOE apparatus, including

- the interaction region: the beam pipe, the low-β quadrupoles;
- the drift chamber;
- the endcap and barrel calorimeters;

Process	Polar Angle	$\sigma(\mu b)$
$e^+e^- \to e^+e^-(\gamma)$	$20° < \theta < 160°$	6.2
$e^+e^- \to \mu^+\mu^-(\gamma)$	$20° < \theta < 160°$	0.085
$e^+e^- \to \pi^+\pi^-(\gamma)$	$20° < \theta < 160°$	0.080
$e^+e^- \to \gamma\gamma(\gamma)$	$20° < \theta < 160°$	0.30
$e^+e^- \to \omega\pi^0$		0.008
$e^+e^- \to \phi$		3.1

Table 2.1: Cross sections for several e^+e^- interaction processes at $\sqrt{s} = 1.02$ GeV. For the process $e^+e^- \to \phi$, the visible cross section is listed.

- the superconducting magnet and the return yoke structure.

A set of specialized routines has been developed to simulate the response of each detector, starting from the basic quantities obtained from the geant particle-tracking and energy-deposition routines.

2.7.1 Generators for non resonant processes and ϕ production.

GEANFI contains the code to generate the physics of interest at DAΦNE. The cross sections for the relevant processes in e^+e^- collisions at $\sqrt{s} = 1.02$ GeV are listed in tab. (2.1).

A precise Bhabha-event generator is required for the measurement of the luminosity. To reach an accuracy of a few per mil for the effective cross section, radiative corrections must be properly treated. BHAGEN, an exact $O(\alpha)$ generator based on the calculations of [38], has been implemented in GEANFI from the very beginning. More recently, the BABAYAGA [39] generator [25,26] has been interfaced with GEANFI. This generator is based on the application to QED of the parton-shower method originally developed for perturbative QCD calculations. The generator takes into account corrections due to initial-state radiation (ISR), final-state radiation (FSR), and ISR-FSR interference, and has an estimated accuracy of 0.5%. BABAYAGA can also be used to generate $e^+e^- \to \mu^+\mu^-$ and $e^+e^- \to \pi^+\pi^-$ events.

The process $e^+e^- \to \omega\pi^0$ is simulated with all ω decay modes enabled, the ω width taken into account, and a $1 + cos^2\theta$ dependence assumed for the $\omega\pi^0$ angular distribution. In particular, the process $e^+e^- \to \omega\pi^0$ with $\omega \to \pi^0\gamma$ is one of the background channels for the analysis of the decay $\eta \to \pi^0\gamma\gamma$; it is treated according to the VMD matrix element described in

[40].

The routines in the geant library simulate two and three body decays according to pure phase-space distributions. Only the main decay modes of muons, pions, kaons, and mesons are simulated. We have enriched the list of simulated particle-decay modes to include rare decays and refined the kinematic distributions of the secondaries to include the correlations expected from the matrix elements for the different decay processes.

The generator for ϕ events selects the ϕ decay channel and declares the decay products to GEANT. Initial-state radiation and the beam-energy spread of the machine ($\Delta E_{beam}/E_{beam} = 0.05\%$) are taken into account event by event in the simulation of the decay kinematics.

2.7.2 Machine background simulation.

A detailed simulation of detector activity due to the accidental coincidence of hits from machine background is required in order to obtain the high precision and careful control of systematics needed for most physics analyses. This activity consists mainly of noise hits in the DC and low-energy clusters in the EmC, mostly at small angles. Background hits in the chamber and calorimeter are added to the simulated events at the reconstruction stage.

For the 2001–2002 data, this background was obtained from $e^+e^- \to \gamma\gamma$ events satisfying specific topological cuts. These events are selected from the data with a cross section of ~ 40 nb. Since $e^+e^- \to \gamma\gamma$ events are fully neutral, all DC hits in these events are considered background, in addition to all EmC clusters not identified as belonging to the $\gamma\gamma$ topology (care is taken to correctly distinguish clusters from initial state radiation or from cluster splitting, which actually belong to the $\gamma\gamma$ topology, from those due to machine background).

We insert the hits from each background selected event into multiple events in the corresponding MC run, with a reuse factor chosen to ensure that all background events are used roughly the same number of times. This ensures reproduction of the time-variable background spectrum in the simulated output.

For both the EmC and DC, when hits are inserted, their timing relative to the start time of the $\gamma\gamma$ event from which they were extracted is preserved.

In the drift chamber, a background hit that arrives earlier than a simulated hit on the same wire causes the simulated hit to be removed from the event, and vice versa. On the calorimeter, if both a background hit and a simulated hit occupy the same cell, the time of the earlier hit is retained, while the energy is taken as the sum of the two hits energy.

Chapter 3

$\eta \to \pi^0\gamma\gamma$ - Analysis.

In this chapter we will show the analysis strategy used to search for $\eta \to \pi^0\gamma\gamma$ events. The production mechanism will be described and a detailed study of the background channels will be given.
The analysis tools that we have developed and used in this work are presented. Data-Monte Carlo comparisons are shown for the relevant selection variables. The analysis results will be given in the next chapter.

3.1 η production mechanism at KLOE.

The DAΦNE machine is a ϕ factory. The ϕ meson is produced in the process $e^+e^- \to \phi$ with a cross section of ~ 3.1 μb. The ϕ meson decays in the η particle with a branching fraction of ~ 1.3 % [1]. The present analysis is done with the DATA sample collected during years 2001 and 2002, corresponding to a total integrated luminosity of $\sim 450\, pb^{-1}$. The total number of produced ϕ mesons is 1.5×10^9 that leads to 2.0×10^7 η mesons produced. Then the η decays into the searched channel $\eta \to \pi^0\gamma\gamma$. The π^0 decays into two photons almost every time being $Br(\pi^0 \to \gamma\gamma) = 98.798 \pm 0.032$ %. The final state of the whole process is the production of 5 γ's. The production and decay chain has been depicted in fig. (3.1).
To identify the signal we will look for a peak in the energy distribution of photons. In fact, being the $\phi \to \eta\gamma$ a two body decay, from energy-momentum conservation one gets that the γ is a monochromatic photon. Defining p_ϕ, p_η and p_γ the quadrimomenta of ϕ, η and γ respectively, we can write:

$$p_\phi = p_\eta + p_\gamma \Leftrightarrow p_\eta^2 = (p_\phi - p_\gamma)^2 \Leftrightarrow m_\eta^2 = m_\phi^2 - 2 \cdot m_\phi E_\gamma \Leftrightarrow E_\gamma = \frac{1}{2}\left(m_\phi - \frac{m_\eta^2}{m_\phi}\right)$$

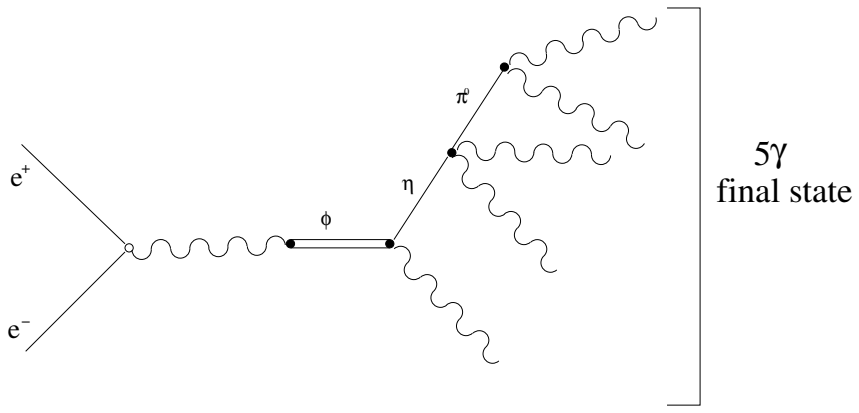

Figure 3.1: Scheme of the production mechanism of the η meson and decay chain into the $\pi^0\gamma\gamma$ final state .

where E_γ is evaluated in the ϕ rest-frame. Using the values $m_\phi = 1019.456 \pm 0.020\ \mathrm{MeV}/c^2$, $m_\eta = 547.75 \pm 0.12\ \mathrm{MeV}/c^2$ one obtains $E_\gamma = 362.67 \pm 0.07$ MeV.

3.2 Background to the $\eta \to \pi^0\gamma\gamma$ process.

As described in the previous chapter (see sec. 1.9) the measured branching ratio for the $\eta \to \pi^0\gamma\gamma$ channel lies in the range $(2.7 - 8.4) \times 10^{-4}$. Taking into account the $e^+e^- \to \phi$ cross section and the $\phi \to \eta\gamma$ branching ratio, the corresponding cross section is between 11 and 36 *pb*. The main background channels are reported in tab. (3.1) together with their effective cross sections. They come from the ϕ decays to neutral kaons, f_0, a_0,η, Bhabha scattering and $e^+e^- \to \gamma\gamma$.

3.2.1 K_L crash, $K_S \to 2\pi^0$

The $\phi \to K_L K_S$ can emulate the signal topology if a K_L enters the calorimeter (K_L crash) and a K_S decays into two pions. In fact, being the ϕ almost

channel	σ (nb)
$\phi \to K_L(crash)K_S(\to \pi^0\pi^0)$	175
$\phi \to K_L(\to 3\pi^0)K_S(\to \pi^0\pi^0)$	37
$\phi \to K_L(\to 3\pi^0)K_S(\to \pi^+\pi^-)$	239
$\phi \to f_0(f_0 \to \pi^0\pi^0)\gamma$	0.30
$\phi \to a_0\gamma, a_0 \to \eta\pi^0, \eta \to \gamma\gamma$	0.26
$\phi \to \eta(\eta \to 3\pi^0)\gamma$	13.8
$\phi \to \eta(\eta \to \pi^+\pi^-\pi^0)\gamma$	10
$\phi \to \eta(\eta \to \gamma\gamma)\gamma$	16.9
$\phi \to \pi^0(\eta \to \gamma\gamma)\gamma$	4.16
$\phi \to \rho^0\pi^0, \rho^0 \to \eta(\to \gamma\gamma)\gamma$	0.04
$\phi \to \rho^0\pi^0, \rho^0 \to \pi^0\gamma$	0.11
$e^+e^- \to \omega(\omega \to \pi^0\gamma)\pi^0$	0.45
$e^+e^- \to \gamma\gamma$	7.5
$e^+e^- \to e^+e^-(\gamma)$	1.5×10^3

Table 3.1: Background for the $\eta \to \pi^0\gamma\gamma$ decay. The values are obtained from [8]. For the f_0 and a_0 we use the KLOE measured value of the branching ratios $\phi \to f_0\gamma$ [41], $\phi \to a_0\gamma$[42]. The Bhabha and gamma gamma contribution are evaluated using a polar angular cut of 18° and a minimum energy of 5 MeV for the radiated photons using the BABAYAGA Monte Carlo generator [39].

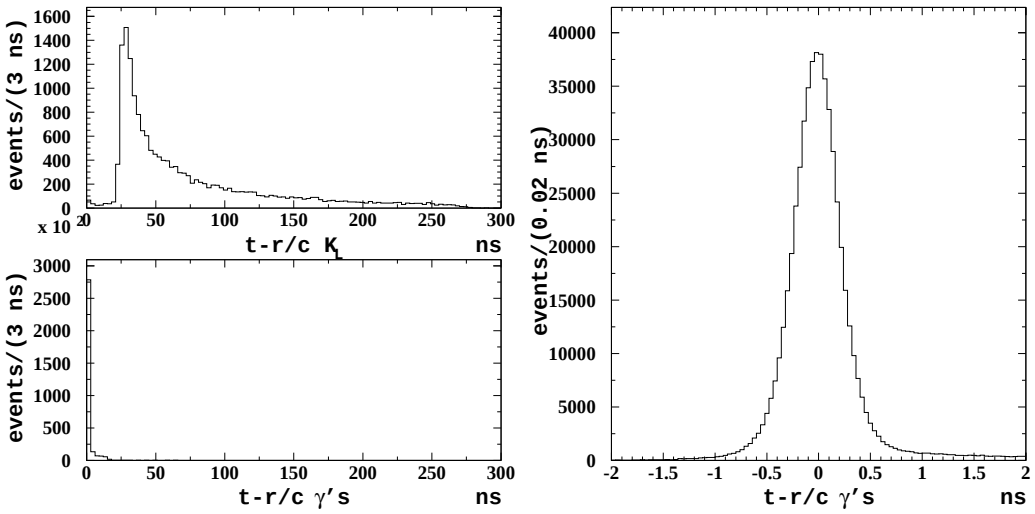

Figure 3.2: $t - r/c$ distributions: (left top) clusters generated by K_L crash, (left bottom) clusters generated by photons produced at I.P, (right) particular view of clusters generated by photons produced at I.P.

at rest, the two kaons are produced with an energy of 509.8 MeV, their γ is therefore 1.024, the K_L mean free path is therefore 3.36 m. Being the mean distance of the calorimeter walls from the Interaction Point (IP) 2.4 m, about 1/2 of K_L reach the calorimeter where they undergo hadron interactions (K_L crash). The K_S instead, having a mean free path of 0.6 cm, decay close to the interaction point.
At the end we have 5 calorimeter clusters and no track, a situation that can emulate the signal. This type of background can be easily rejected using the time information provided by the calorimeter. In fact the K_L spend in average about 30 ns to reach the calorimeter, while the photons only 7 ns. So the cluster associated to the K_L crash is much later than the clusters associated to the $K_S \to \pi^0\pi^0$ decay. In the $\phi \to \eta(\to \pi^0\gamma\gamma)\gamma$ process one has five photons coming from the IP. Knowing the cluster position $\vec{r}_{clu}$ and the cluster time t_{clu} one must have $t_{clu} - \frac{|\vec{r}_{clu}|}{c} \sim 0$ (clusters with this property are called prompt clusters). In fig. (3.2) the $t - r/c$ variable is shown for K_L crash and photons. There the selection power of this variable can be appreciated.

3.2.2 $K_L \to 3\pi^0$, $K_S \to \pi^0\pi^0$

The process $\phi \to K_L K_S$,$K_L \to 3\pi^0$, $K_S \to \pi^0\pi^0$ produces ten photons in the final state. This could simulate the signal if 5 photons are lost. Cutting

on the time of the photons is possible to reject the main part of the events and only the events in which the K_L decays near the interaction point are potential background. In the case of not detected photons a cut on the total energy of the prompt photons easily rejects this background.

3.2.3 $K_L \to 3\pi^0$, $K_S \to \pi^+\pi^-$

The $K_L \to 3\pi^0$, $K_S \to \pi^+\pi^-$ could reproduce the signal if the π^+ and π^- tracks are not reconstructed in the drift chamber. In this case the two pions produce two clusters in the calorimeter that, together with the 6 photons coming from the K_L decay, produce 8 clusters. If three of them are lost, the signal topology is reproduced. This background is rejected by the time constraint too. In fact the K_L is compelled to decay near the interaction point while the charged pions have $\beta \sim 0.85$, thus not satisfying the prompt clusters condition.

3.2.4 $f_0\gamma$, $a_0\gamma$, $\omega\pi^0$ and $\rho^0\pi^0$.

The $\phi \to f_0(\to 2\pi^0)\gamma$ ends in a 5 γs final state reproducing exactly the $\eta \to \pi^0\gamma\gamma$ topology. The only way to reduce this background is to reject events in which 2 π^0 are found. This is done by rejecting events with two pairs of photons such that each one has the π^0 invariant mass. In the $\eta \to \pi^0\gamma\gamma$ case we have, in fact, only a pair of photons giving the π^0 mass.
The same considerations are valid for $\phi \to a_0(\to \eta\pi^0)\gamma$ with $\eta \to \gamma\gamma$. In this case a veto on the $\eta \to \gamma\gamma$ invariant mass is imposed.
The $e^+e^- \to \omega\pi^0$ is a not resonant process. This means that it is not mediated by the ϕ particle. It is a background source if ω decays into $\pi^0\gamma$. In this case we end up with a $\pi^0\pi^0\gamma$ final state. It can be rejected as the f_0 background but in this case also a constraint on the mass of the $\pi^0\gamma$ system can be imposed to veto the ω mass.
The $\rho^0\pi^0$ channel is a background candidate when $\rho \to \eta(\to \gamma\gamma)\gamma$ and $\rho \to \pi^0\gamma$. It is easily rejected by the criteria used to reject f_0 and a_0.

3.2.5 Accidental clusters background.

The $\phi \to \eta(\eta \to \gamma\gamma)\gamma$, $\phi \to \pi^0(\pi^0 \to \gamma\gamma)\gamma$, $e^+e^- \to \gamma\gamma$ are all events with less than 5 photons. These can emulate the 5 photons topology if clusters due to the machine background add up to the events producing a 5 cluster topology. As we will show later the machine background is mainly

concentrated at small angle and low energy. A cut on the minimum energy of the cluster and their angle fully rejects this background.
The same consideration is valid for the Bhabha process $e^+e^- \to e^+e^-$, if the two charged tracks are not reconstructed. Electrons travel almost at the same velocity of photons and cannot be rejected by a time requirement. Anyway the Bhabha angular distribution is very peaked at small angles, so an angular cut rejects almost all of them.

3.2.6 $\eta \to 3\pi^0$

The $\phi \to \eta(\to 3\pi^0)\gamma$ channel has 7 photons in the final state. It can emulate the signal in three different cases: two photons are lost, one is lost and two merge together and, finally, if two pairs of photons merge together into two clusters. These three cases are treated in different ways as explained in the following.

3.3 Event preselection, the EVCL algorithm.

The selection criteria described above are partially applied at DATA reconstruction level. After DATA acquisition the event are processed by the background rejection filter, FILFO, described in section (2.6). After that a further module called EVCL, event classification, divide the full data sample in several, not disjointed, sets (streams). The events we are looking for are collected in the so called "Neutral Radiative Stream". It contains events with an arbitrary number of gammas.
The selection criteria are the following:

- at least three prompt clusters which are not associated to the DC reconstructed tracks by the "Track to Cluster" algorithm (see sec. 2.5);
- the total energy of the prompt clusters (prompt energy) must be greater than 700 MeV to reject kaon background and charged event background.

The effect of this last cut is shown in fig. (3.3) for Monte Carlo simulated events.

3.4 Time and number of clusters.

The events which we are looking for have only prompt photons. We look for five clusters in the calorimeter and impose a time constraint on the clusters

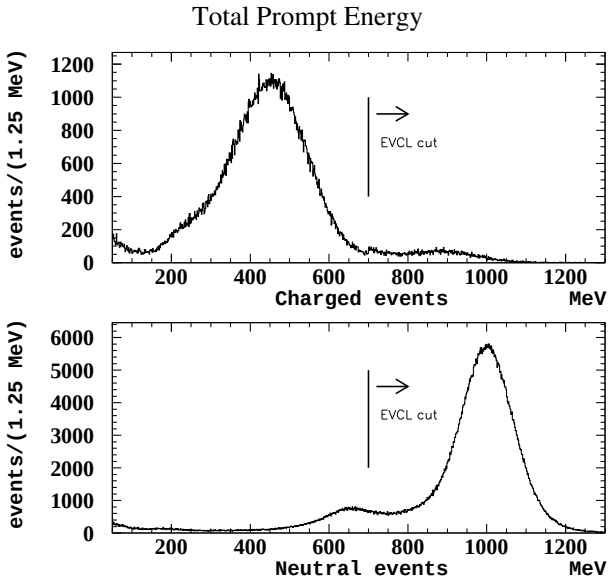

Figure 3.3: Total prompt energy (MC simulation): **top** events with at least 2 charged tracks in the final state; **bottom** neutral events. The EVCL cut is shown. The two samples are independent.

as explained before. The mean position of the interaction point is known run by run from the analysis of Bhabha scattering events. Given the cluster position $\vec{r}_{clu}$, the average vertex position $\vec{r}_{vtx}$ and the cluster time t_{clu}, we require that each cluster satisfies the following relation:

$$\left| \frac{|\vec{r}_{clu} - \vec{r}_{vtx}|}{c} - t_{clu} \right| < min(5\sigma_t, 2ns) \tag{3.1}$$

where σ_t is a function of the cluster energy:

$$\sigma_t = \sqrt{\frac{(54\text{ps})^2}{\sqrt{E[GeV]}} + (140\text{ps})^2}$$

The time resolution is worse at low energy, this means that without the 2 ns condition many fake clusters could enter in the event. For this reason we require 5 and only 5 clusters which satisfy equation (3.1).
The simpler requirement of just 5 clusters is not a good choice. This can be seen in fig. (3.4) where the number of clusters expected from Monte Carlo simulation is shown both for signal and background after the EVCL selection. As we can see large part of the signal events have more than 5 clusters due

to accidental clusters. In fig. (3.5) we have reported the number of prompt clusters. In this case only a minor part of signal events has more than five prompt clusters, while the background is much reduced with a 5 prompt clusters requirement.

To improve the energy resolution a fit procedure has been applied that compells the photons to close the kinematic. This procedure is described in the following section.

3.5 Kinematic fit.

Given a set of measured quantities x_i, we indicate with x_i^{true} their true values. x_i is the best approximation of x_i^{true}. In most cases x_i is normal distributed around x_i^{true} with standard deviation σ_i. If the variables x_i^{true} are constrained by some physical law (energy-momentum conservation for example), they must satisfy k equations, that we can write in implicit form:

$$F_j(x_k^{true}) = 0 \quad j = 1, \ldots, k \tag{3.2}$$

The fit procedure finds a new approximation (μ_i) of x_i^{true} by minimizing the quantity:

$$\chi^2 = \sum_i \frac{(x_i - \mu_i)^2}{\sigma_i^2}$$

and imposing the (3.2) constraints on μ_i. This has been done using the lagrangian multipliers method, that consists in minimizing the quantity:

$$\chi^2 = \sum_i \frac{(x_i - \mu_i)^2}{\sigma_i^2} + \sum_j \lambda_j F_j(\mu_k) \tag{3.3}$$

respect to the variables μ_i and λ_j. To this purpose an iterative procedure has been developed.
In our case the x_i are the following variables:

- the time of the 5 clusters, t_i;
- the position of the clusters centroid x_i, y_i, z_i;
- the clusters energy E_i;
- the mean position of the interaction point (IP) X_{IP}, Y_{IP}, Z_{IP};
- the mean value of the ϕ quadrimomentum P_X, P_Y, P_Z, E.

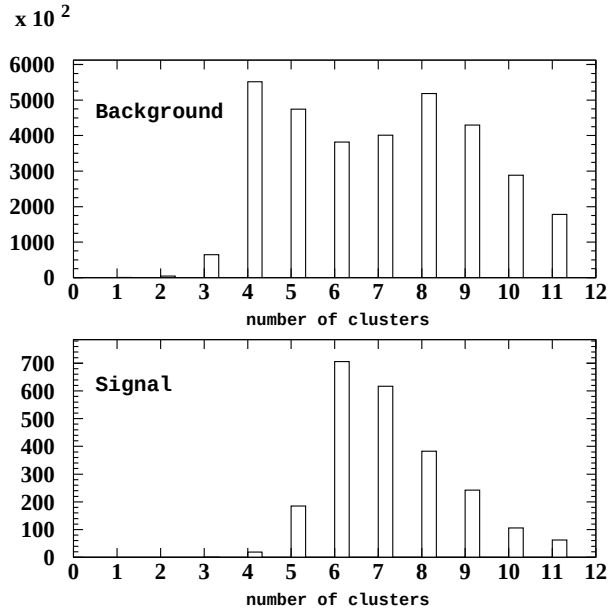

Figure 3.4: Number of clusters for background and signal (Monte Carlo simulation).

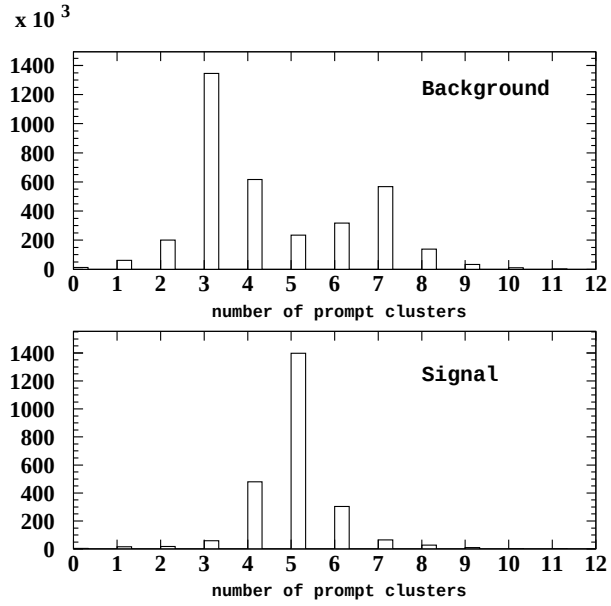

Figure 3.5: Number of prompt clusters for background and signal (Monte Carlo simulation).

Variable	σ
E	$\left(0.057/\sqrt{E(\text{GeV})} + 0.006\right) \cdot E$
X	1.4 cm
Y (barrel) Z (end-cap)	1.4 cm
Z (barrel) Y (end-cap)	$1.4\text{cm}/\sqrt{E}$ (GeV)
t	$\sqrt{(0.14)^2 + (0.054)^2/E\ (\text{GeV})}$ ps

Table 3.2: Resolutions used in the kinematic fit. These values are used both for DATA and MC.

The last two quantities are determined run by run with a dedicated algorithm that works on Bhabha scattering events at large angle.
The total reconstructed variables are 32. On them we impose 9 constraints: 5 of them are the time of flight of photons, one for each cluster:

$$t_j - \frac{r_j}{c} = 0$$

$$r_j = \sqrt{(x_j - X_{vtx})^2 + (y_j - Y_{vtx})^2 + (z_j - Z_{vtx})^2}$$

where j runs on the five photons. The other four constraints are the energy-momentum conservation:

$$P_{X,Y,Z} = \sum_{i=1}^{5} P^{\gamma_i}_{X,Y,Z}, \quad E = \sum_{i=1}^{5} E^{\gamma_i}$$

where:

$$P^{\gamma_i}_X = \frac{x_i - X_{vtx}}{r_i} E^{\gamma_i}, \quad P^{\gamma_i}_Y = \frac{y_i - Y_{vtx}}{r_i} E^{\gamma_i}, \quad P^{\gamma_i}_Z = \frac{z_i - Z_{vtx}}{r_i} E^{\gamma_i}$$

The σ_i are reported in tab. (3.2). The effect of the kinematic fit is shown in fig. (3.6) where the energy spectrum of $\eta \to \pi^0\gamma\gamma$ is shown before and after the kinematic fit for Monte Carlo simulated events.
In the figure we can see that the photon energy resolution has a big improvement thanks to the energy-momentum constraint. In fig. (3.7) we have reported also the spectrum for the $\eta \to 3\pi^0$ background.In this case no resolution improvement is observed, this is simply due to the lost photons that don't allow to close the kinematic. On top of the distribution one can see a small structure around 363 MeV. This is due to the $\eta \to 3\pi^0$ background when there is the merging of two pairs of clusters. In this case there isn't

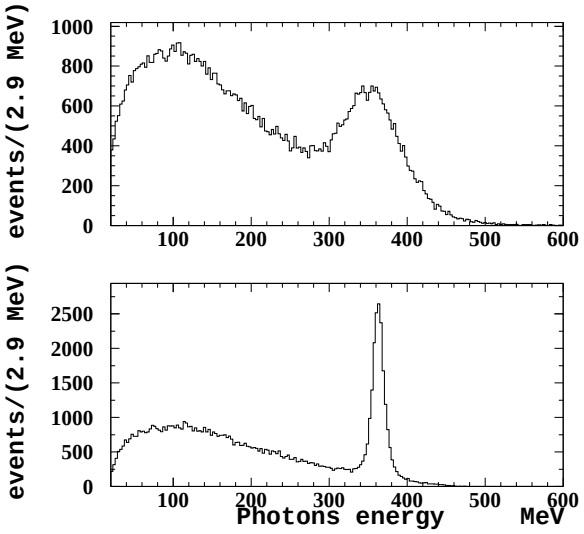

Figure 3.6: Inclusive photons energy distribution before (top) and after (bottom) the kinematic fit procedure. The improvement in the photon energy resolution is evident. (MC)

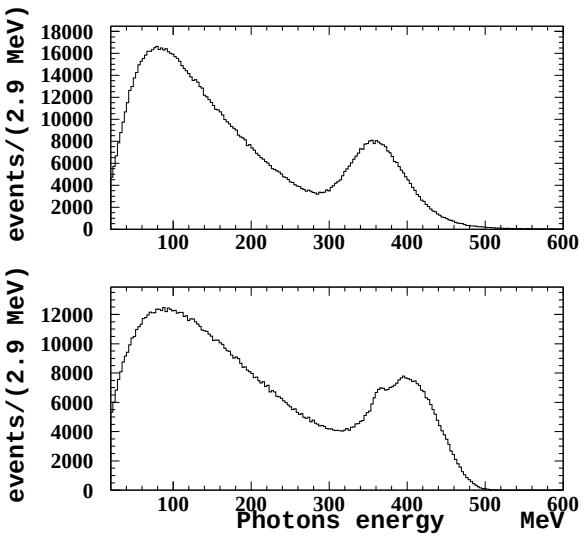

Figure 3.7: Inclusive photon Energy distribution before (top) and after (bottom) the kinematic fit for $\eta \to 3\pi^0$. The small excess around 363 MeV is due to the case of two merged photons (see text).

	mass fit (MeV)	sigma fit (MeV)	mean (MeV)	rms (MeV)
MC	134.93 ± 0.04	6.95 ± 0.05	135.2	5.228
DATA	135.08 ± 0.07	6.80 ± 0.09	135.3	5.197
Difference	0.15 ± 0.08	0.15 ± 0.10	–	–

Table 3.3: m_π^0 values. The DATA-MC discrepancy is less than 2 sigmas both on the central value than on the sigma. Furthermore they are in agreement with the PDG value (134.9766 ± 0.0006) MeV [8].

missing momentum and the kinematic is correctly closed, so the fit improves the energy resolution.

To test the ability of the Monte Carlo simulation to reproduce this effect, we have selected a control sample enriched with events with 5 and only 5 photons coming from the IP. This sample is dominated by the process is $e^+e^- \to \omega(\to \pi^0\gamma)\pi^0$.

It has five prompt photons in the final state and 2 π^0 as intermediate state. We can check the photon energy resolution before and after the kinematic fit simply by comparing the π^0 mass. To select this sample, reducing $\eta \to 3\pi^0$ contribution, we require that:

- the total energy is greater than 1000 MeV and the total momentum is less than 100 MeV. The total momentum versus the total energy histogram is shown in fig.(3.8), together with the selection region.
- a minimum cluster energy greater than 20 MeV and angle greater than 25°, to reject accidental clusters.

In fig. (3.9) we show the $m_{\gamma\gamma}$ distribution before and after the kinematic fit for both DATA and MC. The energy resolution improvement is evident.

To compare better the shape of the peak, a direct comparison has been made normalizing the histogram in the range 125 - 145 MeV/c^2. The very nice agreement is shown in fig.(3.10).

A quantitative comparison has been performed fitting these distribution around the peak. The obtained values are reported in tab. (3.3) while the fit result is shown in fig.(3.11).

Also the stability of the fitted value as a function of the photon energy has been checked by fitting the $m_{\gamma\gamma}$ distribution with a double gaussian plus a 2^{th} degree polynomial as a function of the energy of one of the two photons. The photon energy range, [40-400] MeV, has been divided into 40 MeV wide

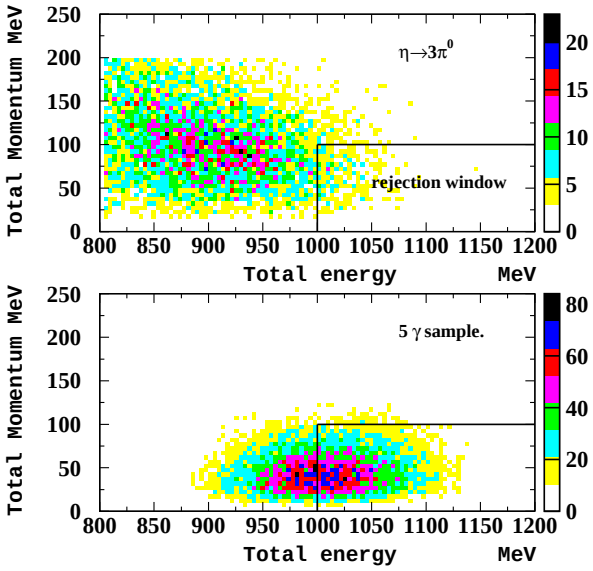

Figure 3.8: Total momentum versus total energy distribution: **top:** $\eta \to 3\pi^0$ MC sample, **bottom** 5 γ MC sample. The window used to reject the $\eta \to 3\pi^0$ sample is shown.

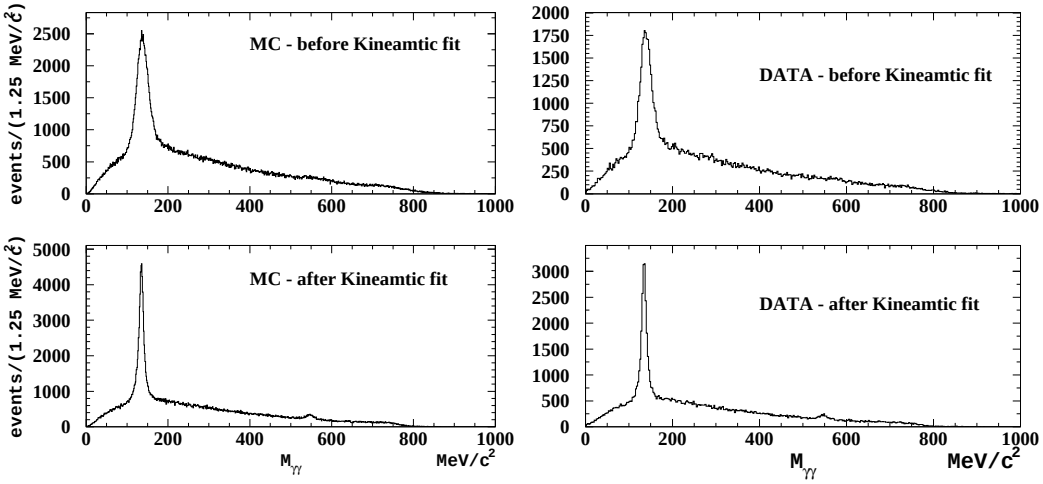

Figure 3.9: Invariant mass distribution before and after the kinematic fit, for MC (left) and DATA (right). After the kinematic fit also the $\eta \to \gamma\gamma$ decay coming from $a_0 \to \eta\pi^0$ is visible.

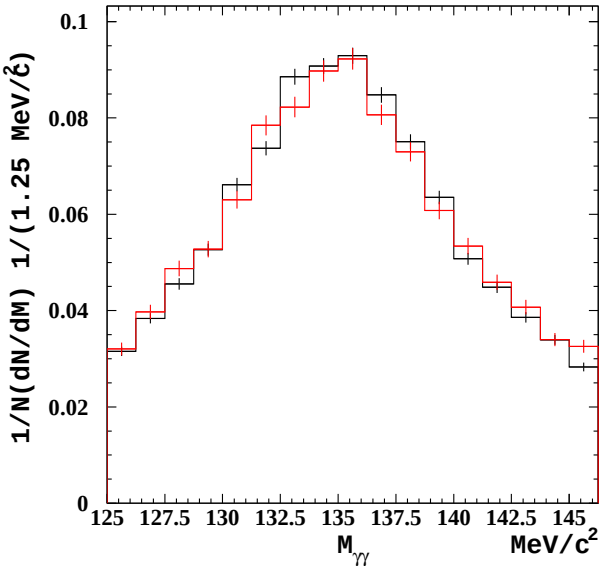

Figure 3.10: DATA-MC comparison for $m_{\gamma\gamma}$ spectrum at the π^0 peak after the application of the kinematic fit, black line MC gray line DATA.

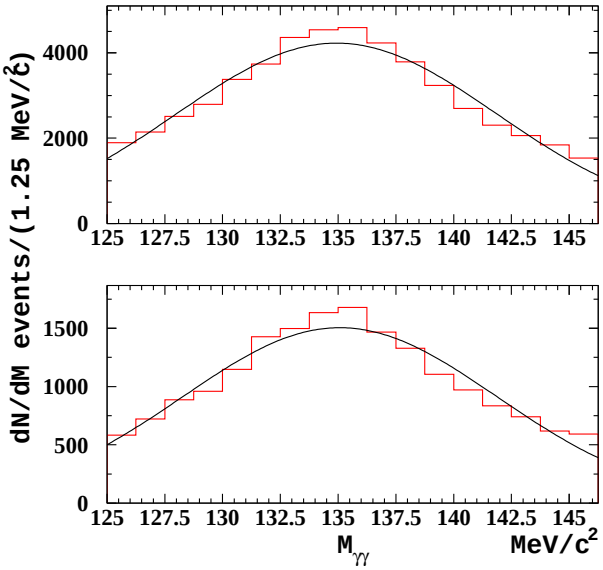

Figure 3.11: Fit to m_{π^0}: (top) MC (bottom) DATA.

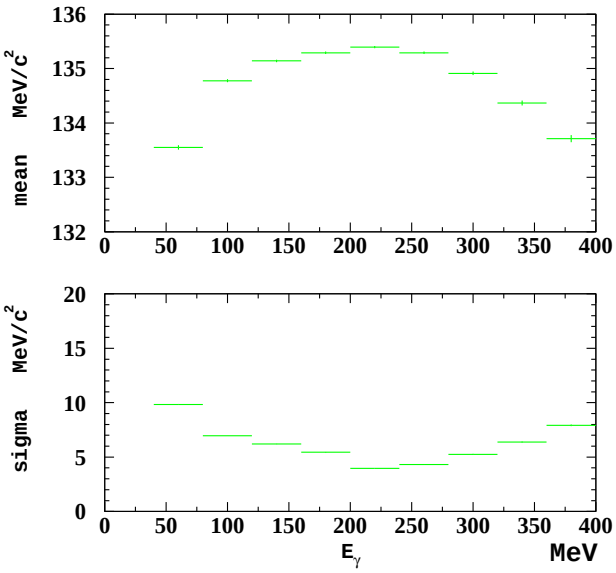

Figure 3.12: m_{π^0} as a function of the photon energy.

	mass fit (MeV)	sigma fit (MeV)
MC	547.38 ± 0.13	9.3870 ± 0.16
DATA	546.65 ± 0.36	10.37 ± 0.48
Difference	0.73 ± 0.38	0.987 ± 0.51

Table 3.4: m_η and sigma value for DATA and MC. The difference is below 2 sigma.

bins, the results are reported in fig.(3.12). Variation below 1% are observed.

The same comparison has been done around the η mass using the sample $\phi \rightarrow a_0\gamma, a_0 \rightarrow \eta\pi^0, \eta \rightarrow \gamma\gamma$, in this case, due to the large presence of background, also the background has been fitted from the sidebands. The histogram has been fitted with a gaussian plus a straight line. The fit results are reported in tab. (3.4) and the fitted histograms are shown in fig.(3.13).

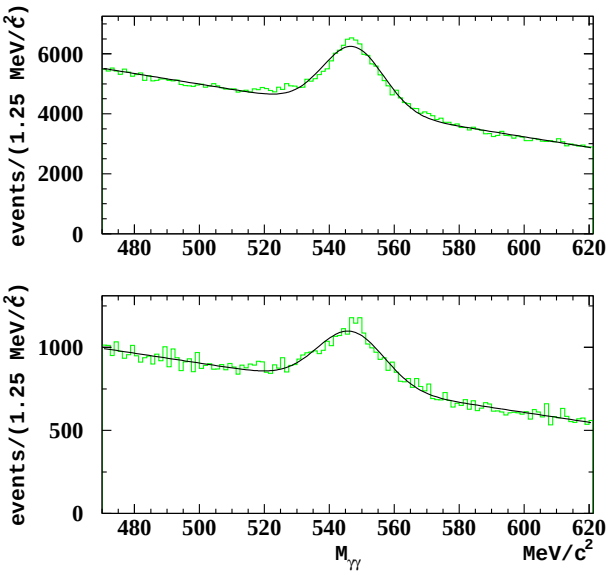

Figure 3.13: m_η fit: (top) Monte Carlo, (bottom) DATA.

3.6 Selection variables.

After the first kinematic fit a second kinematic fit is done requiring also the π^0 mass constraint. In this case we have a total of 10 possible combination; one for each way to associate a pair of photons to the π^0.
The input to this fit are the calorimeter reconstructed variables, not the output of the previous fit. The constraints are the same with the adjoint of the π^0 mass. All combinations are tried and the least $\chi^2_{\pi^0}$ value is retained and used as selection variable.
This variable is used to cut the relevant background that don't close correctly the kinematic, such as kaons background and $\eta \to 3\pi^0$ background.
The $\chi^2_{\pi^0}$ is not useful to reject $\phi \to \eta\gamma$, $\phi \to \pi^0\gamma$ and $e^+e^- \to \gamma\gamma$ background. In this case the adjoint of two background clusters can easily close the kinematic.
The background cluster energy is, anyway, pushed to zero by the first kinematic fit. These events, in fact, are able to close the kinematic with only three photons, the other two are compelled to acquire value near to zero or negative. This can be seen in fig. (3.14) where the energy of all photons after the kinematic fit is shown.
To cut this background we cut on the minimum energy of the photons after

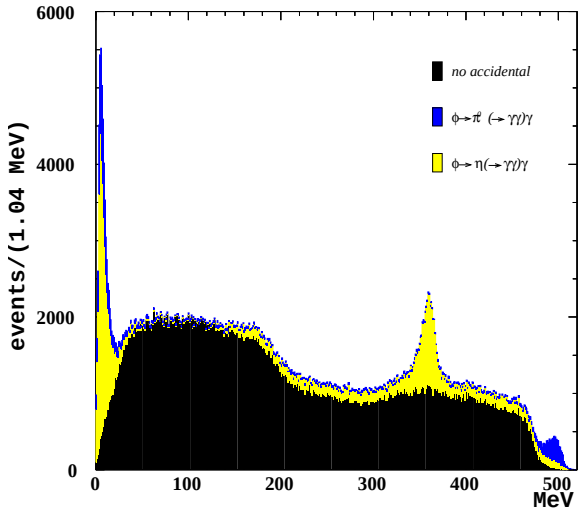

Figure 3.14: Energy distribution of the five photons after the kinematic fit, the contribution from the $\phi \to \eta\gamma$ and $\phi \to \pi^0\gamma$ plus accidentals together with the 5γ events is shown. The accidental clusters are pushed around the 0 value. The peack at 363 MeV and 500 MeV comes from the monochromtic photons of the two processes (Monte Carlo simulation).

the kinematic fit $E_{min} > 20MeV$ and with an angle greater than 21°. After this cut the MC and data distribution looks like those reported in fig.(3.15).

A DATA-MC comparison on the $\chi^2_{\pi^0}$ has been performed using the $\omega\pi^0$ control sample. The result is shown in fig.(3.16) in linear and logarithmic scale, there is in this variable a small discrepancy at small values. The error expected from this discrepancy is much below the statistical error of the final measurement (see chapter 4).

3.7 MC normalization.

In our Monte Carlo simulation there are several channels whose cross section drastically depends on the total energy in the C.M. An example is the $e^+e^- \to \omega\pi^0$ channel that is simulated with a constant cross-section around the ϕ peak while it goes down at the ϕ meson mass due to the $\omega - \phi$ interference.
For this reason the normalization of the different channels must be done to have the correct background composition. To do this we use the $m_{\gamma\gamma}$ distribution of each pair of photon. We build 7 histograms, one for each background channel that is relevant at this stage of the analysis: $\omega\pi^0, f_0\gamma,$

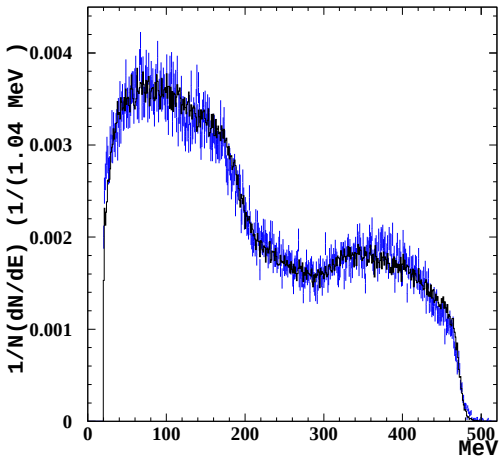

Figure 3.15: Energy distribution of the five photons after the kinematic fit (MC black continuous line DATA blue error bars), the background due to accidental clusters has been cut.

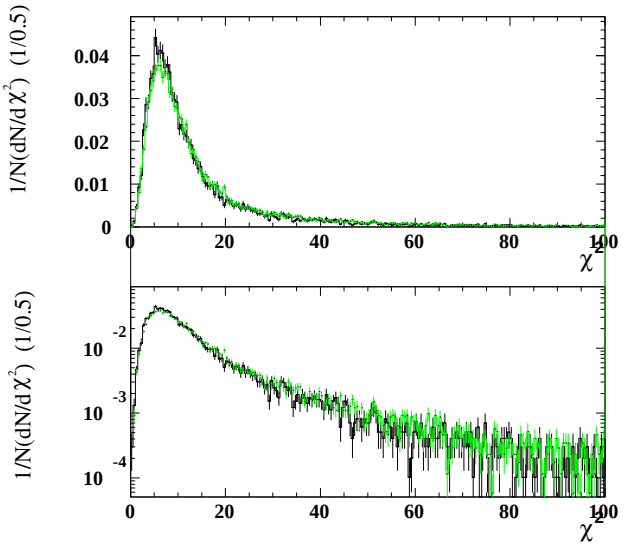

Figure 3.16: DATA-MC comparison for the χ^2 of the kinematic fit with a π^0 hypothesis, the DATA is the black line, the MC the gray one.

Channel	Correction factor
$\omega\pi^0$	0.1408 ± 0.0017
f_0	0.214 ± 0.008
a_0	0.137 ± 0.007
$\rho\pi^0$	0.09 ± 0.02
η 2 merged	0.59 ± 0.06
η 1 lost 1 merged	0.300 ± 0.019
η 2 lost	0.151 ± 0.012

Table 3.5: Correction factors applied to the simulated background channels obtained fitting the $m_{\gamma\gamma}$ spectrum. The MC statistic is 5 time the DATA statistic, so a value of 0.2 is expected if MC was right.

$a_0\gamma$, $\rho^0\pi^0$, $\eta \to 3\pi^0$. The last one is subdivided into three topologies: 2 lost photons, 1 lost photon and 1 merged cluster, 2 merged clusters. Given a pair of photons we build the invariant mass and put it in the histogram, so for each event we have 10 entries in the histogram. This is done to avoid problems of the choice of the pair of photon linked to the π^0.
We fit the DATA distribution with a linear combination of the 7 histograms, and we obtain the background content of the DATA. In tab. (3.5) we have reported the coefficients of the fit.
The result of the fit is shown in fig. (3.17). As a cross check of the result, also the invariant mass of three photons has been built. The distribution peaks at the ω mass in the case of the $\omega\pi^0$ background. Using the normalizing factors reported in tab. (3.5) one obtains the spectrum shown in fig. (3.18). As it can be ssen, the spectrum is perfectly reproduced.

3.8 $\eta \to 3\pi^0$ rejection.

A large part of background comes from the process $\eta \to 3\pi^0$ when one or two photons are lost. This happens, above all, at small angle where, due to the presence of the beam pipe, the calorimeter has two holes. Furthermore at small angle there is a lot of machine background and the clustering algorithm fails to reconstruct clusters correctly. To reject this background we have developed two dedicate kinematic fit procedures. One to reject the case in which we lose two clusters and one in which we lose one cluster and merge two other ones. In both cases we have a five cluster topology. The procedure is based on the algorithm described in [43]. It is very similar to the procedure described in sec. (3.5) but in this case we consider the momentum of the

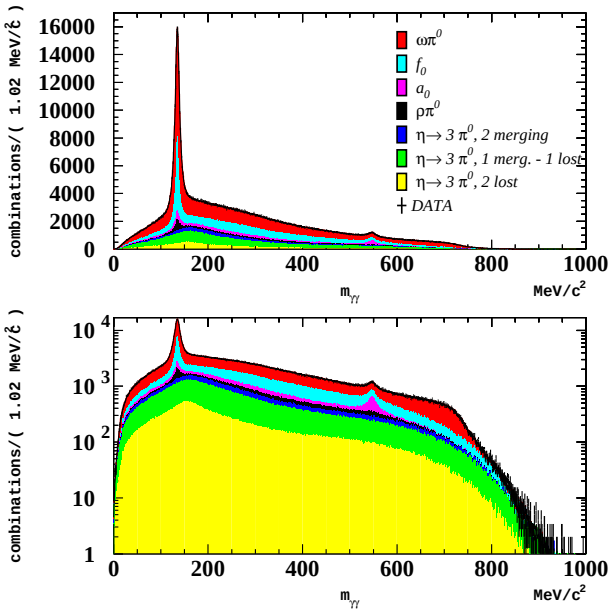

Figure 3.17: $m_{\gamma\gamma}$ spectrum fitted to obtain the normalization of the background contributions.

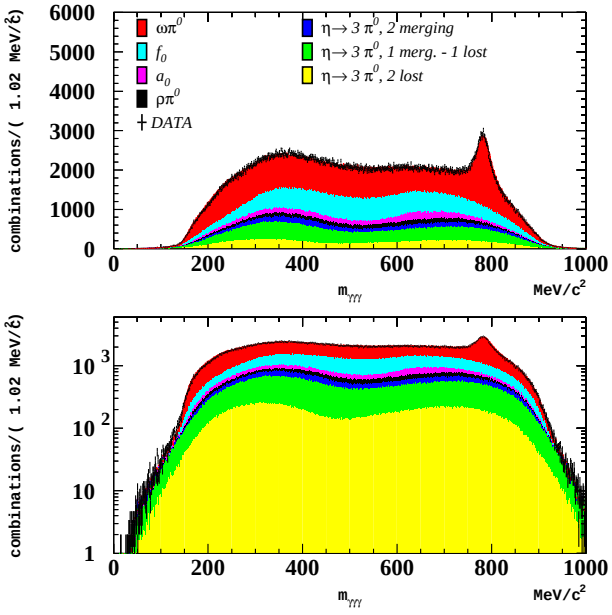

Figure 3.18: $m_{\gamma\gamma\gamma}$ obtained using the correction factors reported in tab. (3.5).

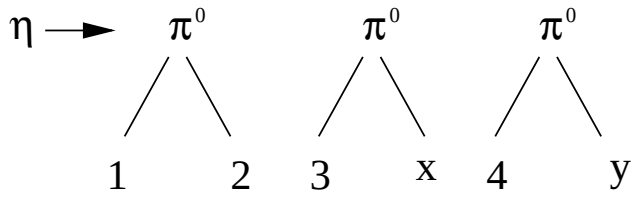

Figure 3.19: Notation scheme for the kinematic fit description.

lost photons as unknown variables. For this reason we put 3 unknowns for each lost photon in the fit corresponding to the linear momentum of the lost photons. In the fit we constraint the η mass and the masses of the 3 π^0. This means that the kinematic constraint of the fit are 4 (coming from the energy momentum conservation) plus 4 coming from the mass of the decaying particles. In this way the fit is over constrained. To have the convergence of the iterative procedure one must find some starting value for the unknowns. These are determined by solving a subset of the constraining equations. We proceed in the following way: we indicate with x and y the missing photons quadrimomenta, with p the quadrimomentum of the detected photons and with $p_{missing}$ the total missing quadrimomentum, following fig. (3.19) we can write the following system:

$$\left\{\begin{array}{rcl} x+y & = & p_{missing} \\ (x+p_3)^2 & = & m^2_{\pi^0} \\ x^2 & = & 0 \\ (y+p_4)^2 & = & m^2_{\pi^0} \\ y^2 & = & 0 \end{array}\right. \Leftrightarrow \left\{\begin{array}{l} x = p_{missing} - y \\ (p_{missing} - y + p_3)^2 = m^2_{\pi^0} \\ (p_{missing} - y)^2 = 0 \\ (y+p_4)^2 = m^2_{\pi^0} \\ y^2 = 0 \end{array}\right. \tag{3.4}$$

Defining with $\vec{p}$ the spatial component of the quadrivector p and with p^4 the time component (the energy) we can write:

$$\left\{\begin{array}{l} \vec{p}_{missing} \cdot y = p^4_{missing} y^4 - \frac{p^2_{missing}}{2} \\ \vec{p}_2 \cdot \vec{y} = p^4_2 y^4 - \vec{p}_{missing} \cdot \vec{p}_2 + \frac{m^2_{\pi^0}}{2} \\ \vec{p}_4 \cdot \vec{y} = p^4_4 y^4 - \frac{m^2_{\pi^0}}{2} \\ y^2 = 0 \end{array}\right.$$

Now we define the matrix A and the vectors $\vec{C}$ and $\vec{B}$ in the following way:

$$A = \begin{pmatrix} \vec{p}_{missing} \\ \vec{p}_3 \\ \vec{p}_4 \end{pmatrix} \quad \vec{C} = \begin{pmatrix} p^4_{missing} \\ p^4_3 \\ p^4_4 \end{pmatrix} \quad \vec{B} = \begin{pmatrix} -\frac{p^2_{missing}}{2} \\ -\vec{p}_{missing} \cdot \vec{p}_2 + \frac{m^2_{\pi^0}}{2} \\ -\frac{m^2_{\pi^0}}{2} \end{pmatrix}$$

so that the previous system can be written in the matrix form:

$$\left\{ \begin{array}{rcc} A\vec{y} & = & \vec{B} + \vec{C}y^4 \\ y^2 & = & 0 \end{array} \right. \Leftrightarrow \left\{ \begin{array}{rcc} \vec{y} & = & A^{-1}(\vec{B} + \vec{C}y^4) \\ y^2 & = & 0 \end{array} \right.$$

Substituting the upper equation in the lower one, one obtains:

$$y^2 = 0 \Leftrightarrow (y^4)^2 - |\vec{y}|^2 = 0 \Leftrightarrow$$

$$\Leftrightarrow \left(1 - |A^{-1}\vec{C}|^2\right)(y^4)^2 + 2\left(A^{-1}\vec{B} \cdot A^{-1}\vec{C}\right)y^4 + |A^{-1}\vec{B}|^2 = 0$$

This equation has a solution if and only if one has:

$$\frac{\Delta^2}{4} = \left(A^{-1}\vec{B} \cdot A^{-1}\vec{C}\right)^2 - \left(1 - |A^{-1}\vec{C}|^2\right)|A^{-1}\vec{B}|^2 \geq 0$$

The parameter Δ^2 evaluated in this way is used as a cut parameter. It is able, in fact, partially to reject the $\eta \to 3\pi^0$ with 2 γs lost background.
The momenta evaluated solving the system (3.4) are put as starting values in the kinematic fit algorithm. Often the algorithm doesn't reach the convergence. This happens more for signal than for background. This effect can be used as a further selection criteria (failing convergence means that the event is not able to satisfy all constraints). In tab. (3.6) we have reported efficiency and background rejection using two criteria: $\Delta^2 < 0$ and [$\Delta^2 < 0$ OR no convergence]. When the fit converges the χ^2 of the kinematic fit is

	$\Delta < 0$	$\Delta < 0$ OR no convergence
$\epsilon(\eta \to \pi^0\gamma\gamma)$	79.05 ± 0.19 %	95.25 ± 0.10 %
$\epsilon(\eta \to 3\pi^0)$ 2 lost	33.55 ± 0.07 %	51.63 ± 0.08 %

Table 3.6: Selection efficiency for signal and background for the two criteria (see text).

shown in fig. (3.20) for signal and background.

The 1 lost - 1 merged case has been treated in the same way. In this case we assume that the merged cluster is the sum of the energy of the two photons which contribute to it. The procedure is very symilar to the 2 lost case, only the unknown physical quantities are changed. In this case we have 5 unknowns: the lost photon momentum and the energy of the two photons contributing to the cluster. To obtain the starting values, following the convention depicted in fig.(3.21), we can write:

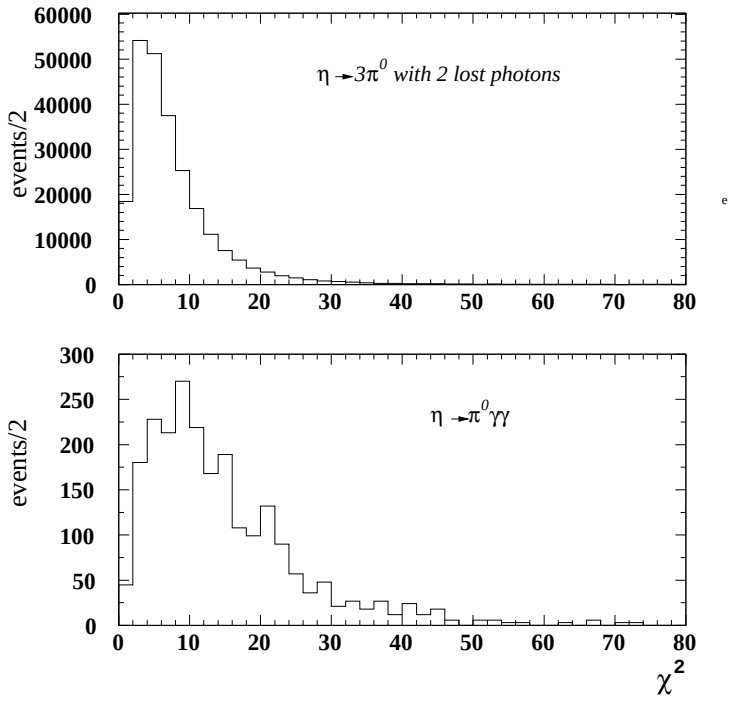

Figure 3.20: χ^2 distribution of the kinematic fit in $\eta \to 3\pi^0$ hypothesis with two lost photons for background (top) and signal (bottom).

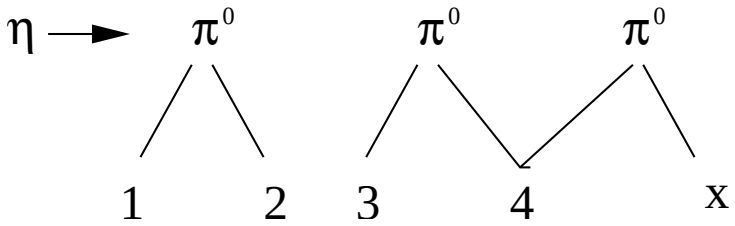

Figure 3.21: Convention scheme for the kinematic fit in the $\eta \to 3\pi^0$ hypothesis with one pair of photons merged and one photon lost.

$$\begin{cases} \vec{x} = \vec{p}_{missing} \\ (p_3 + p_{4,1})^2 = m^2_{\pi^0} \\ (x + p_{4,2})^2 = m^2_{\pi^0} \end{cases} \Leftrightarrow \begin{cases} \vec{x} = \vec{p}_{missing} \\ E_{4,1} = \frac{m^2_{\pi^0}}{E_3(1-cos\theta_{34})} \\ E_{4,2} = \frac{m^2_{\pi^0}}{|\vec{p}_{missing}|(1-cos\theta_{3x})} \end{cases}$$

In the last equation the direction of the missing photon is simply given by the the direction of the the missing momentum vector. In this case the fit converges both for signal and background and the χ^2 of the fit doesn't help (see fig. 3.22). Anyway other distributions can help. The energy of the

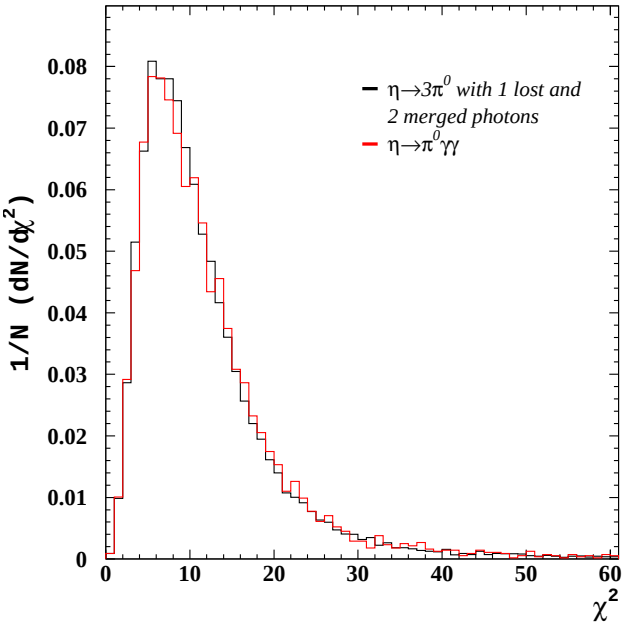

Figure 3.22: Distribution of the χ^2 of the kinematic fit in 1 lost - 2 merged case, the curves for signal and background are pratically indistinguishable.

lost photon for example and its direction. These distributions are shown in fig.(3.23) and are used to reject this background.

In the signal case the angle distribution of the lost photon identified by the fit is flat in $cos\theta$ and its energy is small. In the background case, instead, the photons are mostly lost at small angle and have higher energy in average. These distributions are indeed used to reject background.

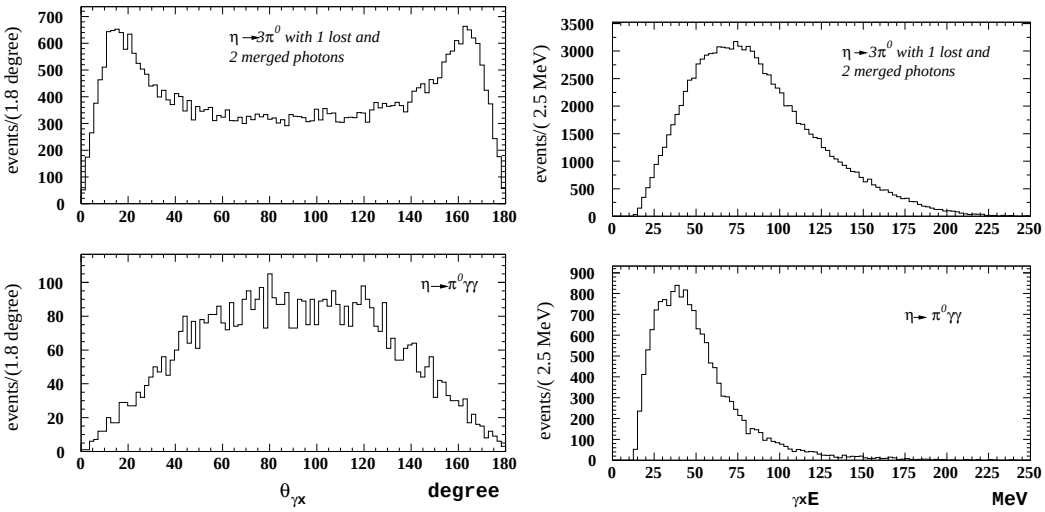

Figure 3.23: Energy and angle distribution of the lost photon as given by the kinematic fit, both for signal and background.

3.9 $\eta \to 3\pi^0$ with 2 merged clusters rejection (the likelihood function).

The $\phi \to \eta(\to 3\pi^0)\gamma$ can reproduce a 5 γ's topology if two pairs of clusters merge together into 2 clusters. In most cases the merging happens between two different π^0, so that one has a $\pi^0\gamma\gamma\gamma$ topology which is the same topology of the signal. No missing momentum is observed and the kinematic fit brings the energy of the γ coming from the $\phi \to \eta\gamma$ to its expected value, that is 363 MeV (the same of the signal), making this background really irriducible. To reduce it, a likelihood function has been built to identify the merged cluster. In fact the spatial and temporal distribution of the hits which are collected in a cluster is different for merged and not merged clusters. The variables which are used in the likelihood are:

- The rms of the x,y, z and t coordinates of the hits, so defined (x for example);

$$x_{rms} = \sum_{i=1}^{n.hits} \frac{(x_i - \bar{x})^2 \cdot E_i}{\sum_{i=1}^{n.hits} E_i} \quad \bar{x} = \sum_{i=1}^{n.hits} \frac{x_i \cdot E_i}{\sum_{i=1}^{n.hits} E_i} \tag{3.5}$$

- the skewness of the x, y, and z variables.

$$x_{skw} = \sum_{i=1}^{n.hits} \frac{(x_i - \bar{x})^3 \cdot E_i}{\sum_{i=1}^{n.hits} E_i} \tag{3.6}$$

The distributions have been studied on a sample made of events with 7 γ's, coming from the process $\phi \to \eta(\to 3\pi^0)\gamma$. The Monte Carlo distributions have been corrected to reproduce the DATA distributions, in order to have a good DATA-MC agreement. The clusters have been divided into two subsets. Those with more than 3 hits (calorimeter cells in the cluster) and those with 3 hits. This because the distributions look quite different for the two cases. Four likelihood variables have been built: 2 for the two endcaps and 2 for the barrel.
The likelihood is built in the following way:

- the distribution of the variables defined in equations (3.5) and (3.6) are normalized, and they give the p.d.f functions of the variables (let's call them v_i), $f(v_i)$. The $f(v_i)$ are different for good clusters and merged clusters, so we will have $f^{good}(v_i)$ and $f^{merged}(v_i)$.

- The likelihoods for good and merged clusters are built according the formula:

$$\mathcal{L}^{good,merged}(v_1, v_2, ..., v_n) = \prod_i f_i^{good,merged}(v_i)$$

- The logarithmic of the ratio of the two likelihood

$$r = log\left(\frac{\mathcal{L}^{good}}{\mathcal{L}^{merged}}\right)$$

  is built and used as discriminating variable.

In fig. (3.24) the DATA-MC comparison of r for good clusters is reported. The distributions are in good agreement. In fig. (3.25) we show the r distribution for merged clusters and for not merged clusters. As one can see r is able to distinguish between the two cases.

3.10 The f_0, a_0 , $\omega\pi^0$ and $\rho^0\pi^0$ rejection.

This type of background produces five prompt neutral clusters in the calorimeter, anyway they can be rejected by vetoing the particles in the final state. The f_0 and $\omega\pi^0$ have 2 π^0 in the final state, while the a_0 has an η that undergoes a 2 γ decay. The veto is done by rejecting configurations in which 2 pairs of photons, whose invariant mass is the π^0 one, are found, or one with a π^0 and one with an η. To reject $\omega\pi^0$ also the $m(\omega)$ mass is vetoed . To do this we build three discriminating variables:

$$S^2(2\pi^0) = \frac{(m(\gamma_1\gamma_2) - m(\pi^0))^2}{\sigma^2_{m(\pi^0)}} + \frac{(m(\gamma_3\gamma_4) - m(\pi^0))^2}{\sigma^2_{m(\pi^0)}}$$

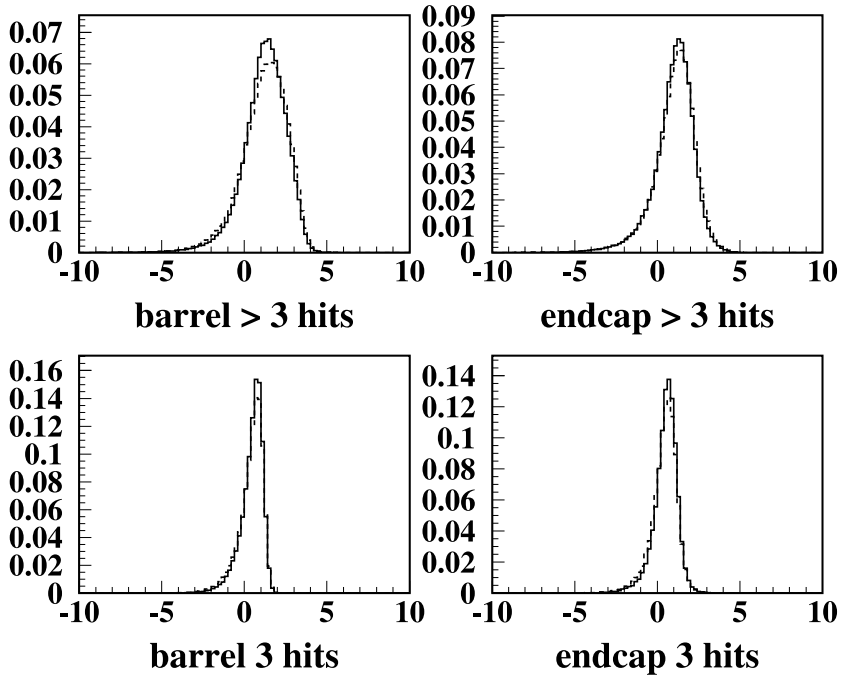

Figure 3.24: DATA-MC comparison of r for good clusters from 7 γ events. The 3 and > 3 hits cases are shown separately.

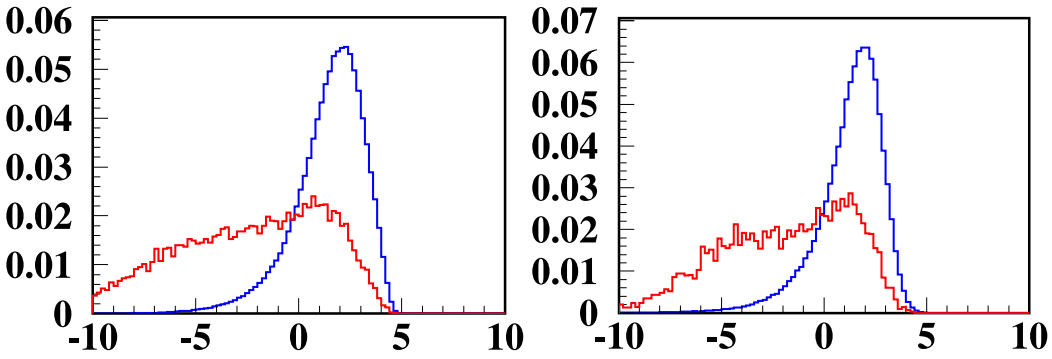

Figure 3.25: r distribution for good clusters (narrow distribution) and for merged clusters (broad distribution) for barrel (left) and endcap (right).

$$S^2(\eta\pi^0) = \frac{(m(\gamma_1\gamma_2) - m(\pi^0))^2}{\sigma^2_{m(\pi^0)}} + \frac{(m(\gamma_3\gamma_4) - m(\eta))^2}{\sigma^2_{m(\eta)}}$$

$$S^2(\omega\pi^0) = \frac{(m(\gamma_1\gamma_2) - m(\pi^0))^2}{\sigma^2_{m(\pi^0)}} + \frac{(m(\gamma_4\gamma_5) - m(\pi^0))^2}{\sigma^2_{m(\pi^0)}} + \frac{(m(\gamma_1\gamma_2\gamma_3) - m(\omega))^2}{\sigma^2_{m(\omega)}}$$

The values of the uncertainties used for these variables are function of the energy and direction of the photons. In our case the angular uncertainity is negligible respect to the energy one. For this reason we neglect the effect of angular uncertainty and we express the error on the mass as a function of the uncertainty on the energy. This expression is very simple, in fact given two photons γ_1 and γ_2 the invariant mass of the pair can be written in the form:

$$m_{\gamma\gamma} = \sqrt{2E_1 \cdot E_2(1 - cos\theta_{12})}$$

and therefore:

$$\frac{\sigma_m}{m} = \frac{1}{2}\sqrt{\left(\frac{\sigma_{E_1}}{E_1}\right)^2 + \left(\frac{\sigma_{E_2}}{E_2}\right)^2}$$

The energy resolution σ_E has been reevaluted. It is not the calorimeter energy resolution, because the kinematic fit improves it. The resolution function has been estimated with Monte Carlo and shown in fig. (3.26).

To check DATA-MC agreement on the S variable, we select two control samples. The $\omega\pi^0$ control sample selected before is used to check $S^2(\pi^0\pi^0)$ and $S^2(\omega\pi^0)$ while a new control sample is defined to check $S^2(\eta\pi^0)$. This control sample is chosen in such a way to enhance the a_0 contribution in the DATA, this is done vetoing all other contributions with the following cuts:

- cluster energy > 50 MeV and angle $> 25°$;
- χ^2 kinematic fit < 20 to reject $\eta \to 3\pi^0$;
- $S^2(\pi^0\pi^0) > 10$ to reject f_0;
- $S^2(\omega\pi^0) > 15$ to reject $\omega\pi^0$
- photon energy < 355 MeV to reject $\eta\gamma$;

The DATA-MC comparison for the three variables is reported in fig. (3.27) where a nice agreement can be seen in both linear and logarithmic scale. In the same figure the expected distribution for the $\eta \to \pi^0\gamma\gamma$ signal is also shown.

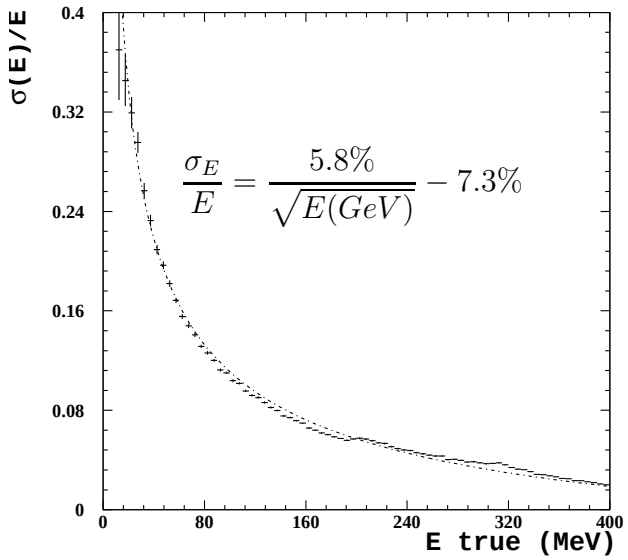

Figure 3.26: Energy resolution after the kinematic fit. The fitted function is reported.

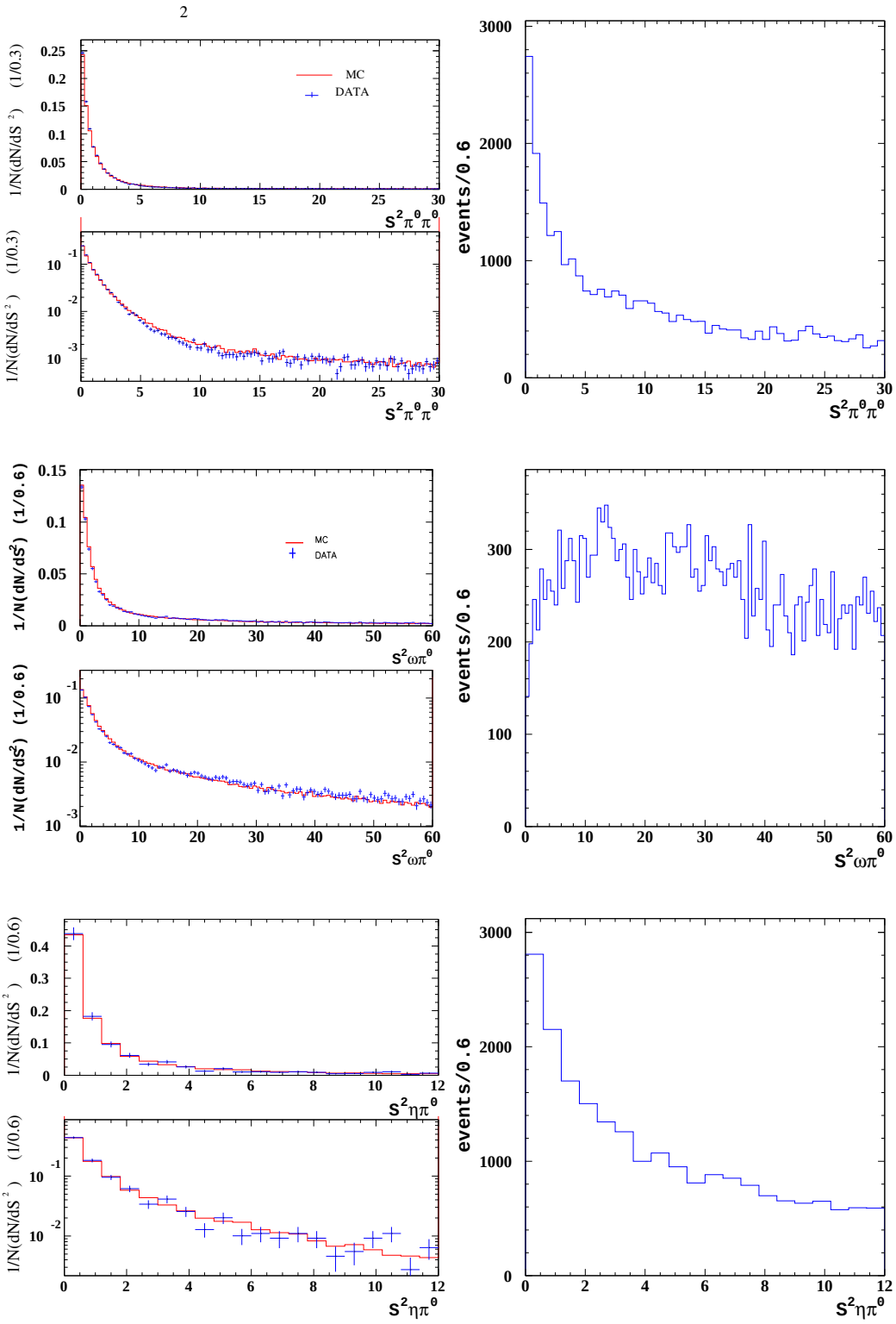

Figure 3.27: DATA-MC comparison for $S^2(\pi^0\pi^0)$, $S^2(\omega\pi^0)$ and $S^2(\eta\pi^0)$: continuos line MC, error bars DATA. The MC distributions for the $\eta \to \pi^0\gamma\gamma$ signal are also shown (right).

Chapter 4

$\eta \rightarrow \pi^0\gamma\gamma$ branching ratio measurement.

In this chapter we give the $Br(\eta \rightarrow \pi^0\gamma\gamma)$ measurement, the cuts on the selection variables described in the previous chapter. The statistical approach used to extract the value is described.

4.1 Preselection.

The analysis has been done in two steps, a preselection and a selection. The preselection selects events with 5 prompt neutral clusters whose total energy is greater than 800 MeV from the FILFO (see sec. 2.6) and EVCL (see sec. 3.3) filtered data. The FILFO background and the EVCL filter efficiency are evaluated at the end of the selection chain just to show that their contribution is negligible.

The FILFO and EVCL algorithm select 59677853 events from about 450 pb^{-1} of DATA. These events are then filtered by the preselection filter whose efficiency and DATA sample size are reported in tab. (4.1).

The DATA sample selected in this way (1917490 events) is reduced to discard noisily runs with bad trigger information and bad ϕ momentum determination. This rejection leaves a DATA sample of 1866231 events.

4.2 Optimization algorithm.

To find the best combination of cuts needed to maximize the analysis sensitivity, an algorithm has been developed that maximize the statistical significance.

Cut	$\epsilon(\eta \to \pi^0\gamma\gamma)$	DATA sample
5 prompt clusters	60.8 ± 0.2 %	3044659
Etot > 800 MeV	93.46 ± 0.13 %	1935296
kinematic fit with π^0 passed	99.65 ± 0.03 %	1917490
Global efficiency - DATA reduction	56.6 ± 0.2 %	3.213 ± 0.002 %

Table 4.1: Efficiency and DATA suppression of the preselection cuts.

If we suppose to have an exact estimate of the background B_{MC} from the MC simulation, and in the data sample there are S signal events we detect $N = S + B_{MC}$, the error on N is $\sqrt{N}$ so that the S estimate and the error on S will be:

$$S = N - B_{MC} \quad \sigma_S = \sqrt{N} \sim \sqrt{S + B_{MC}}$$

therefore the relative error on S will be $\sim \frac{S}{\sqrt{S+B_{MC}}}$.
The significance has been maximized respect to the cuts on the variables using the MC sample. The variables used to select the signal and reject background are described in the previous chapter and are here summarized:

- the minimum energy of the photons after the kinematic fit E_{min};
- the minimum angle of the photons θ_{min};
- the $\chi^2_{\pi^0}$ of the kinematic fit with the π^0 hypothesis;
- the $S^2(\pi^0\pi^0), S^2(\omega\pi^0), S^2(\eta\pi^0)$ as described in sec. (3.10);
- the angle $\theta_{\gamma x}$ and the energy $E_{\gamma x}$ of the lost photon from the output of the kinematic fit in the $\eta \to 3\pi^0$ with 1 lost and 2 merged photons hypothesis (see sec. 3.8);
- the likelihood function for merged cluster identification, as described in sec. (3.9).

To these cuts we add the response of the kinematic fit in the $\eta \to 3\pi^0$ with two lost photons hypothesis, in particular we choose the combination reported in tab. (3.6) right because it has an higher efficiency.

For E_{min} and θ_{min} the optimization algorithm has been forced to scan the region: $E_{min} > 20$ MeV and $\theta_{min} > 21°$, in order to reject accidental background as described in the previous chapter. It confirms these two values

Optimized cut	relative efficiency	DATA selected.
$\theta_\gamma > 21^\circ$	94.07 ± 0.13 %	574474
$E_{min} > 20$ MeV	91.17 ± 0.16 %	286516
2 lost rejection	95.00 ± 0.13 %	246602
$\chi^2_{\pi^0} < 15$ (fig. 3.16)	57.40 ± 0.30 %	128197
$S^2(\omega\pi^0) > 30$ (fig. 3.27)	71.8 ± 0.4 %	34446
$S^2(\pi^0\pi^0) > 7$ (fig. 3.27)	83.4 ± 0.3 %	12157
$S^2(\eta\pi^0) > 8$ (fig. 3.27)	62.4 ± 0.5 %	4422
$16^\circ < \theta_{\gamma x} < 164^\circ$ (fig. 3.23)	97.7 ± 0.2 %	4136
$E_{\gamma x} < 76$ MeV (fig. 3.23)	92.0 ± 0.4 %	3550
Likelihood (fig. 3.25) r < -0.5 barrel, $< 0.$ end-caps	53.7 ± 0.7 %	1034
EVCL	98.92 ± 0.19 %	
Global efficiency (data suppression)	4.72 ± 0.08 %	$(1.73 \pm 0.05) \times 10^{-5}$

Table 4.2: Optimized cuts, efficiency and data sample rejection factor. The FILFO and Trigger efficiency is 100 %

as optimum values.

After these cuts the efficiency is 4.72 % while we have 1034 events in the DATA sample. The expected background composition as estimated by MC is reported in tab. (4.3). In the same table we show the expected number of events obtained using the correction factor of tab. (3.5).
As we will show after, the discrepancy between DATA and MC expected is not due to the signal presence, this is a common problem of rare decay search, even if the DATA and MC distribution agree very well also in the tail (has we have seen in the previous chapter), the background that is suppressed with a huge factor $\sim 1.73 \times 10^{-5}$ is hardly reproduced by the MC simulation. For this reason we prefer not to use an absolute subtraction procedure, but to fit a distribution in which the MC and background look very different.
To identify the signal we proceed in the following way:

- we identify the photon γ_ϕ originated in the ϕ decay among the 5 γ of the $\phi \to \eta(\to \pi^0\gamma\gamma)\gamma_\phi$ process in the following way. Looking at the inclusive distribution of the 5 γ's energy shown in fig. (3.6), it can be seen that the energy of the main part of photons is below the γ_ϕ peak at 363 MeV. So γ_ϕ is simply identified as the most energetic photon.

- we build the invariant mass $m(4\gamma)$ of the remaining 4 photons. It peaks

Background channel	N. events	N. events corrected
$\omega\pi^0$	709	99.83
f_0	265	56.71
a_0	361	49.46
$\rho\pi^0$	203	18.27
η 2 merged	119	70.21
η 1 lost 1 merged	624	187.2
η 2 lost	1065	160.82
Total	3346	642

Table 4.3: Background expected from MC, with and without correction of tab. (3.5).

at the η mass in the signal case.

In fig. (4.1) we show the $m(4\gamma)$ distribution for both signal and weighted background.

The number of signal events is extracted by fitting the 2 MC distributions for signal and background to the DATA distribution with the method described in the following section.

4.3 Maximum likelihood fit with finite Monte Carlo statistic.

The fit has been performed using the HMCMLL routine of the HBOOK package [44]. It is useful when one has a small number of events in some of the DATA histogram bins and a small number of events in the MC simulated distribution. The problem is described and the solutions shown in the following.

We want to determine the contents of two samples in our DATA distribution starting from several (2 in our case) MC predicted distributions. Let's suppose that the MC distribution has a very large number of events N_J and let's call with P_j $(j = 1, 2, ..., m)$ the fraction of the sample j in our data. The prediction f_i for the number of events in the bin i of the DATA histogram is given by:

$$f_i = N_D \sum_{j=1}^{m} P_j a_{ji}/N_J$$

where a_{ji} is the number of events that are in the bin i of the histogram of

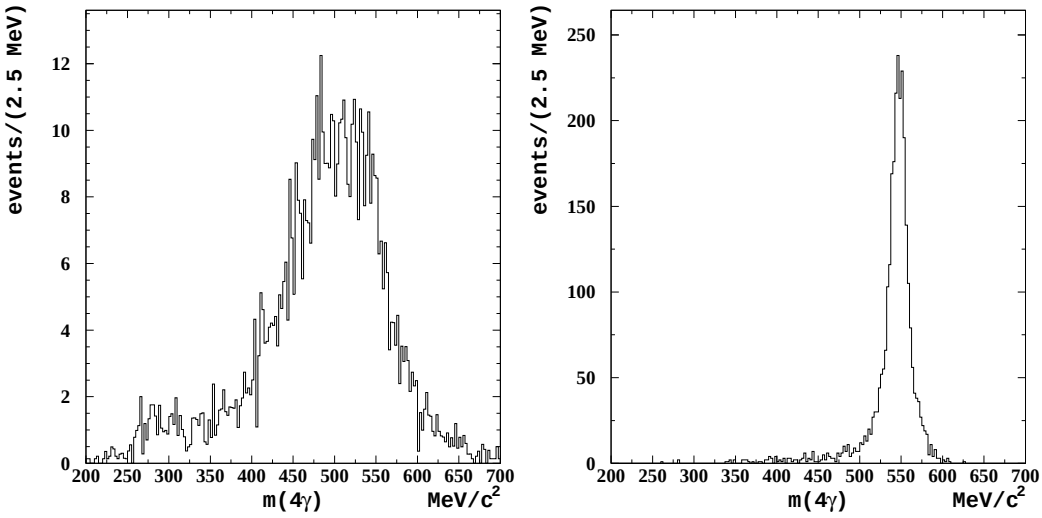

Figure 4.1: Monte Carlo distribution of $m(4\gamma)$ for background (left) and signal (right).

the source j. Being N_J very large the fluctuations on the numbers a_{ji} are very small and as a consequence a_{ji} is very close to its true value. Let's call this value A_{ji}.
If N_J is not so large the correct expression to use is:

$$f_i = N_D \sum_{j=1}^{m} P_j A_{ji}/N_J$$

The quantities A_{ji} are the expected values for a_{ji} and are unknown, while N_D is the number of events in the DATA histogram. The values a_{ji} are distributed according a binomial distribution in each bin i. In the limit in which $A_{ji} << N_J$, that is the histogram has many bins, the a_{ji} distribution can be well approximated by a Poisson distribution with mean A_{ji}.
For what concern the DATA histogram, the content of the i bin, d_i, is distributed according a Poisson distribution with mean f_i. Then we can build a joint probability to find a value d_i for the content of the i bin of the DATA histogram, whose expected value is f_i, and to find a value a_{ji}, whose expected value is A_{ji}, for the content of the bin i of the source j histogram. In practice we must maximize the following function:

$$\mathcal{L} = \prod_i e^{-f_i} \frac{f_i^{d_i}}{d_i!} \times \prod_{ij} e^{-A_{ij}} \frac{A_{ij}^{a_{ij}}}{a_{ij!}}$$

This distribution is maximized respect to the fraction P_j and the quantity

A_{ji}. Of course we are interested only to the P_j quantities.

To simplify the calculation it is better to maximize $ln\mathcal{L}$ that is:

$$ln\mathcal{L} = \sum_{i=1}^{nbin} d_i ln f_i - f_i + \sum_{j=1}^{n.sources} a_{ji} ln A_{ji} - A_{ji}$$

The values $ln(d_i!)$ and $ln(a_{ij}!)$ are constant quantities that don't enter in the maximization.

4.3.1 Weighted distributions.

In our case the MC background distribution comes from weighted events. Each event k is weighted with a factor l_k of tab. (3.5) according to the background channel it belongs to. For this reason in each bin i we have different weighted events. The MC spectrum is obtained by weighting each i bin of the unweighted MC histogram with a weight w_i obtained averaging the weights l_k of the events entering the bin i.
The only difference respect to the previous considerations is in f_i definition:

$$f_i = N_D \sum_{j=1}^{m} P_j w_{ji} A_{ji} / N_J$$

4.4 The fit.

In fig. (4.2) we show the MC distributions used in the fit. The unweighted background distribution together with the weights evaluated for each bin, the MC weighted distribution and the signal distribution.
As can be seen in the figure the $m(4\gamma)$ spectrum has been cut in the range 426 - 612 MeV/c^2 to exclude very low populated bins. The chosen bin width is 6 MeV.

The fit result for the background and signal fractions is:

$$\text{P(background)} = 0.907 \pm 0.049 \qquad \text{P(signal)} = 0.093 \pm 0.031$$

and the covariance matrix is:

$$\begin{pmatrix} 2.41 \cdot 10^{-3} & -0.847 \cdot 10^{-3} \\ -0.847 \cdot 10^{-3} & 0.984 \cdot 10^{-3} \end{pmatrix}$$

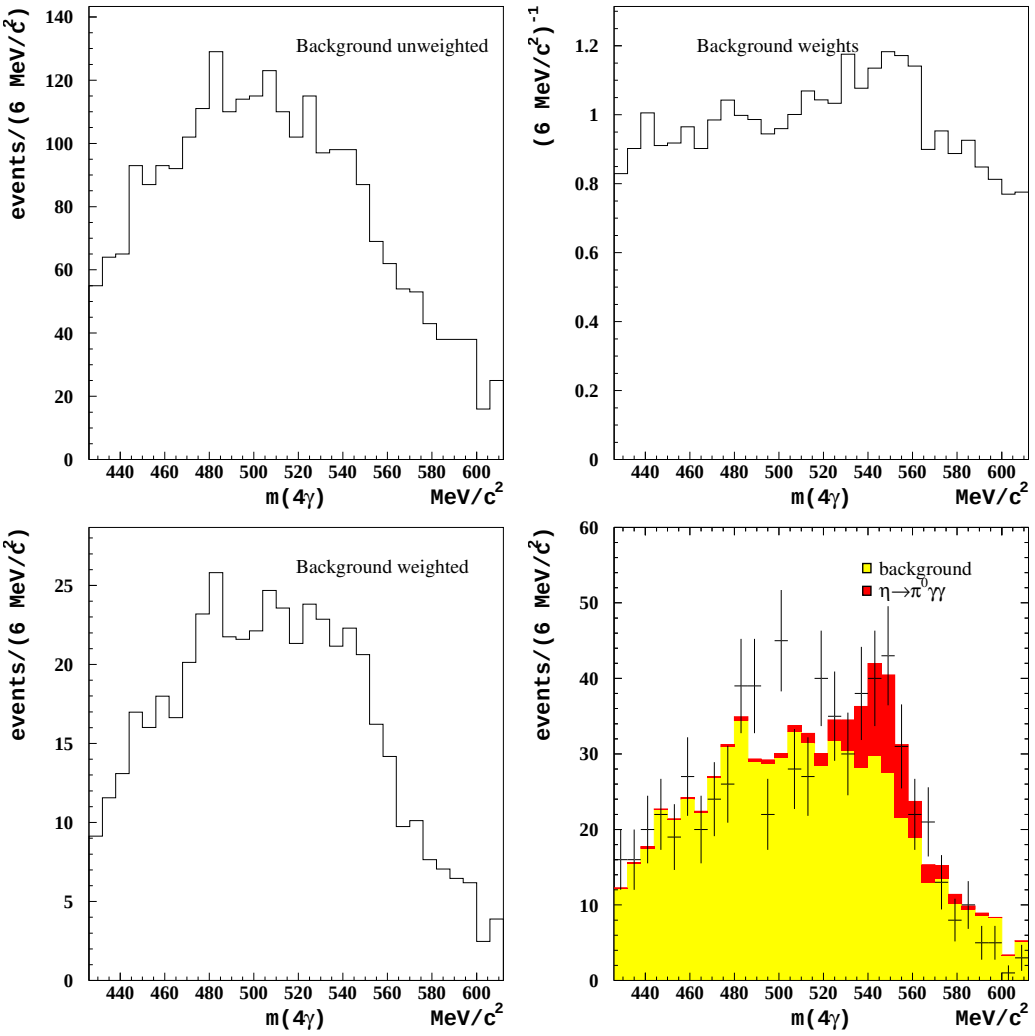

Figure 4.2: MC distribution used to fit the DATA: (top) background unweighted together with the weights, (bottom) MC weighted with the signal.

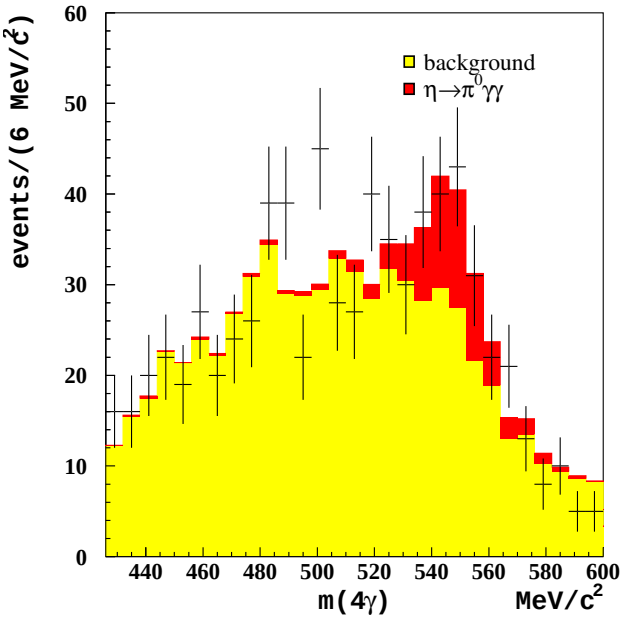

Figure 4.3: 4γ invariant mass DATA distribution fitted with MC shapes.

The DATA distribution fitted together with the MC background and signal is shown in fig. (4.3). To show the significance of the signal fraction we have reported in fig. (4.4) the 68.27 %, 90 %, 95 % and 99 % confidence region in the background-signal fraction plane. The signal presence is significant at about 99 %

Taking into account the 426 - 612 MeV/c^2 window the signal efficiency is 4.63 ± 0.09 % and the DATA sample is of 735 events. So we obtain the following numbers for background and signal events.

$$N_{background} = 667 \pm 36 \qquad N_{sig} = 68 \pm 23$$

To extract the branching ratio we have measured the number of $\eta \to 3\pi^0$ with a dedicated selection made selecting events in this way:

- FILFO and EVCL passed;
- seven prompt calorimeter clusters not associated to a charged track, with an angle $> 23°$ and energy > 20 MeV;
- at least a cluster with energy greater then 280 MeV.

The number of selected events in the same DATA sample is $N(\eta \to 3\pi^0) = 2288882$ while the efficiency is $\epsilon(\eta \to 3\pi^0) = 0.378 \pm 0.008(syst) \pm 0.001(stat.)$,

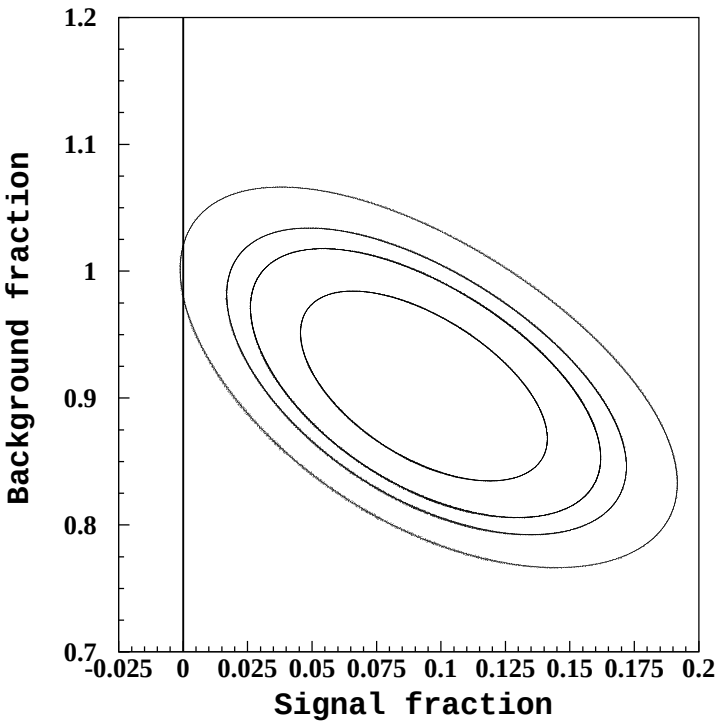

Figure 4.4: 68.27 %, 90 %, 95 % and 99 % countours of the fit.

so we get the following result for $\eta \to \pi^0\gamma\gamma$ branching ratio:

$$\frac{Br(\eta \to \pi^0\gamma\gamma)}{Br(\eta \to 3\pi^0)} = \frac{N(\eta \to \pi^0\gamma\gamma) \cdot \epsilon(\eta \to 3\pi^0)}{N(\eta \to 3\pi^0) \cdot \epsilon(\eta \to \pi^0\gamma\gamma)} = (2.43 \pm 0.82) \times 10^{-4}$$

That taking into account that $Br(\eta \to 3\pi^0) = 32.51 \pm 0.29$ % we obtain:

$$Br(\eta \to \pi^0\gamma\gamma) = (8.0 \pm 2.7) \times 10^{-5}$$

4.5 Systematic studies.

The systematic due to DATA-MC discrepancies in the shape of the $M_{4\gamma}$ distribution of the signal and of the background has been studied by varying the bin width of the histograms used in the fit and the window chosen to fit the histograms.

4.5.1 Systematic due to the bin width choice.

The bin width has been varied between 2 MeV and 9 MeV, the fit has been done for each value of this bin width leaving the fitted region at [426 - 612] MeV.
For each bin width the fractions of background and signal have been refitted, the branching ratio has been reevaluated and reported in fig. (4.5). The maximum excursion among the values is 0.52×10^{-5}. The chosen bin width gives the maximum value, so to symmetrize the error we correct the branching ratio value for 1/2 of the excursion and give 1/2 of it as systematic error, that is the central value is 7.70×10^{-5} while the systemetic error due to the bin choice is 0.26×10^{-5}.

4.5.2 Systematic due to the window chosen to fit $m_{4\gamma}$ distribution.

To check the stability of the fit to the choice of the window used to extract the branching ratio we have varied the lower cut in the range 378 - 474 MeV and the higher cut in the range 570 - 720 MeV, the bin width has been fixed to 6 MeV.
In fig. (4.6) we have reported the branching ratio as a function of the lower mass cut (left) and of the higher mass cut (right). The systematic error coming from these variation is taken as 1/2 of the maximum variation and they are 0.44×10^{-5} for the lower cut and 0.56×10^{-5} for the higher cut.

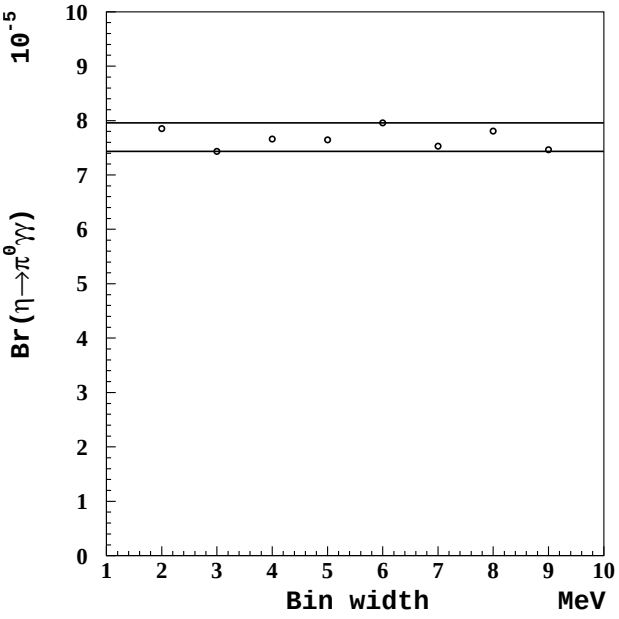

Figure 4.5: Branching ratio obtained with different choices of the bin width. The two horizontal line indicate the maximum and minimum value obtained.

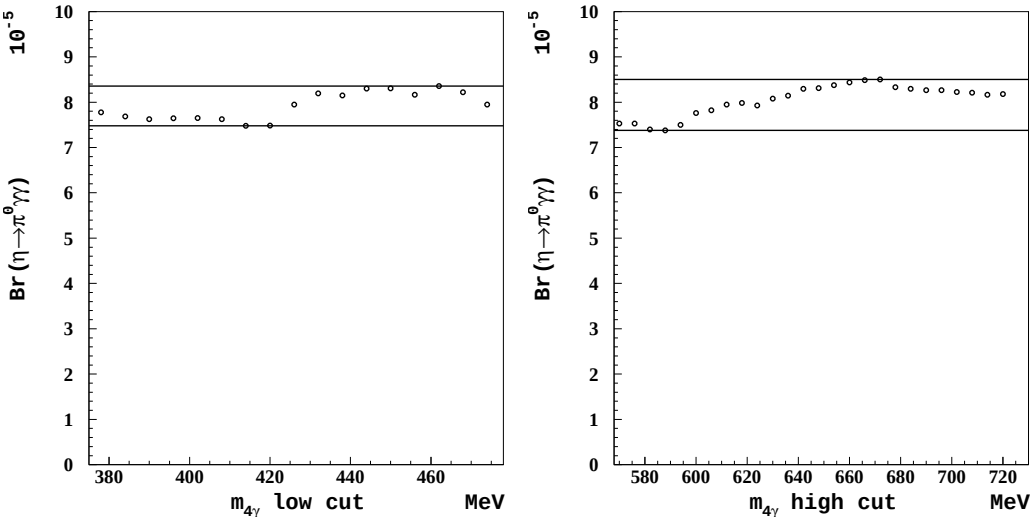

Figure 4.6: Branching ratio obtained for different choices of: (left) lower value of $m_{4\gamma}$, (right) higher value of $m_{4\gamma}$.

Source of systematic error	variation range	error
Bin width	2 - 9 MeV	0.26×10^{-5}
Lower cut on $m_{4\gamma}$	378 - 474 MeV	0.44×10^{-5}
Higher cut on $m_{4\gamma}$	570 - 720 MeV	0.56×10^{-5}
Overall systematic error		0.8×10^{-5}

Table 4.4: Systematic error summary.

The systematic error are resumed in tab. (4.4), the overall systematic error is obtained by summing in quadrature the three contributions.

The final result taking into account the considerations on the systematic is:

$$Br(\eta \to \pi^0\gamma\gamma) = (7.7 \pm 2.7_{(stat.)} \pm 0.8_{(syst.)}) \times 10^{-5}$$

4.6 Comparison with previous results.

In fig. (4.7) we compare the previous experimental results with the Branching ratio measured here. This result is discrepant with the GAMS value and is marginally in agreement with Crystal Ball.
In fig. (4.8) we report the KLOE measured value with several theoretical predictions.

As we can see all the predictions are quite high, the old theoretical estimate of ChPT at $O(p^6)$ with vector resonance saturation is in good agreement with the present result. So this result seems to confirm that the $\eta \to \pi^0\gamma\gamma$ is well understood at $O(p^6)$. The NJL estimate of p^6 contribution is in agreement as well, while the inclusion of scalar meson contribution (a_0) such as in the $ENJL$ model gives too high values.
The pure VMD estimate and the all order estimates give a too high value.
As we have seen in chapter 1 the p^2 contribution vanishes while the p^4 contribution is suppressed by G-parity violation and the kaon mass in the propagator. So one expects that the main contribution to the $\eta \to \pi^0\gamma\gamma$ comes from $O(p^6)$ terms. The all order estimate give a value that is at least double of $O(p^6)$. This is quite strange, in fact no reason for such high contribution has been found. If this was the case the coefficient of higher order operators would be unnaturally high and this would be a trouble for a perturbation theory.

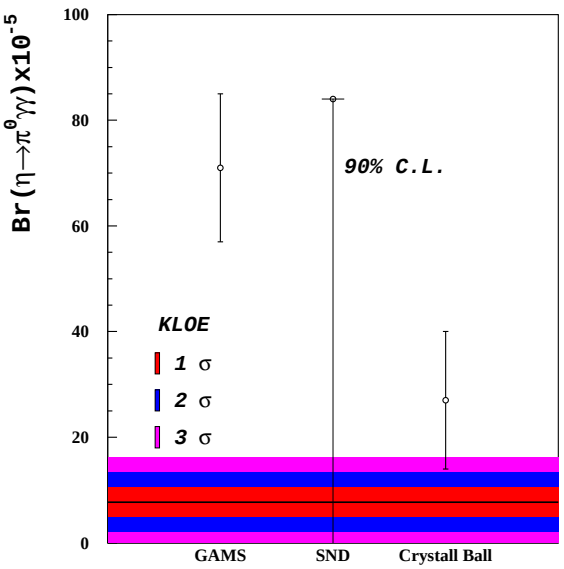

Figure 4.7: Previous branching ratio measurements. The KLOE 68%, 90% and 98% regions are shown.

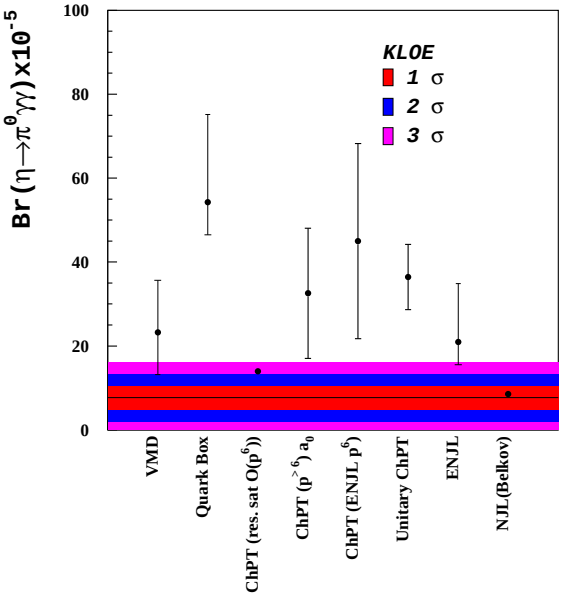

Figure 4.8: Theoretical predictions for $Br(\eta \to \pi^0\gamma\gamma)$ compared with this measurement. For the references see tab. (1.1).

Chapter 5

Upper limit on the $\eta \to \gamma\gamma\gamma$ decay.

In this chapter we describe the analysis performed to search for the C-violating decay $\eta \to \gamma\gamma\gamma$ in the data collected in the years 2001 and 2002. The signal is searched in events with 4 photons in the final state. The spectrum of the most energetic photon is used to search for the signal. The background is evaluated from data itself.

5.1 Introduction

The η meson is an even eigenstate of the charge coniugation operator C (see sec. 1.9), while a photon is an odd C eigenstate. So any decay of the η meson into a final state with an odd number of photons violates the C symmetry. In the Standard Model, the C symmetry is exactly conserved in both strong and electromagnetic decays, but it is violated in weak decays due to the V-A structure of the weak couplings. In the framework of the Standard Model the decay rate of the $\pi^0 \to 3\gamma$ has been evaluated [45], and generalizing this result to the η meson [46], one obtains $\mathrm{Br}(\eta \to 3\gamma) < 10^{-12}$.
For this reason the discovery of a larger decay rate would be a clear signal of SM violation. At the moment all predictions of alternative models are far below the experimentally achievable limits [47]. From the experimental point of view the only published result is that of the GAMS2000 experiment, which has obtained the upper limit 5×10^{-4} at 90 % C.L. [8].

5.2 Background

The signal in this analysis is $\phi \to \gamma\eta(\to 3\gamma) \to 4\gamma$, the cross section corresponding to the GAMS upper limit is very low: < 0.02 nb, calculated taking σ_ϕ=3.1 μb. So, background studies have to cover all possible neutral processes. Relevant physical processes which give 4 photons in the final state include $e^+e^- \to \omega\gamma$ with $\omega \to \pi^0\gamma$ but also more important are processes with less or more than 4 photons due to background which mimic 4 photons events. The agreement with MC in the background description is very hard to obtain due to the effects themselves that induce background: cluster splitting, cluster merging, accidental cluster due to machine background. These effects are very difficult to reproduce, so in this case we have estimated the background directly from data and used the MC only to evaluate the detection efficiency of the signal.

5.3 Preselection

The selection criteria are based on a sample of 120000 Monte Carlo $\phi \to \gamma\eta$, $\eta \to \gamma\gamma\gamma$ events where the η meson decay is described by pure phase space (since its matrix element is unknown).

To the events is applied a 'recovery splitting' procedure (applied both to data and MC). To suppress split clusters, it is required that every cluster don't have an association with a DC track.
The preselection criteria are described here:

1. We require 4 prompt clusters in the calorimeter (see sec. 3.2 for the prompt cluster definition). Photons of a signal event come from the I.P.(interaction piont), must have t-r/c within a time window of 5 times the calorimeter time resolution σ_t, see tab. (5.1) for the time resolution used.

2. We require 4 "good" photons. Where a good photon is defined in the following way: the cluster energy is greater than 30 MeV, the angle respect the beam line is such that $|cos\theta| < 0.93$. Cluster energy cut rejects fake clusters and split clusters, the polar angle interval 21.6°-158.4° excludes the blind region around the beam-pipe where a lot of machine background and bhabha background is present.

3. We require that the total energy of prompt clusters be greater than 800 MeV and the total momentum of prompt clusters $<$ 200 MeV to

reject kaons and charged events background. These last two cuts , as in the $\eta \to \pi^0\gamma\gamma$ case, reject multi photons events with a number of photons greater than 4, which give background if some photons are lost.

At the end of the preselection we have 71865 preselected events in 2001 data and 118180 in 2002 data.

5.4 Selection

The events that pass the preselection are stored and to them are applied the following additional cuts:

1. $\theta_{\gamma\gamma}$>15°, $\theta_{\gamma\gamma}$ is the minimum angle between two photons, to further reject split clusters, which mainly come from 3γ final states.
   Fig. (5.1) shows the distribution of the minimum angle between two photons for $\phi \to \pi^0\gamma \to 3\gamma$, $\phi \to \eta(\to \gamma\gamma)\gamma \to 3\gamma$, $\phi \to \eta(\to 3\gamma)\gamma \to 4\gamma$ final states (the distributions are taken from Monte Carlo without accidental cluster simulation) and 2001 data. The peak around 10° in the data distribution is clearly due to residual split clusters.

2. $E_{min} > 50$ MeV, $|cos\theta| < 0.91$; these cuts further reject accidental clusters and QED background, see fig. (5.2) and fig. (5.3).

5.4.1 Kinematic fit procedure

At this point a kinematic fit procedure is applied to the four photons to improve the energy resolution. The input variables of the fit are the following:

- X,Y,Z coordinates of the cluster;
- E energy of the cluster;
- t time of the cluster;
- X,Y,Z of the interaction vertex (only data, 0 0 0 for MC);
- E,Px,Py,Pz of the ϕ (obtained run by run from bhabha analysis for DATA, (1019.413, -12.7,0.,0.) MeV for MC);

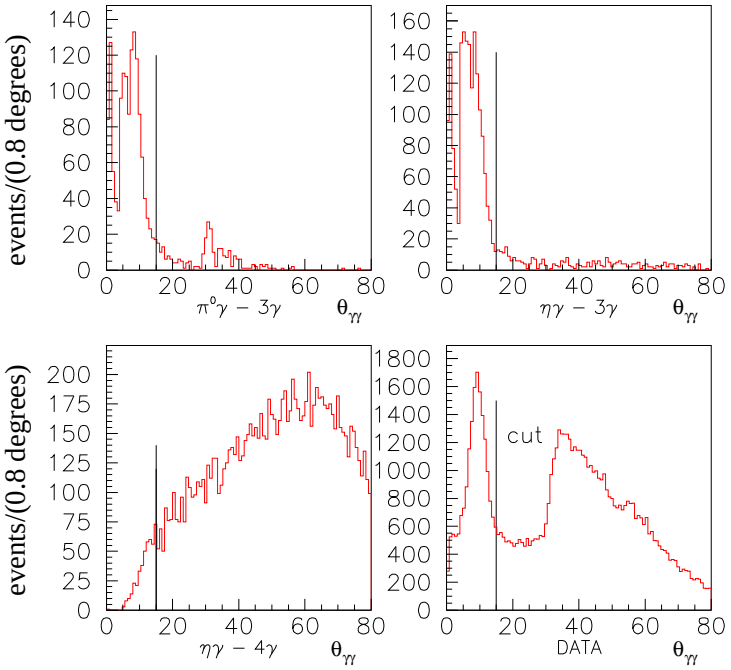

Figure 5.1: $\theta_{\gamma\gamma}$ for the following samples: MC $\pi^0\gamma \to 3\gamma$, MC $\eta\gamma \to 3\gamma$, MC Signal $\eta \to 3\gamma$, 2001 DATA.

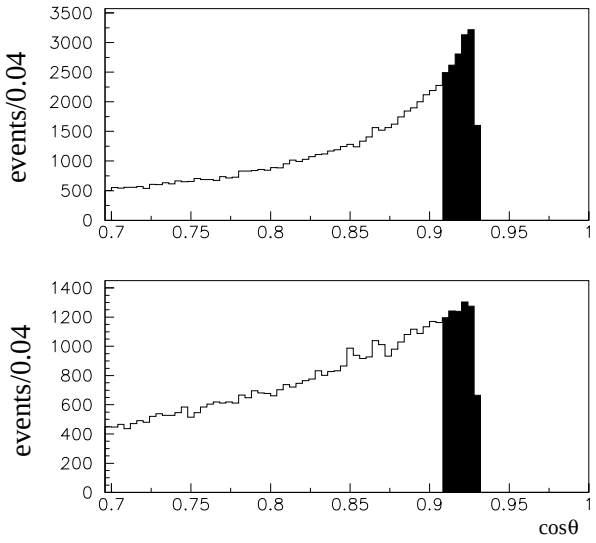

Figure 5.2: *cosθ* distribution for: **up** 2001 DATA, **down** MC signal.

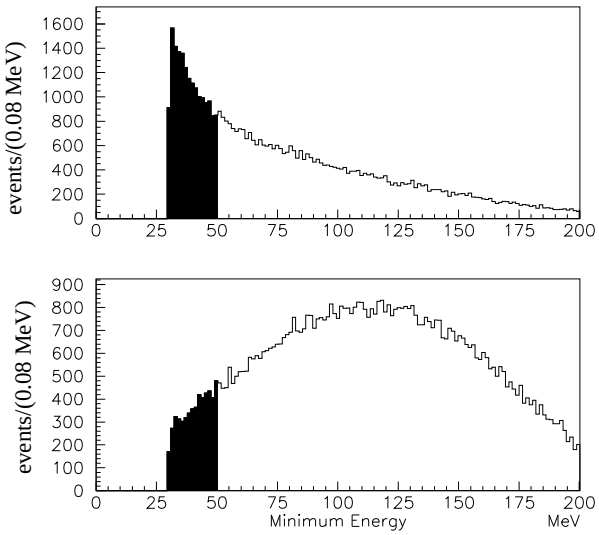

Figure 5.3: Minimum energy of the four photons for: **up** 2001 DATA, **down** MC signal

The fit is made according to the Lagrange's multipliers method, minimizing the following χ^2:

$$\chi^2 = \sum_i \frac{(x_i - \mu_i)^2}{\sigma_i^2} + \sum_j \lambda_j F_j(\mu_k) \tag{5.1}$$

with 27 free parameters where the $F_j(\mu_k)$ represent the energy, momentum and time constraints.
The errors used for the fitted variables, different for DATA and Monte Carlo, are reported in tab. (5.1). The χ^2 of the kinematic fit is used to reject background using the cut $\chi^2_{min} > 25$ (see fig. 5.4). At this point the main source of background is given by the channel $e^+e^- \to \omega(\to \pi^0\gamma)\gamma$ where a photon comes from initial state radiation. To see it, we procede in the following way. First we do a kinematic fit with the hypothesis of a $\pi^0\gamma\gamma$ final state, choose the combination with the mimimum χ^2, then we plot the variable $m_{\pi^0\gamma}$, choosing the most energetic photon between the two photons that aren't linked to the π^0 (see fig. 5.5).
Events with a π^0 in the final state are a very large fraction of background, they come also from $\phi \to f_0\gamma \to \pi^0\pi^0\gamma$, $\phi \to a_0\gamma \to \eta\pi^0\gamma$ and $\phi \to \pi^0\gamma$ final states. So we reject events containing a π^0 by cutting on the invariant mass built from any couple of photons, $m_{\gamma\gamma}$. This variable is plotted in fig. (5.6) both for 2001 DATA and MC signal. The cut chosen is 90 MeV/$c^2 < m_{\gamma\gamma} <$ 180 MeV/c^2.

Variable	σ_{MC}	σ_{DATA}
E	$\left(0.05/\sqrt{\text{E (GeV)}}\right) \cdot E$	$\left(0.057/\sqrt{E(\text{GeV})} + 0.006\right) \cdot E$
X	1.2 cm	1.2 cm
Y (barrel) Z (end-cap)	1.2 cm	1.2 cm
Z (barrel) Y (end-cap)	$\frac{0.85\text{cm}}{\sqrt{E}(\text{GeV})}$	$\frac{1.4cm}{\sqrt{E}\ (\text{GeV})}$
t	$0.05/\sqrt{E\ (\text{GeV})}$ ps	$\sqrt{(0.15)^2 + \frac{(0.054)^2}{E\ (\text{GeV})}}$ ps

Table 5.1: Resolutions used in the kinematic fit

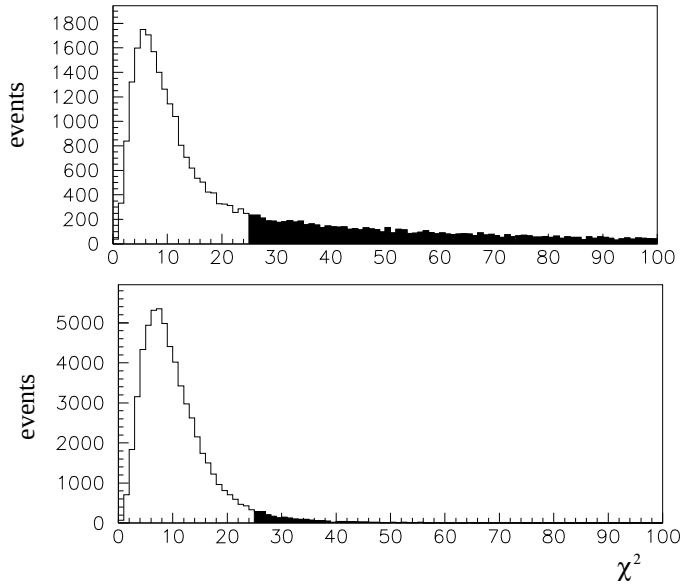

Figure 5.4: χ^2 of kinematic fit distribution for: **up** DATA, **down** MC signal. Events with $\chi^2 > 25$ are rejected.

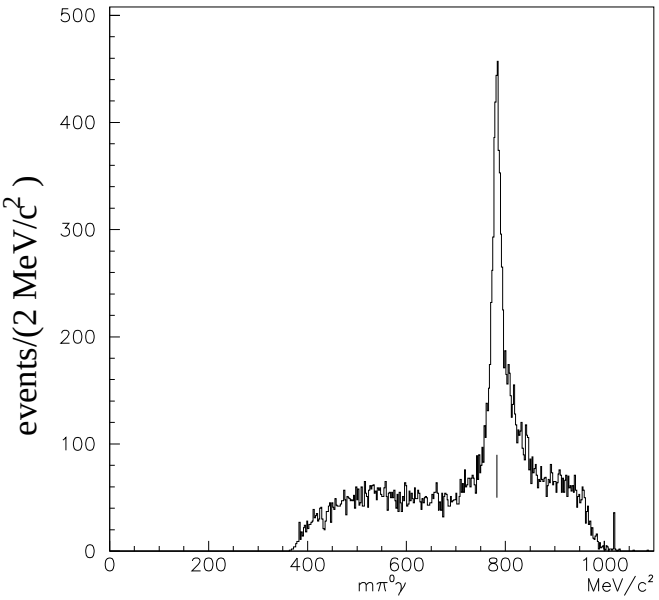

Figure 5.5: $m_{\pi^0\gamma}$ distribution, a clear peak is visible around the ω mass.

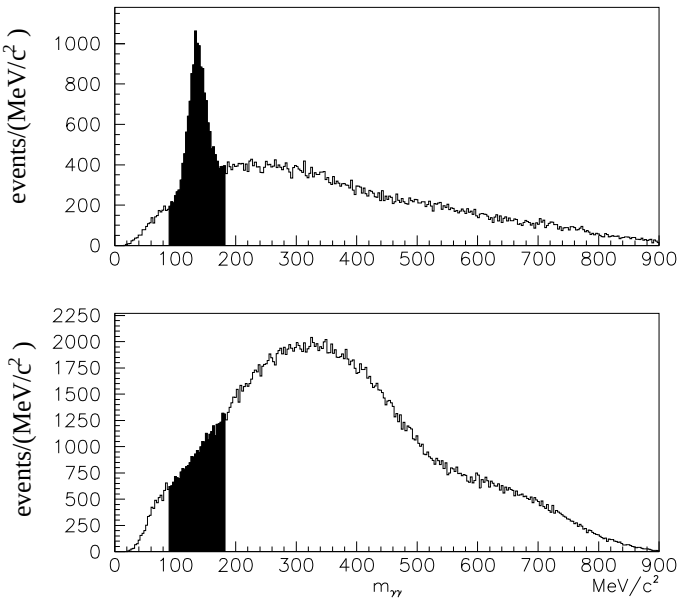

Figure 5.6: $m_{\gamma\gamma}$ distribution for: **up** 2001 DATA, **down** MC signal. Events in the 90 - 180 MeV mass window are rejected.

5.5 DATA - MC comparison on $m_{\gamma\gamma}$

To test the agreement of the data with MC distribution, we have chosen two samples of events, one with 3γ final state and one with 7γ final state. The two samples are: $\phi \to \pi^0\gamma$ and $\phi \to \eta\gamma \to 3\pi^0\gamma$. In fig. (5.7) and fig. (5.8) $m_{\gamma\gamma}$ is shown for DATA and MC. A small discrepancy can be seen for both samples. The discrepancy reflects the difference between MC and DATA energy resolution, well known for the old MC generator. To demonstrate this, we have smeared the energy of every photon with a gaussian distribution whose sigma is: $\sigma_{smear} = \sqrt{\sigma^2_{DATA} - \sigma^2_{MC}}$ and rebuilt the $m_{\gamma\gamma}$ variable. The result is in the lower plots, which show a better agreement. Therefore to evalutate the efficiency of the cut we have used the smeared data.

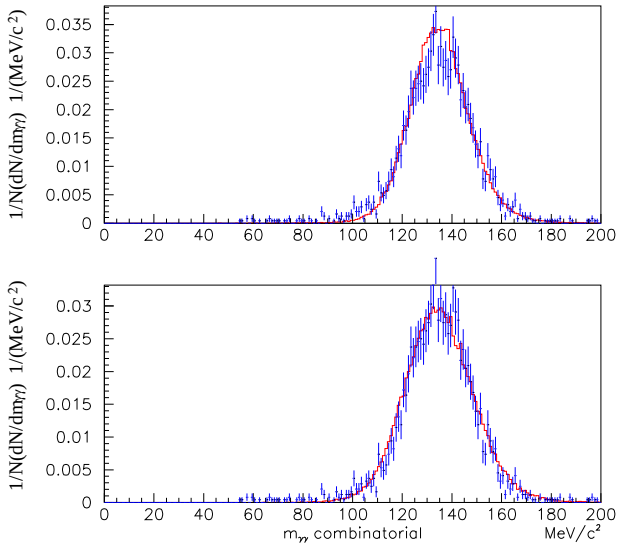

Figure 5.7: $m_{\gamma\gamma}$ distribution for $\phi \to \pi^0\gamma$ sample, the solid line is the MC distribution while the points are 2001 DATA, the two distributions are normalized in the range shown in the plot. Up: unsmeared distribution, down: smeared distribution (MC only)

5.6 Spectrum of the most energetic photon

To search for $\eta \to 3\gamma$ events, we look for a peak in the distribution of the energy E_{max} of the most energetic photon evaluated in the ϕ reference frame. This is the recoil photon of the $\phi \to \eta\gamma$ decay for the majority of the events.

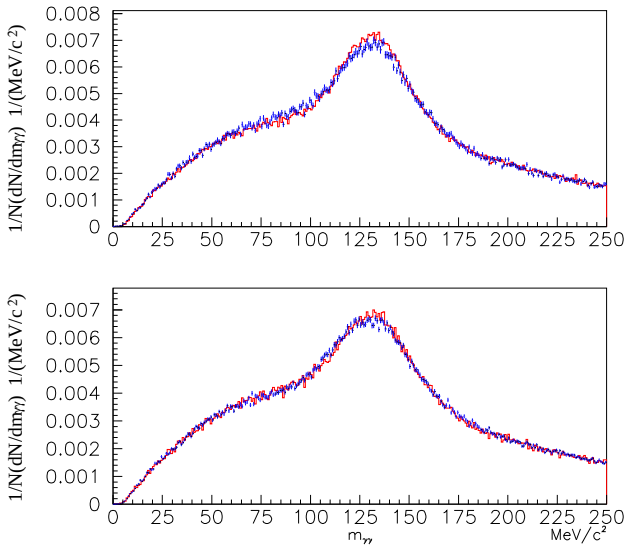

Figure 5.8: $m_{\gamma\gamma}$ distribution for $\phi \to \eta\gamma \to 3\pi^0\gamma$ sample, the solid line is the MC distribution while the points are 2001 DATA, the two distributions are normalized in the range shown in the plot. Up: unsmeared distribution, down: smeared distribution (MC only)

Its energy is 362.7 MeV. In fig. (5.9) the distribution for MC, 2001 and 2002 DATA is shown. The two distributions for 2001 and 2002 overlap very well. A Kolmogorov test gives a compatibility probability of 26%, so we use the whole sample. From the distribution is clear that there isn't a narrow peak in E_{max}, so we don't see any evidence of $\eta \to 3\gamma$ events. For this reason we evaluate an upper limit on the Br($\eta \to 3\gamma$) using this distribution.

5.7 Upper limit evaluation

To evaluate the upper limit we proceed in the following way. We choose as signal region (the region where there is the main part of the signal) the range [350,379.75] MeV (17 bins, 1.75 MeV wide). We assume that there isn't a signal out of this range or it is negligible and doesn't affect the shape of the background distribution. Then we fit the distribution of the DATA in the domain [280,350] MeV $\cup$ [379.75,481.25] MeV with a fifth degree polynomial. The fit is good (χ^2/n.d.o.f = 78/92); the fitted parameters are reported in tab.(5.2) and fig. (5.10). We use the result to obtain the expected number

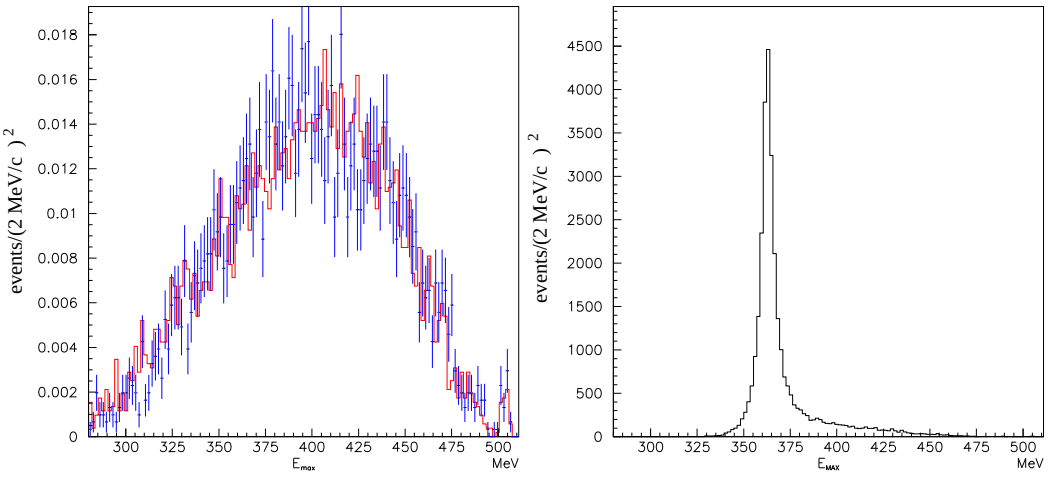

Figure 5.9: Energy of the most energetic photon in the ϕ reference frame: **left:** 2002 DATA (continuous line), 2001 DATA (dot); **right:** MC signal $\eta \to 3\gamma$

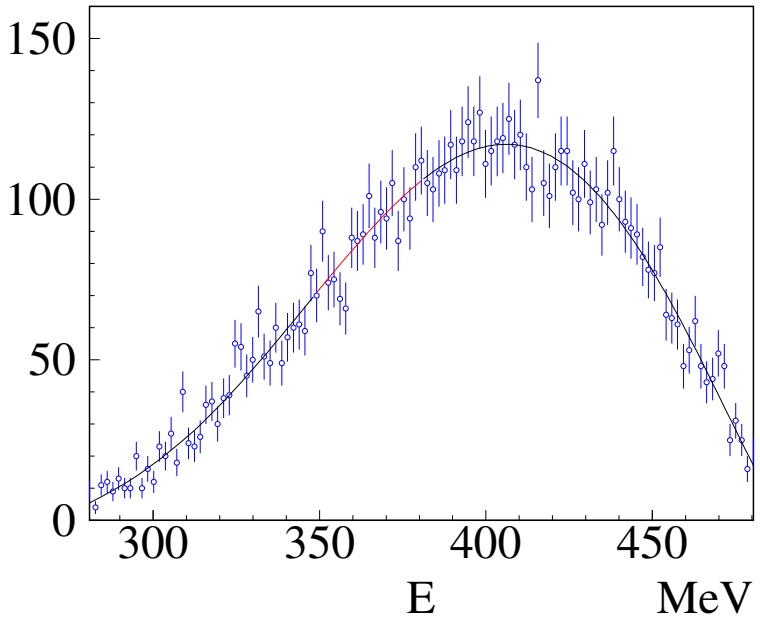

Figure 5.10: E_{max} distribution for 2001+2002 DATA, the interval used for background estimation is shown.

Parameter	Value		
a_1	-8636	$\pm$	5
a_2	278.592	$\pm$	0.019
a_3	-1.64141	$\pm$	0.00005
a_4	$4.74211 \cdot 10^{-3}$	$\pm$	$0.00013 \cdot 10^{-3}$
a_5	$-6.6872 \cdot 10^{-6}$	$\pm$	$0.0003 \cdot 10^{-6}$
a_6	$3.6756 \cdot 10^{-9}$	$\pm$	$0.0005 \cdot 10^{-9}$
χ^2/n.d.o.f = 78/92	$Prob(\chi^2 > 78) = 85\%$		

Table 5.2: Fitted parameters with errors and χ^2 of the fifth degree polynomial fit:$Pol(x) = a_1 + a_2 \cdot x + a_3 \cdot x^2 + a_4 \cdot x^3 + a_5 \cdot x^4 + a_6 \cdot x^5$

of background events in each bin, N_i^b in the signal region [350,379.75].

$$N_i^b = a_1 + a_2 \cdot x_i + a_3 \cdot x_i^2 + a_4 \cdot x_i^3 + a_5 \cdot x_i^4 + a_6 \cdot x_i^5$$

The total number of observed events in the signal window is 1513 while from integration of the polynomial we obtain 1518 events in the same region.

In this range we assume to have both background and signal and build a χ^2 function in this way:

$$F = \sum_i \frac{(N_i - N_i^b)^2}{N_i^b},$$

where N_i is the number of observed counts in the i^{th} bin, and the sum is over bins in the signal region.
To extract an upper limit we use the Neyman's construction procedure [48]. We obtain the distribution function for F for various values of the number of signal counts s as follows. First, we *construct* the values N_i by sampling a Poisson distribution with mean $\langle N_i(s) \rangle = N_i^b + s \times f_i$, where f_i is the fraction of signal events ($\sum_i f_i = 1$, see fig. 5.9, left) in the i^{th} bin, and evaluate F. Repeating this procedure 10^6 times for each value of s we obtain the complete p.d.f., which is numerically integrated to obtain the 90% and 95% contours in Neyman's construction. These countours are shown in fig. (5.11). We then evaluate F using the *observed* N_i. We find $F = 13.45$, from which we obtain

$$N_{\eta \to 3\gamma} \leq 63.1 \text{ @ } 90\% \text{ C.L.} \quad \leq 80.8 \text{ @ } 95\% \text{ C.L.}$$

5.8 Selection efficiency

Here we report the summary of the efficiency for all the cuts.

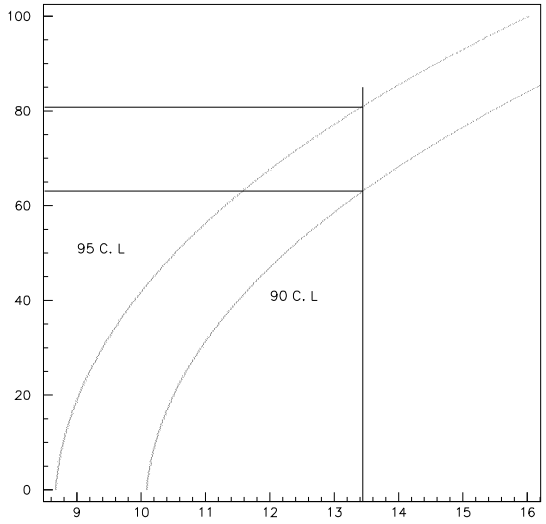

Figure 5.11: 90% and 95% CL upper limits on signal count. The observed value of F is indicated.

Selection cut (filter)	MC events	ϵ_r^*
FILFO	113775/120000	0.9481 ± 0.0006
EVCL	95307/113775	0.8377 ± 0.0011
Ntime = 4	84665/95307	0.88340 ± 0.0010
N(Good photons) = 4	75195/84665	0.8883 ± 0.0011
$\theta_{\gamma\gamma} > 15°$	72880/75195	0.9692 ± 0.0006
$E_{tot} > 800$ **MeV	72880/72880	1
Total momentum < 200 $^{**}MeV$	72879/72880	1
$E_{min} > 50$MeV	67676/72979	0.9273 ± 0.0010
$\|cos\theta\| < 0.91$	61327/67676	0.9062 ± 0.0011
$\chi^2_{min} < 25$	59048/61327	0.9628 ± 0.0008
90 MeV/$c^2 < m_{\gamma\gamma} <$ 180 MeV/C^2	29968/59048	0.508 ± 0.002
350 MeV $< E_{max} <$ 390 MeV	24360/29968	0.813 ± 0.002
Overall	24360/120000	0.2030 ± 0.0012

* evaluated respect to the previous cut, ** these cuts are in EVCL yet

5.9 DATA-MC comparison and systematic errors evaluation

In this section we evaluate various systematic effects, especially those which may arise from differences in the data/MC distributions used in the analysis.

5.9.1 Systematics due to the $\chi^2 cut$

We evaluate the systematics due to possible differences in the χ^2 distribution between data and MC by comparing a data control sample with MC. The chosen control sample is the channel $e^+e^- \rightarrow \omega(\rightarrow \pi^0\gamma)\gamma \rightarrow 4\gamma$ that is the only channel with four photons that we have in our selection. Because the kinematic fit requires only the energy-momentum conservation, we can compare its χ^2 distribution directly to that of the channel $\eta \rightarrow 3\gamma$ from MC. The selection of the control sample is done in the following way.

- We do a kinematic fit under quadrimomentum conservation hypothesis. We build the $m_{\gamma\gamma}$ variable for any pair of photons and select as m_{π^0} the closest value to the π^0 mass;

- we do a kinematic fit under π^0 and quadrimomentum conservation hypothesis and select the combination that minimize the χ^2, then we build the variable $m_{\pi^0\gamma}$, using as γ the most energetic of the remaining two γ not associated to the π^0.

The plot of the two dimensional distribution $(m_{\pi^0\gamma}, m_{\pi^0})$ is reported in fig. (5.12). There can be seen a peak due to the $\omega\gamma$ process. We plot the projection along m_{π^0} in fig. (5.13) and select the range $128 < m_{\pi^0} < 145\ MeV/c^2$. For these events we plot $m_{\pi^0\gamma}$, shown in the same figure, and select the range $760 < m_{\pi^0\gamma} < 815 MeV/c^2$.

The events that pass this selection are the $\omega\gamma$ candidates. In fig. (5.14) we have reported the χ^2 distribution of the kinematic fit, under energy-momentum conservation hypothesis, for the selected $\omega\gamma$ sample and for MC $\eta \rightarrow 3\gamma$ sample. The upper plot is the χ^2 distribution, the lower plot is the fraction of events that survives to a given χ^2 cut, normalized to the range shown in figure. For $\chi^2_{cut} = 25$ the DATA-MC discrepancy is about 3% (in fact being the kinematic fit done only requiring total energy-momentum conservation the two χ^2 distributions should be the same. This is the systematic error that we assume for this cut.

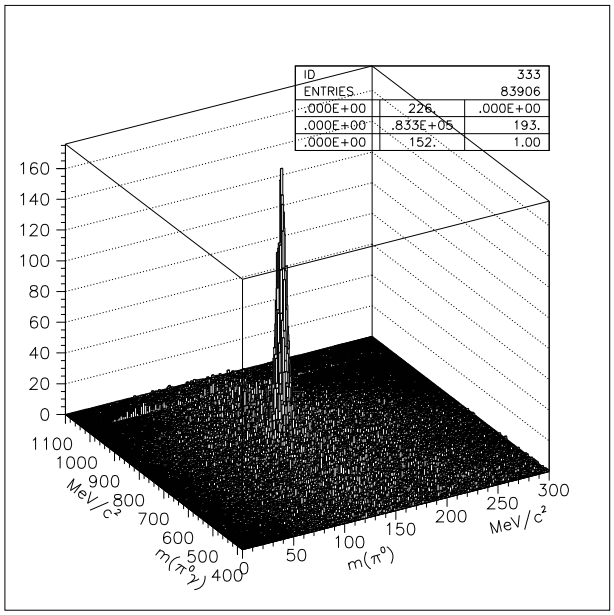

Figure 5.12: Two dimensional distribution of $m_{\pi^0\gamma}$ versus $m_{\gamma\gamma}$.

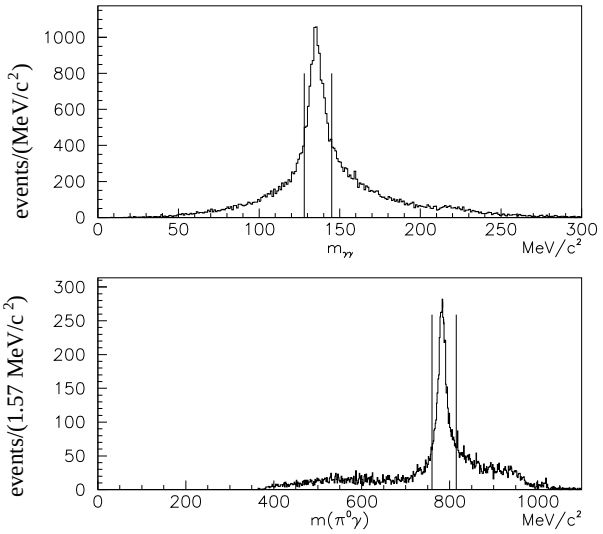

Figure 5.13: **up** distribution of $m_{\gamma\gamma}$ closest to the true value of π^0 mass; **down** distribution of $m_{\pi^0\gamma}$ after the selection on $m_{\gamma\gamma}$ (see text). In both figures the lines indicate the selected range.

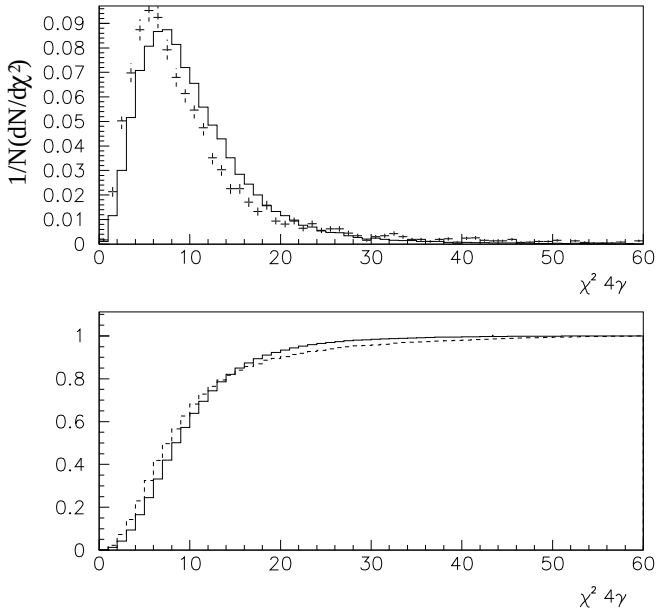

Figure 5.14: (Up) χ^2 distribution for MC $\eta \to 3\gamma$, continuous line, and $\omega\gamma$ selected sample (see text), dashed line.

5.9.2 Systematic due to photon detection efficiency

The MC doesn't simulate with full accuracy the photon detection efficiency. Using a sample of $\phi \to \pi^+\pi^-\pi^0$ the efficiency has been evaluated directly from DATA as a function of the energy and $cos(\theta)$ of the photon, the ratio $w = \epsilon_{data}/\epsilon_{MC}$ has been evaluated. For this reason, we have evaluated the quantity:

$$Weight = \prod_{i=1}^{4} w_i \quad \text{“i” runs on the four photons.}$$

for each event. The sum of the weights gives the effect of this discrepancy on the efficiency. The results are:

unweighted events	24360/120000 (20.3 %)
weighted events	24012/120000 (20.0 %)
$\Delta\epsilon/\epsilon$	1.5 %

The same effect is seen in the $\eta \to 3\pi^0$ that we will use to evaluate the upper limit. The effect on the ratio of the efficiencies $\epsilon(\eta \to 3\pi^0)/\epsilon(\eta \to 3\gamma)$ is below 1 %.

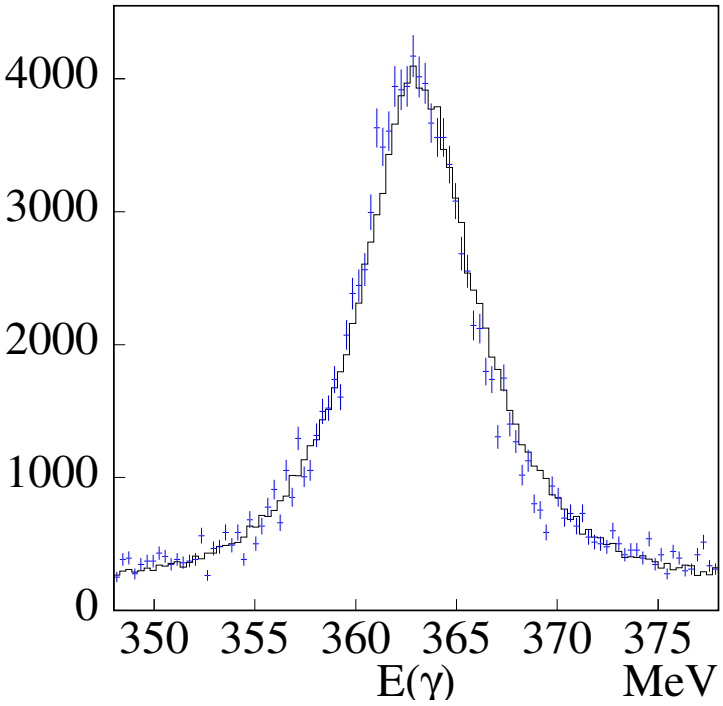

Figure 5.15: Energy distribution of photons in the $\phi \to \eta(\to \gamma\gamma)\gamma$ sample. Each event enters three times in the histogram, one for each photon. Both MC (continuous line) and DATA (points) are shown. To the energy value has been subtracted 361.68 MeV for MC and 362.707 MeV for DATA to take in account the wrong η mass value that is in the MC generator.

5.9.3 Systematics due to the shapes of signal and background

To test if the kinematic fit introduces a bias in the photon energy that is different for DATA and MC, we have analyzed a sample of 3γ events ($\phi \to \eta(\to \gamma\gamma)\gamma$) and compute the energy of each photon. This energy is plotted in fig. (5.15) both for DATA and MC. After having taken into account the wrong η mass that we have in MC generator ($m_\eta = 548.8$ MeV instead of 547.3 MeV) the two distributions overlap very well, so we don't quote the systematics on this variable.

5.9.4 Other systematics.

The stability of the upper limit versus the background estimate has been checked by comparing the results of polynomials of different degree for fitting the $E(\gamma_{hi})$ distribution outside the signal region. A 3^{rd} order polynomial doesn't describe the background shape well. A 4^{th} order polynomial gives a lower value for the signal yield, while a 6^{th} order polynomial gives the same result. We have also checked the stability of the result by changing the window chosen for evaluation of the upper limit obtaining a maximum variation of 11%.
Also the systematics coming from the assumption of a flat phase space dynamic of the three bodies decays has been checked by using the matrix element determined by Dicus for the $\pi^0 \to 3\gamma$ case [45] and we find a value 5% lower.

All the systematic contributions are summarized in tab. (5.3)

Contributions to the systematic error	
χ^2_{cut}	3 %
$\epsilon(\eta \to 3\pi^0)/\epsilon(\eta \to 3\gamma)$	1 %
Polynomial degree and window variation	11 %
Theoretical model	5 %

Table 5.3: Summary of the contributions to the systematic error

5.10 Final result

We have evaluated the number of η in the data sample through the study of the decay channel $\eta \to 3\pi^0$ as in the $\eta \to \pi^0\gamma\gamma$ case (see sec. 4.4).
Then we evaluate the ratios of the two branching ratios:

$$\frac{Br(\eta \to 3\gamma)}{Br(\eta \to 3\pi^0)} \leq \frac{N_{Up}\ \epsilon_{\eta\to 3\pi^0}}{N_{\eta\to 3\pi^0}\ \epsilon_{\eta\to 3\gamma}}$$

being $\epsilon(\eta \to 3\gamma) = 20.0 \pm 0.01(stat.) \pm 0.02(syst.) \pm 0.006(\chi^2_{cut})$, we obtain:

$$\frac{Br(\eta \to 3\gamma)}{Br(\eta \to 3\pi^0)} \leq 6.3 \cdot 10^{-5} \quad 95\ \%\ \text{C.L.}$$

$$\frac{Br(\eta \to 3\gamma)}{Br(\eta \to 3\pi^0)} \leq 4.9 \cdot 10^{-5} \quad 90\ \%\ \text{C.L.}$$

Using the PDG2002 value for $Br(\eta \to 3\pi^0) = (32.51 \pm 0.29)\%$ we have:

$$Br(\eta \to 3\gamma) \leq 2.0 \cdot 10^{-5} \quad 95\ \%\ \text{C.L.}$$

$$Br(\eta \to 3\gamma) \leq 1.6 \cdot 10^{-5} \quad 90\ \%\ \text{C.L.}$$

Conclusions

In this work we have measured the $\eta \to \pi^0\gamma\gamma$ branching ratio with the KLOE experiment.
The decay has been searched in 5 γ's events due to its decay topology: $\phi \to \eta(\to \pi^0\gamma\gamma)\gamma$.
The background is of three types: 5γ's events originating by other decay processes, $> 5\gamma$'s events with the loss or the merging of some clusters, $< 5\gamma$'s events with the adjoint of accidental clusters.
The direct 5 γ sources are reduced through cuts on the intermediate particles mass.
The $> 5\gamma$'s events are due mainly to $\eta \to 3\pi^0$ decay. There are three different topologies which simulate signal: $\eta \to 3\pi^0$ with two lost clusters, with one lost cluster and two merged clusters, and the third with 2 pairs of merged clusters.
The topologies with lost photons are reduced with dedicated kinematic fit in the background hypothesis, the third has been reduced with a likelihood function built using cluster shape variables: position and time.
Background coming from $< 3\gamma$ events plus accidental has been completely rejected with a cut on the energy and angle of the photons.
Background coming from kaons decays has been completely rejected using the time information provided by the calorimeter.
MC has been used to simulate the signal and background. All the selection variables show a good agreement with the DATA. This agreement has been studied using some control samples.
The background composition has been determined by fitting the $m_{\gamma\gamma}$ distribution at an early stage of the analysis and the relative contributions of the background components have been fixed in the following.
The signal has been extracted by a maximum likelihood fit of the $m(\pi^0\gamma\gamma)$ distribution, that shows a significant peak at the η mass. The background spectrum has been obtained by MC.
Being the available MC sample just 5 times the DATA sample, the statistical fluctuations of the MC have been included in the fit.

The signal presence has been established at about 99 % C.L.
The selection efficiency is $\sim 4.6\%$. To extract the $\eta \to \pi^0\gamma\gamma$ branching ratio the number of $\eta \to 3\pi^0$ decays in the same DATA sample has been determined with a dedicated analysis requiring 7γ's.
Using the $\eta \to 3\pi^0$ branching ratio we find $Br(\eta \to \pi^0\gamma\gamma) = (7.7\pm2.7)\times10^{-5}$. This value is in agreement with Chiral Perturbation Theory prediction at $O(p^6)$ with vector resonance saturation assumption and some NJL model evaluation of $\mathscr{L}_6$ Lagrangian.
The value is in clear disagreement with the GAMS measurement and is compatible with the recent Crystal Ball measurement.

In doing this work also another channel has been studied: $\eta \to 3\gamma$. This a C violating decay whose branching ratio is predicted at $< 10^{-12}$ in the Standard Model. The work has been recently published by the KLOE collaboration [49] and the value obtained is $Br(\eta \to 3\gamma) < 1.6 \times 10^{-5}$ @90% C.L. This is the world best limit for this decay and is a factor ~ 40 lower than the previously published upper limit.

Bibliography

[1] S. Eidelman et al. (Particle Data Group), Phys. Lett. B592 (2004) 1

[2] M. E. Peskin and D. V. Schroeder, An Introduction to Quantum Field Theory, Addison-Wesley Publishing Company

[3] C. Vafa and E. Witten, Nucl. Phys. B234 (1984) 173

[4] J. Goldstone, Nuovo Cim. 19 (1961) 154

[5] S. Weinberg, Phys. Rev. Lett. 17 (1966) 616

[6] L. Ametller, J. Bijnens, A. Bramon, F. Cornet, Phys. Lett. B276 (1992) 185

[7] E. Oset, J. R. Pelaź and L. Roca, Phys. Rev. D67 (2003) 073013

[8] K. Hagiwara et al. (Particle Data Group), Phys. Rev. D66 (2002) 010001

[9] S. Bellucci and C. Bruno, Nucl. Phys. B452 (1995) 626

[10] J. F. Donoghue, E. Golowich and B. R. Holstein, Dynamics of the Standard Model, Cambridge (1992)

[11] S. Bellucci, J. Gasser and M. E. Sainio, Nucl. Phys. B423 (1994) 80

[12] G. Ecker, J. Gasser, A. Pich and E. de Rafael, Nucl. Phys. B321 (1989) 311

[13] J. N. Ng and D. J. Peters, Phys. Rev. D46 (1992) 5034

[14] J. N. Ng and D. J. Peters, Phys. Rev. D47 (1993) 4939

[15] J.Bijnens, A. Fayyazuddin and J. Prades, Phys. Lett. B379 (1996) 209

[16] Y. Nemoto, M. Oka and M. Takizawa, Phys. Rev. D54 (1996) 6777

[17] A. A. Belkov, A. V. Lanyov, S. Scherer, J. Phys. G 22 (1996) 1383

[18] The KLOE Collaboration, A. Aloisio et al, Phys. Lett. B541 (2002) 45

[19] G. Di Giugno et al., Phys. Rev. Lett. 16 (1966) 767.

[20] M.N. Achasov et al., Nucl. Phys. B600 (2001) 3

[21] A.A. Wahling, E. Shibata, I. Mannelli, Phys. Rev. Lett. 17 (1966) 221

[22] M. Feldman et al., Phys. Rev. Lett. 18 (1967) 868.

[23] C. Baltay et al., Phys. Rev. Lett. 19 (1967) 1495

[24] S. Buniatov et al., Phys. Lett. 25 B(1967) 560.

[25] F. Jacquet et al, Phys. Lett. 25 B (1967) 574

[26] F. Jacquet, U. Nguyen-Khac, A. Haatfut, A. Halsteinslid, Nuovo Cimento 63 A (1969) 743.

[27] B. Cox, L. Fortney, J. Colson, Phys. Rev. Lett. 24 (1970) 534

[28] M. T. Buttran, M. N. Kreisler, R. E. Mischke, Phys. Rev. Lett. 25 (1970) 1358

[29] S. Devons et al., Phys. Rev. D 1 (1970) 1936

[30] S. Schmitt et al., Phys. Lett. 32 B (1970) 638

[31] Z. S. Strugalski et al., Nucl. Phys. B 27 (1971) 429

[32] A. T. Abrosimov et al., Yad. Fiz. 31 (1980) 371; A. T. Abrosimov et al., Sov. J. Nucl. Phys. 31 (1980) 195.

[33] Alde et al., Z. Phys. C25 (1984) 225

[34] N. Knetch et al., Phys. Lett. B589 (2004) 14

[35] A. Aloisio et al., Nucl. Instrum. Meth. A 516 (2004) 288.

[36] R. Brun, et al., GEANT3, CERN-DD/EE/84-1 (1984).

[37] R. Brun, et al., GEANT: Simulation for particle physics experiments, user guide and reference manual, CERN-DD-78-2-REV (1978).

[38] F. A. Berende, R. Kleiss, Nucl. Phys. B 228 (1983) 537.

[39] C. M. Carloni Calame, et al., The BABAYAGA event generator, hep-ph/0312014 (2003)

[40] N. N. Achasov, V. V. Gubin, Phys. Rev. D 63 (2001) 094007.

[41] A. Aloisio et al., Phys. Lett. B537 (2002) 21

[42] A. Aloisio et al., Phys. Lett. B536 (2002) 209

[43] A. G. Froedesen, O. Skjeggestad, H. Tøfte, Probability and Statistics in Particle Physiscs - Universitetsforlaget (Bergen, Oslo, Tromsø)

[44] CERN Program Library Long Writeup Y250 (http://wwwasdoc.web.cern.ch/wwwasdoc/hbook_html3/hboomain.html)

[45] D.A. Dicus, Phys. Rev. D12 (1975) 2133

[46] P. Herczeg, *Proc. Int. Workshop on Production and Decay of Light Mesons*, P. Fleury ed., Paris, France, (World Scientific, 1988), 16.

[47] B.M.K. Nefkens and J.W. Price, Phys. Scripta, T99 (2002) 114

[48] G.J. Feldman, R.D. Cousins, Phys. Rev. D57 (1998) 3873; J. Neyman, Phil. Trans. A236 (1937) 333

[49] A. Aloisio et al., Phys. Lett. B591 (2004) 49